Applied Thermal Engineering 281 (2025) 128608

Contents lists available at ScienceDirect

Applied Thermal Engineering

journal homepage: www.elsevier.com/locate/apthermeng

Research Paper

A new TEG-supported thermal management system of the battery system for an electric vehicle

Ahmet Mavi [a,*], Oguz Arslan [b]

[a] Vocational School, Bilecik Şeyh Edebali University, Bilecik, Turkey
[b] Departman of Mechanical Engineering, Faculty of Engineering, Bilecik Şeyh Edebali University, Bilecik, Turkey

ARTICLE INFO

Keywords:
Electric vehicle
Heat pump
Li-ion battery
Thermoelectric generators
Waste heat recovery

ABSTRACT

A multifunctional energy recovery system using phase change materials (PCM) and thermoelectric generators (TEG) was designed to utilize battery-derived waste heat in electric vehicles. System performance was evaluated using four different cycle fluids: R134a, R152a, R1234yf, and R1234ze, at discharge rates from 0.2C to 5C. In winter conditions, both TEG-I and TEG-II provided electricity generation, while in summer mode, only TEG-II was active. At 5C-rate, the total electricity generation from TEG-I and TEG-II was calculated to be 199 W. The highest COP of 3.47 was achieved for R1234ze, while the maximum second-law efficiency of 57.14 % was achieved with R1234ze. The New Concept (NC) system was observed to offer a 9.80 % advantage in second-law efficiency and an 7.39 % advantage in COP compared to the Conventional System (CS). Furthermore, in economic evaluations, the highest Net Present Value (NPV) of $1265.25 was calculated for R1234ze fluid at 2000 kPa. These findings suggest that the proposed integrated system may offer notable improvements in energy efficiency and economic sustainability in electric vehicles. The payback period (PBP) 1C–5C discharge rates ranges from 3.26 to 5.64 years.

1. Introduction

In recent years, challenges such as global climate change, energy security, and the environmental impacts of fossil fuels have driven the transportation sector toward alternative fuels and electric vehicle technologies. In this context, electric vehicles (EVs) are becoming increasingly important for zero-emission policies and sustainable energy use. Furthermore, increasing energy efficiency, decreasing operating costs, and advances in battery technologies make the economic and technological advantages of electric vehicles even more attractive [1–3]. Compared to internal combustion engines, electric vehicles offer lower carbon emissions, higher energy efficiency, and lower operating costs [4,5]. However, one of the most critical elements in EV energy management is the thermal control of battery systems. One of the most important factors affecting battery life, safety and performance depends on the operating temperature [6–8]. The ideal operating temperature of lithium-ion batteries used in EVs is generally limited to between 25 °C and 40 °C [9,10]. Temperatures outside this range can lead to capacity loss, cell imbalance, and the risk of fire. Therefore, effective heating and cooling systems are required to maintain batteries within a certain temperature range [11,12]. At the same time, the energy consumption of these systems directly affects the driving range and system efficiency. In this context, a steady-state equivalent resistance electro-thermal analog model for prismatic cells was developed and it was shown that such simplified steady-state approaches can effectively predict the thermal behavior of lithium-ion batteries under different cooling conditions, thus providing a reliable basis for energy consumption evaluations [13,14]. Steady-state analyses and transient electrothermal modeling were performed together. Developed a time-dependent electrothermal model for a prismatic Li-ion cell and solved it using a finite difference approach in MATLAB. The model was validated with experimental data from the literature under air-cooled conditions. The study investigated the cell temperature variation with time under scenarios of 1C–5C discharge rate, 1–5 m/s air speed, and 15–35 °C inlet temperature. The maximum temperature values and temperature distribution under load steps and short driving profiles were compared. The transient solution provides more precision results in some parameters than steady-state analyses by revealing the maximum temperature increases and short-term fluctuations caused by thermal inertia and load steps throughout the drive cycle. However, the model remains at the single cell/sub-module level. Only air cooling is considered. Humidity/condensation effects and temperature-dependent changes in material properties are not taken into account. They also noted that battery pack-level

* Corresponding author.
E-mail address: ahmet.mavi@bilecik.edu.tr (A. Mavi).

https://doi.org/10.1016/j.applthermaleng.2025.128608
Received 5 August 2025; Received in revised form 15 September 2025; Accepted 30 September 2025
Available online 9 October 2025

Nomenclature

A	Area (m^2)
C	Discharge rate, Cell capacity (Ah)
C_p	Specific heat capacity (kJ/kg K)
C_{mr}	Maintenance cost ($)
D_h	Hydraulic diameter (m)
d	Diameter (m)
E	Open circuit voltage (V)
F	Forced convection-boiling factor
G	Mass velocity (kg/m^2s)
h	Heat transfer coefficient (kW/mK)
I	Discharge current (A)
j	Culborn factor, Current density (A)
k	thermal conductivity (W/mK) / Isentropic exponent
$\dot{m}$	Mass flow rates (kg/s)
n	Depreciation period
N	Total number of cycles
N_t	Total number of pipes
Nu	Nusselt number
P	Pressure (kPa)
Pr	Prandtl number
Q	Heating capacity (kW)
q_J	Joule heat (J)
q	Heat production rate (W)
R	Resistance (Ω)
Re	Reynolds number
S	Effectiveness factor
s	Entropy (kJ/kg K)
T	Temperature (K)
T_B	Battery temperature (K)
U	Overall heat transfer coefficient (kW/mK)
W_C	Compressor power (kW)
x	Dryness fraction

Subscripts

f	Saturated liquid
g	Saturated vapor
i	Inlet
o	Outlet
k	Bubble boiling
z	Forced convection coefficients

Greek symbols

ε	Exergy efficiencies (%)
δ	Wing thickness (m)
μ	Viscosity (kg/ms)
η	Energy efficiency (%)
σ	Surface tension (N/m)
ρ	Density (kg/m^3)

Abbreviations

ATEG	Automotive Thermoelectric Generator
PBP	Payback period
COP	Coefficient of performance
Con	Condenser
Comp	Compressor
CS	Conventional system
EV	Electric vehicle
EG	Electric generation
Evap	Evaporator
ExV	Expansion valve
GWP	Global warming potential
HVAC	Heating, ventilation, and Air conditioning
HPAC	Heat pump air conditioner
ICC	Initial capital cost (USD)
ITMS	Integrated thermal management system
LHTS	Latent Heat Thermal Energy Storage
MSDM	Multi-Scale Multi-Domain Model
NTGK	Newman, Tiedemann, Gu, and Kim
NPV	Net present value
NC	New concept
ODP	Ozone depletion potential
PCM	Phase change material
SEI	Solid Electrolyte Interphase
SOC	State of charge
TEG	Thermoelectric generator
TMS	Thermal management system

integration and related control strategies was excluded from the scope [15]. Another study examined the thermal management system under both steady-state and transient conditions. Four different connection configurations were evaluated in the study. The steady-state analysis revealed the effects of ambient temperature, battery heat generation rate, and mass flow rate on COP, cooling capacity, and battery surface temperature. The findings indicated that the series configuration provided the highest steady-state performance, while the parallel configuration provided the lowest. Furthermore, the transient analysis examined the system's time-dependent response to driving cycles. In particular, it has been reported that series and series–parallel configurations maintain more uniform battery temperature distribution during load changes [16]. Thermal management systems of EVs are of critical importance not only for the battery but also for cabin climate control [17,18]. In this context, utilizing the waste heat generated in electric vehicles carries great potential to increase energy efficiency. The waste heat generated from the battery, inverter, motor, and cooling systems can be used for both cabin heating and energy recovery [19,20]. In this regard, heat recovery applications not only increase system efficiency but also contribute to maintaining thermal stability by preventing battery overheating.

Among the systems developed for utilizing waste heat, PCM and TEG stand out [21–23]. In this context, the dual validation approach for TEG-based waste heat recovery stands out as a method that ensures the compatibility of design conditions with real-world driving conditions. ANSYS-based numerical modeling and on-board prototype testing. The method aims to more reliably determine the performance band under real-world driving conditions by calibrating steady-state predictions with transient measurements. Indicate that design parameters such as temperature difference, Seebeck coefficient, leg length, string connection, and geometry are first computationally screened and then validated with static and dynamic on-board experiments. However, it is noted that dynamic flow and temperature fluctuations can lead to limited deviations in power output compared to laboratory or static predictions, and uncertainties remain regarding long-term durability, contact resistance/aging, and generalizability to different driving scenarios [24]. TEG integration into electric vehicle battery systems can simultaneously improve BTMS performance by converting waste heat into electricity, while the integrated use of PCM and TEG minimizes source temperature fluctuations through phase-change-based thermal energy storage. It also supports the creation of a sustainable temperature difference (ΔT) across the TEG, offering the potential to increase efficiency and operating time under both steady and transient operating conditions [25,26].

PCM equipped heat exchangers are particularly effective in balancing both cooling and heating loads during seasonal transitions.

They increase temperature uniformity by keeping the maximum temperature in battery packs approximately 12 °C lower than in air cooled systems. and by reducing the temperature difference to less than 1 °C, it extends cell life and increases energy density [27,28]. Bhakta and Kundu [29] stated that the main problem encountered in TEG applications for waste heat recovery in the automotive industry is that conversion efficiencies generally remain at the level of 3–5 %. This limitation arises from factors such as material properties, thermal matching, and integration challenges. Liu et al. [30] emphasized that TEG-PCM hybrid systems can simultaneously perform both heat storage and electricity generation, and that the PCM's high latent heat capacity allows for increased performance by maintaining a more stable TEG temperature difference. However, the same study also noted that limitations such as low thermal conductivity, phase separation, and thermal instability during long cycles limit the applicability of hybrid integration. PCMs, thanks to their high latent heat storage capacity, can limit temperature fluctuations in battery systems, while TEG systems directly generate electrical energy using the temperature difference [31]. Liu et al. [31] reported that PCM–TEG systems can increase energy conversion efficiency by 1 %-16 % compared to TEG alone. Furthermore, it is stated that appropriate geometric alignments can improve second-law efficiency by reducing entropy production [32,33]. They reported that the maximum efficiency level was approximately 4 % under the applied thermal load. In an experimental study conducted by Imran et al. [34], a configuration in which four TEG modules were integrated into the engine exhaust system produced a maximum voltage of 24.2 V, a current of 3.22A, and an electrical power of 78.05 W. In this system, the water-cooled heat exchanger effectively maintained the temperature difference and optimized energy conversion. Similarly, Shi et al. [35] experimentally investigated a PCM-assisted TEG system and reported a total electrical output of 3211.6 J with a thermal energy input of 225 kJ. The average energy conversion efficiency calculated during this process was determined to be 1.472 %. It was also emphasized that heat source power is the most decisive parameter for system performance. These studies demonstrate that PCM-TEG systems provide a more stable temperature profile by balancing the effects of transient heat sources and offer an efficient option for meeting the energy needs of auxiliary systems in electric vehicles. The integrated use of these two technologies enables both thermal management and energy recovery, thus increasing overall system efficiency. PCM-TEG hybrid systems, in particular, can meet the energy needs of auxiliary systems by converting waste heat from the battery or condenser into electricity. Shi et al. [36] showed that a TEG system integrated with a PCM improved system stability against transient temperature changes, and improved open-circuit voltage by 0.7 % and power output by 1.16 %. PCM-TEG hybrid systems, in particular, can meet the energy needs of auxiliary systems by converting waste heat from the battery or condenser into electricity. Mao et al. [37] experimentally demonstrated that a TEG system integrated with a PCM increased the total energy production by approximately 25 %. Al Janabi et al. [38] investigated the potential of TEG modules to generate electricity through the effect of temperature differences. In the tests, an output voltage of 4.13 V was obtained, and operating temperatures reached up to 116 °C. Furthermore, system efficiency varied between 3.6 % and 15.9 % depending on the temperature difference. These results demonstrate that TEG systems can be used effectively to generate electricity from waste heat. In this context, PCM and TEG systems offer significant advantages in battery-based waste heat recovery, while integrated heat pump-supported structures represent a strong alternative in terms of energy and exergy performance.

These systems, developed for both cabin heating and battery cooling in electric vehicles, increase energy efficiency and system flexibility when applied together with waste heat recovery [39]. The shift towards low-GWP refrigerants (R1234yf, R744/CO_2, R290) in EV heat pumps has accelerated; life cycle climate performance (LCCP) analyses show that these options can reduce emissions from both direct leakage and indirect energy consumption compared to R134a [40]. Considering regional climate conditions, R744-VI configurations have been found to be more suitable in cold regions and R1234yf-based cycles in warm-temperate regions [41]. In the study of Tang et al., a heat pump system with R134a refrigerant without PCM integration was tested in a −5 °C environment; approximately COP 3.2 and 3.6 kW heating capacity were reported, and exergy destruction was given as 55 % for the compressor, 28 % for the expansion valve, 12 % for the condenser, and 5 % for the evaporator [42]. In the analyses conducted on PCM-integrated systems, the exergy efficiency was found to be approximately 31 % [43]. In addition, in a study by Rezaei et al., the driving range of an electric vehicle with a PCM-based HVAC system was increased by 11 % in cooling mode and 19 % in heating mode [44]. From an economic perspective, optimizing the design of an efficient BTMS significantly reduces life cycle costs. Lander et al. reported a 27 % reduction in LCC (from $0.22/km to $0.16/km) by switching to surface cooling [45], while Asef et al. studied the total BTMS cost for a hybrid electric vehicle under different driving cycles and reported that the best possible return was around $200 [46]. These data was showed that PCM-supported heat pump systems have a positive effect on both energy and exergy efficiency and increase the thermal stability of the system against seasonal conditions. In the evaluation of these systems, not only energy efficiency but also economic feasibility is of great importance. NPV analyses are used as a fundamental tool in determining the payback period of the investment cost and the economic viability of the system [47]. Li et al. [48] examined the energy, exergy, and economic performance of the TEG system they developed for the automotive sector. Analyses conducted under different structural designs showed that the system could amortize its investment within approximately 2–3 years and provide a positive NPV. In a study conducted by Tian et al. [49], the energy efficiency and economic performance of the waste heat recovery mechanism integrated into the thermal management system of electric vehicles were investigated. In addition, the system provides annual operating cost savings of €162-249 compared to the PTC heater, and thus the payback period is between 4.57 and 6.77 years. Ji et al. [50] reported that a new generation Automotive Thermoelectric Generator (ATEG) system with integrated heat pipes produced 613.2 kWh of electricity annually, resulting in an economic gain of $85.85. They reported that the cost recovery period was 2.86 years, while for conventional ATEG this period was 1.83 years and the production was 423.4 kWh.

This study examined a waste heat recovery system that integrates PCM and TEG and can operate according to seasonal conditions. In winter conditions, the battery temperature was kept constant at a maximum of 40 °C, and the waste heat generated from the water-cooled battery was utilized in the PCM-TEG I integrated heat exchanger, which contributes to cabin heating. A second PCM-TEG II block, located at the condenser outlet, generated electricity at two different points within the system. In summer conditions, the battery was cooled by ambient air and its temperature was controlled to not exceed 60 °C. This high-temperature waste heat was utilized through the PCM-TEG II block, which functions as an evaporator. System performance was analyzed in detail under different C-rate values and environmental conditions, using heat exchanger structures specifically designed for both modes. The proposed configuration was compared with the conventional system, and an NPV analysis was conducted in addition to energy and exergy performance. Discounted payback periods (DPB) was calculated according to different C-rates.

2. System description

In order to utilize the waste heat released from the battery in electric vehicles, a two-stage thermal management cycle with integrated phase change material (PCM) and thermoelectric generator (TEG) was designed. In heating mode, the battery is cooled with water, first transferring the heat to the PCM-TEG1 block, and then to the PCM-TEG2 block. This process generates electricity through both TEG1 and TEG2, while the hot surface of TEG2 effectively heats the vehicle cabin. In

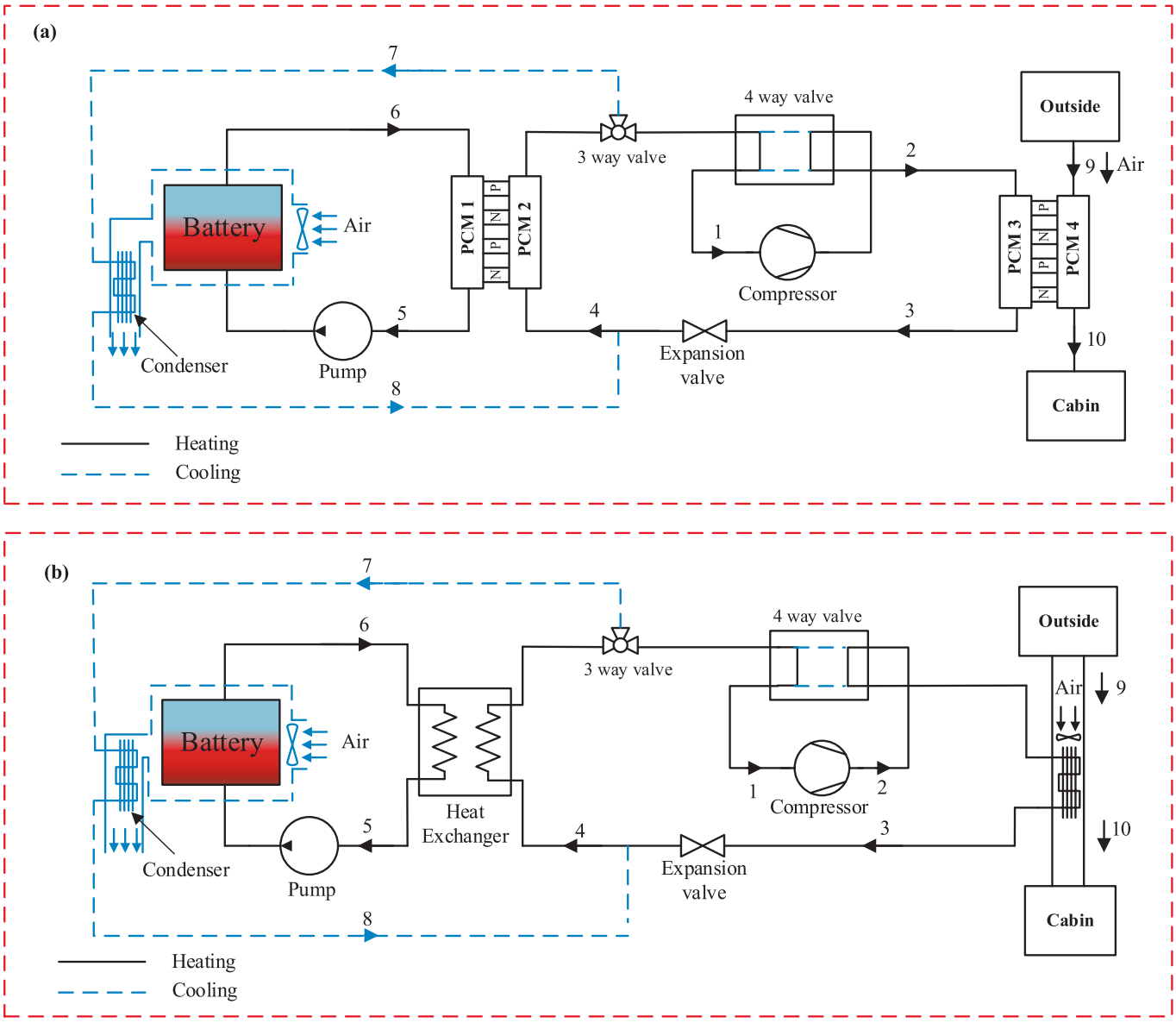

Fig. 1. (a) PCM and TEG integrated new generation heating–cooling system (NC) and (b) conventional system (CS).

cooling mode, the battery is cooled with air, occupied only by the PCM-TEG2 block. In this mode, the cabin is cooled by the cold surface of TEG2, while electricity is generated through TEG2. The flow diagram of the heating and cooling states of the system and the conventional system is given in Fig. 1.

This study presents a new two-stage system design integrated into the thermal management system of electric vehicles. The primary objective of the design is to perform in vehicle heating and cooling through heat energy recovery, while also generating additional electricity through the TEG.

In the initial design, operating conditions for the battery at different discharge rates (C-rates) were evaluated, taking winter conditions into account. The waste heat amounts corresponding to C-rates of 0.2C, 0.3C, 0.5C, 1C, 3C, and 5C were calculated based on thermal equilibrium. The battery temperature was maintained at a maximum of 40 °C, which is considered ideal for cell safety and performance [51]. The maximum temperature was limited to not exceed 40 °C. The battery was cooled with water, and the waste heat generated from this coolant was transferred to the first phase change material block, PCM1. PCM1′s temperature was maintained by the waste heat transferred from the battery coolant. The temperature of PCM2 was determined by the dual-phase refrigerant circulating in the vehicle's heating system. Electricity generation was achieved through TEG1 based on the fixed temperature difference created between these two PCM blocks. A similar structure was also built around a second TEG module, taking into account the fixed temperature difference created between PCM3 and PCM4 blocks. The temperature of PCM3 was determined by the temperature of the refrigerant circulating in the vehicle's cooling circuit. The temperature of PCM4 was fixed by considering the external ambient conditions and the vehicle cabin target temperature. Thus, a second temperature difference-based electricity generation process was implemented through TEG2. The use of PCM in both TEG units improves the system's thermal equilibrium conditions and allows the heat flow to be directed in accordance with the Second Law of Thermodynamics.

In the second design, the system was reconfigured for in-car cooling in summer conditions. This design, consistent with the first system, considered the same battery operating conditions. However, in this system, the battery was cooled directly by ambient air. For this purpose, a fan was placed in front of the battery. Fan-assisted airflow controlled the battery temperature to a maximum of 60 °C. In this design, the

PCM1, PCM2, and TEG1 elements used for heating were excluded from the system. Instead, a condenser was integrated into the system structure. The heat generated by this condenser was transferred to the in-car air conditioning system. Electricity generation was also provided by TEG2, placed between the PCM3 and PCM4 blocks. The temperature of PCM3 was determined by the temperature of the refrigerant circulating in the cooling cycle, while the temperature of PCM4 was determined by the temperature of the outside air and the in-car air conditioning conditions. This aims to maintain the temperatures of both PCM blocks consistently, enabling electricity generation based on the temperature difference via TEG2. In this arrangement, heat transfer occurs from the vehicle's cooling system to the battery side. Thus, heat flow from higher to lower temperatures is achieved for both heating and cooling the vehicle interior, as required by the Second Law of Thermodynamics.

In the HPAC cycle, the vapor-phase refrigerant first enters the compressor, where its pressure is increased to match the system's operating conditions (point 1). The elevated pressure and temperature refrigerant is then delivered to the condenser (point 2). The heat released during condensation in the condenser is transferred to PCM3, which melts and stores the heat. At the same time, the hot surface of TEG2 is connected to PCM3, which generates electricity from the temperature difference between PCM3 and the cold side. The cold surface of TEG2 is created by PCM4. Outdoor air (point 9) is delivered to PCM4 and sent into the cabin to meet the heating needs of the vehicle cabin (point 10). The refrigerant leaving the condenser is in liquid phase and is sent to the expansion valve (ExV) (point 3). The pressure and temperature of the isenthalpicly expanding refrigerant in ExV decreases. The resulting liquid–vapor mixture was directed to PCM2, which forms the cold side of the evaporator (point 4). In this region, the refrigerant evaporates, absorbing heat from the evaporator. PCM2 forms the cold side of TEG1 to generate electricity from TEG1. The BTMS refrigerant (point 6) leaving the battery transfers its waste heat to PCM1. PCM1 melts and stores the heat, and this surface forms the hot side of TEG1. The refrigerant that releases its heat (point 5) leaves PCM1 and returns to the battery as cooled water. When the 4-way valve is changed in cooling mode, the heat exchanger in the battery section operates as a condenser. The refrigerant condenses there, exits in gaseous form at point 7, and returns to the main circuit via line 8. In this mode, the PCM1-PCM2 blocks and the TEG1 line was disabled.

Because PCM operates in a closed volume, there is no mass exchange with the environment, and mass losses due to leakage was not considered. Leakage due to volume instability during melting is a significant problem for PCMs. However, encapsulation and/or form-stable composite design with a porous carrier framework effectively prevents leakage. Indeed, experimental leakage tests have demonstrated that no leakage is observed in expanded graphite (EG)-supported composites, even at a 75 % PCM fraction. Furthermore, it has been reported that form-stable PCMs with recyclable frameworks prevent leakage through capillary effects and surface tension, and that sealing/stability can be maintained even after $\geq$ 2000 thermal cycles. [52,53]. In this context, the stability of the PCM reported in the literature appears to have approximately the same life cycle as a vehicle battery. In this study, the electrical outputs of the TEG were taken directly from the manufacturer's specifications, based on the temperature difference between its two surfaces. Because these specifications include thermal and electrical losses within the module, the reported power values represent the final net output. Therefore, no additional thermal losses for the TEG were added to the model. Furthermore, since the study was considered a new system and was conducted theoretically, integration into existing EVs was not considered.

In the conventional model, Battery temperature control is achieved through the water cooling circuit in winter operating conditions, whereas it is achieved through the air cooling circuit in summer operating conditions. This system includes an intermediate heat exchanger in the Battery section. Therefore, energy recovery components such as the PCM and TEG are not integrated into this section. The flow diagram of the conventional system is presented in Fig. 1b. To ensure a reliable and equal simultaneous comparison with the new system (NC), the same operating conditions were defined for heating and cooling modes. In this context, the cabin heat load for both systems was kept constant, and differences in compressor power and performance due to waste heat utilization were evaluated based on the methodology. In the NC, Battery waste heat is utilized through the PCM and TEG modules without passing through the intermediate heat exchanger, resulting in electricity generation and additional profit. In the CS, however, because it includes an intermediate heat exchanger, there is no PCM-TEG section. Using this method, the CS and NC systems were compared with respect to different heat recovery strategies, and the results were evaluated in detail in terms of energy efficiency, exergy balance, and economic performance indicators.

2.1. Heat generation in the battery

To perform a proper thermal analysis of a battery module, it is crucial to accurately determine the amount of heat generated during operation. The Bernardi formula is widely used for this purpose in lithium-ion batteries [54]. The heat generated within the cell consists of three main components: Joule heat due to ohmic losses, reversible heat due to entropic changes, and heat generated by side chemical reactions such as electrolyte degradation and solid electrolyte interface (SEI) layer formation. Among these components, Joule heat is the most heat source, especially in cells operating under high currents. Entropic heat can be positive or negative depending on the direction of operation and temperature, while the heat from side reactions is negligible under normal operating conditions [55–57]. The total heat generation in the cell was defined by the following expression developed by Bernardi et al. [58]:

$$q = I^2R - IT\frac{\partial E}{\partial T} \tag{1}$$

In this equation, q represents the total amount of heat generated in the battery cell per unit time (W); I represents the current flowing through the cell (A), R represents the internal resistance of the battery (Ω), T represents the temperature of the battery (K), and $\frac{\partial E}{\partial T}$ represents the rate of change of open-circuit voltage with respect to temperature (V/K). The term I^2R in the equation represents the Joule (ohmic) heat generated as a result of the internal resistance of the battery cell. This component is the irreversible energy loss due to resistance during the passage of electric current through the cell. This term generally contributes to the total heat generation. The second term in the equation, $IT\frac{\partial E}{\partial T}$, represents the entropy change occurring during electrochemical reactions in the battery cell and the temperature-dependent effect of this change. This expression demonstrates that reversible heat generation in the cell was related to the changes in current, temperature, and open-circuit voltage with respect to temperature.

2.2. Battery operating conditions

In this study, the thermal operating conditions of the electric vehicle battery vary depending on the vehicle's heating and cooling requirements in summer and winter. In winter, the battery is cooled with water, and its temperature is controlled to not exceed 40 °C. In this mode, the heat generated due to different discharge rates is directed to the TEG unit for interior heating. In summer, the battery is cooled by ambient air, and its temperature is limited to not exceeding 60 °C.

In the calculations performed in this context, the battery temperature is limited to not exceeding 40 °C, and waste heat values are obtained at C-rates between 0.2C and 5C. This range covers a wide range of real-world usage scenarios, from low-load city driving to highway operation and fast acceleration, and is consistent with typical electric vehicle driving profiles reported in the literature [59]. In this study, a steady-state approach is adopted to evaluate the fundamental thermal

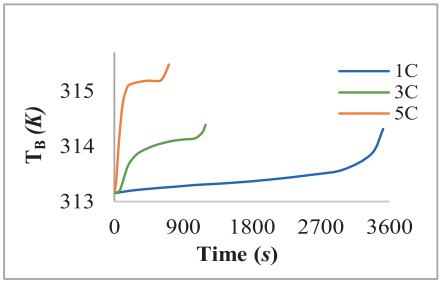

Fig. 2. Battery surface temperature profile under cooling conditions.

Table 1
Battery specifications [51].

Property	Value
Battery Chemistry	$LiMn_2O_4$
Cell nominal voltage	4.2 V
Cut-off voltage (cell)	3.0 V
Cell capacity	14.6 Ah
Total number of modules	360
Connection type	Series-Parallel Combination
System capacity	292 Ah
System voltage	453 V
Total power	132.4 kWh

behavior of the proposed thermal management system. This approach is supported by literature findings that show that once the battery surface temperature reaches a certain threshold, the heat generation rate remains relatively constant throughout the discharge process, especially under controlled thermal conditions and constant discharge rates [60]. In this context, when the battery operates at a constant discharge rate, heat generation increases more rapidly during the initial phase of discharge; however, once the battery reaches the target temperature of 40 °C, the heat generation rate approaches a largely stable level. At the same time, the discharge rate was chosen to represent dynamic driving conditions within the range of 0.2C–5C. This range varies between approximately (0.2–0.5C) for idle/cruise, approximately (1-2C) for urban acceleration, approximately (2-3C) for highway crossings, and approximately (3-5C) for sudden accelerations. Therefore, each C value was solved as a separate operating point, and the thermal loads for the acceleration-cruise-deceleration sections were represented using equivalent power levels. The 5C upper limit includes short-term sudden peaks on the safe side, while the 0.2C lower limit captures the need for thermal management at low load. Thus, the results can be generalized to dynamic conditions without being tied to a specific driving cycle. As illustrated in Fig. 2, the battery surface temperature stabilizes around 40 °C in a short time under various C rates, indicating that it can balance the dynamic heat generation. Therefore, the modeling approach based on steady-state behavior was considered as a suitable option to compare the effectiveness of the thermal management system (TMS) under different discharge scenarios.

The simulations were performed using ANSYS Fluent 2020R1, and the modeling process utilized the MSDM (Multi-Scale Multi-Domain Model) approach. The NTGK (Newman, Tiedemann, Gu, and Kim) battery module was employed to model the electrochemical and thermal behaviors of the battery cells. The selected battery cells are based on the $LiMn_2O_4$ chemistry, with a total power output of 132.4 kW. Initially, six lithium-ion cells with a rated capacity of 4.2 V and 14.6 Ah were connected in series, resulting in a module with 25.2 V voltage and an energy capacity of 367.92 Wh. Subsequently, 20 of these series-connected modules were connected in parallel, providing a total capacity of 292 Ah and an energy output of 7384 Wh. In the final stage, 18 of these parallel-connected units were arranged in series, forming a battery pack with a total voltage of 453.6 V and an approximate energy capacity of

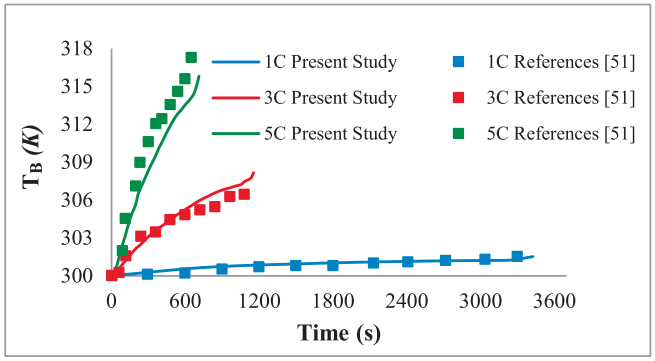

Fig. 3. Validation of simulation results [51].

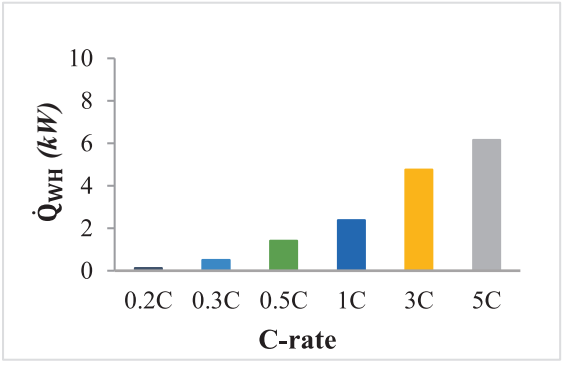

Fig. 4. Amounts of waste heat obtained from the battery at different discharge rates.

132.4 kWh. The properties of the battery system are given in Table 1.

This study is based on the results of numerical simulations conducted with ANSYS Fluent to evaluate the thermal performance of the proposed heat pump system. To support the accuracy of the battery model, the same operating conditions reported in the referenced study were adopted, and simulations were performed at 1C, 3C, and 5C discharge rates using the battery properties given in Table 1. The analysis confirms that the proposed system operates consistently under identical thermal conditions across different discharge rates. The results of the CFD analysis performed to evaluate the electric vehicle battery as a waste heat source were validated in the authors' previous work [51]. The battery system's validation results is given in Fig. 3.

The validation analyses determined the average percentage error (MAPE) values between 0.3580 % and 0.5538 %. The correlation coefficients (R^2) were calculated as 0.987, 0.971 and 0.963. In this regard, the simulation results are highly agreeable with the literature. The amount of thermal energy transferred to the TEG I at different discharge rates in the in-vehicle heating mode, with the battery cooled by water, is given in Fig. 4.

According to Fig. 4, when the battery temperature is 40 °C, the amount of waste heat generated from the battery varies depending on the discharge rate. The lowest waste heat was approximately 0.288 kW at a 0.2C discharge rate, while the highest was 6.192 kW at a 5C rate. In the system design where the electric vehicle battery is air-cooled, the battery temperature is limited to a maximum of 60 °C. Furthermore, different temperature ranges were determined for the battery temperatures used in the analyses, not exceeding 30 °C, 35 °C, 40 °C, 45 °C, and 50 °C. The battery was cooled using ambient air as the cooling medium. The air temperatures used were set at 25 °C, 30 °C, 35 °C, 40 °C, 45 °C, and 50 °C. Cooling was performed only under conditions where the ambient temperature was lower than the battery temperature. Therefore, for each air temperature, only temperature matches corresponding to higher battery temperatures were considered. This approach aimed to

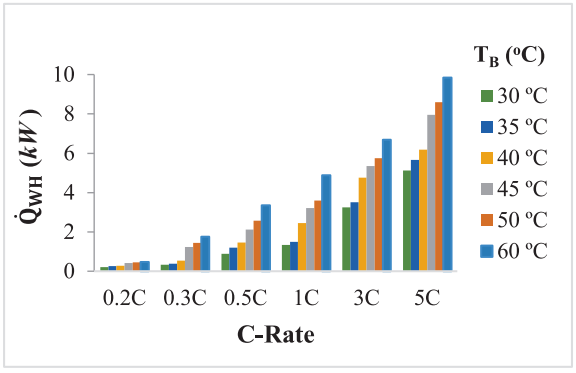

Fig. 5. Amounts of waste heat obtained at different battery temperatures.

effectively cool the battery and maintain it within the target temperature range. Accordingly, the amounts of waste heat generated during the battery cooling process is given in Fig. 5.

According to Fig. 5, increasing battery temperature leads to a significant increase in the amount of waste heat generated. In the analyses performed, the minimum and maximum waste heat values corresponding to each battery temperature were calculated. Accordingly, at a battery temperature of 25 °C, the waste heat amount ranged from 0.146 kW to 4.748 kW, while at 60 °C, these values ranged from 0.471 kW to 9.846 kW. Similarly, the waste heat ranges for temperatures of 30 °C, 35 °C, 40 °C, 45 °C, and 50 °C were determined as 0.216–5.126 kW, 0.269–5.662 kW, 0.288–6.192 kW, 0.4248–7.963 kW, and 0.45–8.596 kW, respectively. These results demonstrate that increasing battery temperature increases waste heat. As temperature increases, battery internal resistance and Joule heat losses also increase, especially under high C-rate conditions. This directly was impacted the cooling load transferred to the thermal management system. Therefore, controlling battery temperature is critical not only for cell safety but also for optimizing waste heat management.

2.3. Performance losses in Li-ion batteries

An increase in temperature leads to both a decrease in capacity and a decrease in energy efficiency due to the accelerated degradation processes in the electrochemical balance and interface structures of lithium-ion batteries. Especially at temperatures above 40 °C, mechanisms such as electrolyte degradation and SEI layer thickening accelerate. This reduces the amount of energy the battery can store and reduces overall system energy efficiency. Therefore, temperature control stands out as a critical parameter for sustainable battery performance [61]. The report that SEI layer growth is largely limited by diffusion and exhibits a gradually slowing rate with time (root-in-time scaling). Side reactions accelerate as temperature increases; SEI thickening becomes more pronounced, triggering capacity loss and increased internal resistance, reducing energy efficiency. The C-rate/current density and SoC level can increase the side reaction current by changing the anode potential. Therefore, degradation is accelerated at high C-rate and high temperature conditions. Because this study focuses steady-state performance, a detailed analysis of SEI kinetics is not included. Therefore, the importance of temperature control is paramount [62]. After 500 cycles at a constant temperature of 60 °C, the capacity retention rate of $LiMn_2O_4$ cells was determined to be 83.7 %. In this study, the operating energy was calculated as 91.98 kWh.

$$E_{Th} = V.C.N \tag{2}$$

This equation was used to calculate the total theoretical amount of energy (Wh) that the battery can produce over the number of cycles under ideal operating conditions (25)–(30) °C). Where, V represents the average cell voltage; C represents the capacity per cell (Ah); and N represents the number of cycles.

In the calculations, capacity and energy loss in $LiMn_2O_4$ cells were investigated using a nonlinear approach. Cyclic degradation and calendar aging were evaluated using empirical relationships that include temperature and time dependencies. The equation for cyclic aging is given below [63,64].

$$\Delta Q_{cyc}(N) = kN^{\beta} \tag{3}$$

$\Delta Q_{cyc}(N)$, Relative capacity/energy loss due to cycle at the end of N cycles, N number of cycles, k Calibration constant, β The nonlinear decay exponent is usually taken to be in the range $0.5 \leq \beta \leq 0.8$ for mechanisms such as diffusion limited/SEI growth. It was taken as 0.5 in the calculation. Calendar aging is as follows [63–65]:

$$\Delta Q_{cal}(t) = a\sqrt{t}\exp\left(-\frac{E_{a.cal}}{RT}\right) \tag{4}$$

ΔQ_{cal} (t) Relative capacity/energy loss due to calendar time at the end of time t, t time, a calibration coefficient (obtained from experimental data). $E_{a.cal}$ Activation energy for calendar aging (J/mol). R is the universal gas constant $(J/molK)$, T temperature (K). *Total losses are;*

$$\Delta Q(N,t) = \Delta Q_{cal}(t) + \Delta Q_{cyc}(N) \tag{5}$$

Capacity loss analyses were carried out by considering nonlinear degradation trends, and the capacity losses were calculated for 1500 cycles. The results are presented in Table 2.

The table compares the capacity, energy efficiency, cycle life, and performance of $LiMn_2O_4$ batteries at operating temperatures between 40 °C and 60 °C. The results reveal that electrochemical degradation within the battery results in a decrease in usable capacity and total energy output as the temperature increases. In particular, at 60 °C, capacity loss reached 28.2 %, and cycle count loss reached 245 cycles. This demonstrates that operating battery systems at high temperatures negatively impacts both energy efficiency and long term performance.

According to the values in the table, the highest COP of 2.47 was achieved at the optimum point when the battery temperature was 40 °C. As the battery temperature increased, performance decreased, with the COP dropping to 1.287 at 60 °C. It decreased to 1.319 at 45 °C, 1.310 at 50 °C, and 1.297 at 55 °C. This indicates that performance decreases with temperature, with the highest COP achieved at 40 °C.

2.4. Selection of refrigerants and comparison of their properties

Environmental impacts, heat transfer performance, and safety

Table 2
Capacity and energy losses due to temperature increase ($LiMn_2O_4$ battery, 4.2 V, 14.6Ah, 1500 cycles) [66,67].

Temperature (°C)	Capacity utilization rate depending on temperature (%)	Energy (kWh)	Energy loss(%)	1C discharge time (min)	Cycle	Cycle loss	COP
40 °C*	–	–	–	–	–	–	2.47
45 °C	88.76	81.63	19.47	48.3	1305	195	1.319
50 °C	87.07	80.08	22.39	46.6	1276	224	1.310
55 °C	85.39	78.54	25.31	44.8	1247	253	1.297
60 °C	83.07	76.40	28.23	43.1	1218	282	1.287

*Optimal point.

Table 3
Thermophysical properties of the selected fluids [68–71].

Property	Unit	Refrigerant			
		R134a	R1234yf	R1234ze	R152a
Type	–	Wet	Dry	Dry	Wet
ODP	–	0	0	0	0
GWP	–	1200	4	6	124
ρ*	kg/m^3	4.258	4.859	4.775	2.759
c_p*	kJ/kg·K	0.85124	1.183	0.887	1.051
k*	W/m·K	0.0133	0.0134	0.0135	0.0141
$T_{critical}$	°C	101	94.7	109	113.3
$P_{critical}$	kPa	4067	3382	3630	4496
Flammability	–	A1	A2L	A2L	A2
AIT	°C	770	405	368	454

*at 25 °C and 1 atm, AIT: Auto ignition temperature.

criteria are of paramount importance in the selection of refrigerants to be used in electric vehicle thermal management systems. In this study, four different refrigerants: R134a, R152a, R1234yf, and R1234ze, was evaluated due to their low environmental impact and distinct thermophysical characteristics. In particular, the "wet" and "dry" vapor characteristics of the refrigerants was considered due to their impact on the two-phase heat transfer mechanism. The refrigerant properties presented in Table 3 is provided for the purpose of comparing and describing their thermophysical parameters at standard reference conditions. In contrast, energy and exergy analyses were performed based on the actual operating temperatures and pressures at each point. State properties such as enthalpy, entropy, and density were obtained from the REFPROP (NIST) database. Thus, cycle performances were calculated by considering point-specific thermodynamic conditions. In this context, the basic thermophysical properties of the selected fluids is given comparatively in Table 3.

In the proposed new system, four different refrigerants R134a, R152a, R1234ze, and R1234yf was selected based on their thermodynamic performance, environmental impact, and operational safety. Refrigerant selection was based on three key criteria. high convective heat transfer coefficient, low environmental impact, particularly low ozone depletion potential (ODP) and low global warming potential (GWP), and efficient operation over a wide temperature range. Although R134a is being phased out due to its high GWP, it is still widely used in many countries, particularly in Turkey, and was considered the reference refrigerant in the proposed system. R152a, on the other hand, has a very low GWP, high latent heat capacity, and heat transfer capability. However, it requires caution due to its low flammability. Despite being classified as slightly flammable (A2L), R1234ze is a strong candidate for low-GWP applications thanks to its low environmental impact and stable thermophysical properties. R1234yf, on the other hand, was developed directly to replace R134a in mobile air conditioning systems. It is a refrigerant widely adopted in the automotive sector today, boasting both a low GWP and acceptable energy efficiency. Furthermore, the "wet" and "dry" vapor characteristics of the selected refrigerants were also taken into account, as they directly impact two-phase heat transfer mechanisms. This aimed to ensure stable and efficient evaporation and condensation processes. As a result, the selected refrigerants offer an environmental approach compatible with international climate targets while also providing the energy performance necessary for sustainable and effective thermal management in electric vehicles.

The battery is actively maintained at 40 °C or below, effectively preventing thermal runaway scenarios and keeping the temperature well below the autoignition points of the two-phase fluids. The refrigerant circuit is physically isolated from high-voltage battery components, and non-flammable insulation materials are applied within the battery compartment to minimize ignition risks from external sources. In the event of a collision or structural damage, automatic shut-off valves are activated to immediately seal the refrigerant loop. With these combined strategies-tight thermal regulation, physical isolation, leak detection, and emergency shut-off-the system ensures that two-phase fluids can be safely utilized in electric vehicle thermal management applications.

3. Modelling of thermoelectric generator (TEG)

The designed system utilizes TEGs to utilize waste heat from electric vehicle batteries and meet in-vehicle air conditioning (heating and cooling) loads. The TEG modules are integrated into a specially designed heat exchanger structure equipped with PCMs.The system is structured

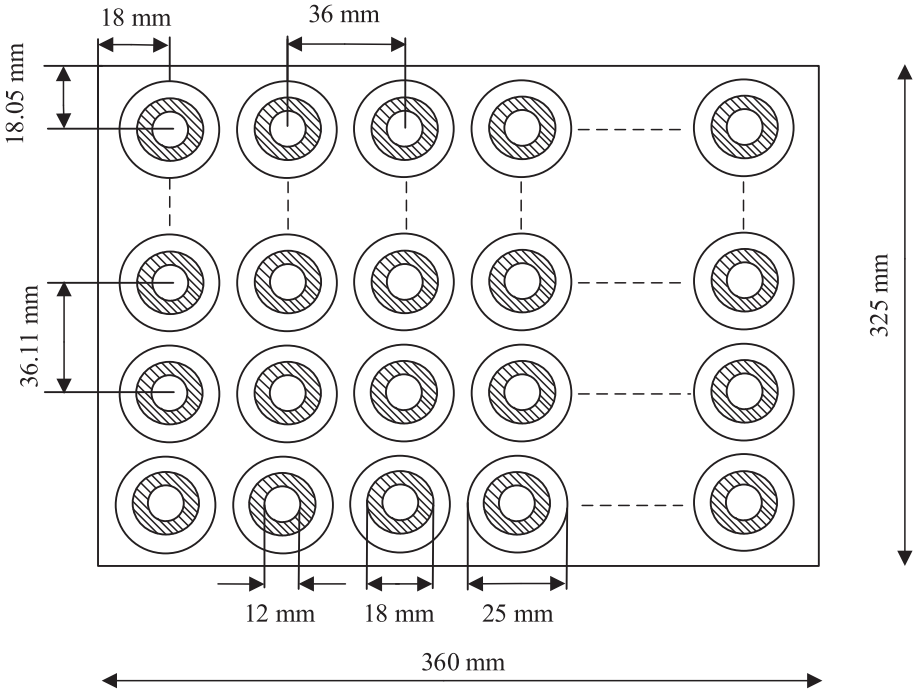

Fig. 6. Tube and fin arrangement of the finned tube heat exchanger.

Table 4
Geometric configuration parameters of the finned tube heat exchanger.

Geometric Specifications	R134a	Water	Air
Tube inner diameter (d_1)	6 mm	12 mm	10 mm
Pipe outer diameter (d_2)	9 mm	18 mm	15 mm
Fin outer diameter (D_0)	14 mm	25 mm	26 mm
Fin spacing (s)	3 mm	3 mm	3 mm
Fin length (b)	2 mm	2 mm	3 mm
Fin length (L)	5 mm	4 mm	6 mm
Thermal conductivity tube (k_T)	170 kW/mK	170 kW/mK	170 kW/mK
Thermal conductivity fin(k_f)	250 kW/mK	250 kW/mK	250 kW/mK

in two stages. In the first stage, waste heat generated from the battery cooling water is used for in-vehicle heating, while in the second stage, heat energy generated from the in-vehicle cooling process is utilized to generate electricity. The temperature difference between the PCM blocks is optimized to maintain a constant temperature, aiming to maximize electricity generation from the TEG units.

Although the theoretical number of TEGs is determined to utilize all waste heat in the system, the physical space occupied by each TEG module creates application limitations. The number of TEGs required to generate the required electricity increases depending on the amount of waste heat in the system. The maximum number of TEGs is limited by design parameters. Taking into account realistic electric vehicle dimensions, the heat exchanger dimensions are set at a maximum of 400 mm × 360 mm × 325 mm. Therefore, considering the system's space, the maximum number of TEG modules is limited to 90 TEG modules, not exceeding the total capacity. Even if the available waste heat exceeds this capacity, the number of modules is not increased, and excess heat is removed from the system. All PCM mass placed in the heat exchanger designed for these limited dimensions was melted. However, due to physical constraints, not all of the waste heat in the system could be utilized. Only the amount needed to melt the PCM mass that could be accommodated in this volume was used, and the remaining heat was removed from the system. Finned tube heat exchangers, thanks to their expanded surface area, increase heat transfer, providing more efficient heat exchange. Especially in systems operating at low temperature differences, the finned structure achieves high heat transfer capacity with compact dimensions. This improves both thermal performance and provides a design advantage by increasing the system's volumetric efficiency. The geometric structure of the layout is given in Fig. 6.

Where, pt represents the horizontal center-to-center pitch of the pipes, pc represents the vertical center-to-center distance of the pipes. The pt/2 and pc/2 values indicate the half-pitch distances between opposing pipes in this arrangement, and are particularly important for fin arrangement and flow field symmetry. The geometrical properties of the circular finned tube heat exchanger in which the PCM and TEG components are placed are given in Table 4.

The tube layout used in a finned-tube heat exchanger is designed with varying axial spacing in the horizontal and vertical directions. Radial fins located around each tube aim to increase heat transfer efficiency by increasing surface area. This configuration was chosen to balance compact design with high thermal performance. The structural layout of the TEG unit is given in Fig. 7.

The sizing of the circular finned tube, PCM-supported heat exchanger was determined based on the amount of waste heat generated in the system and the number of Thermoelectric Generators (TEGs), which were determined by the melting temperature of the PCM. The sizing calculations for the TEG-I and TEG-II units were based on the maximum waste heat values the battery could generate under different operating conditions. The technical specifications of the TEG modules used in the system is given in Table 5 [72].

In this study, paraffin wax, an organic material, was chosen as the phase change material (PCM) for the system due to its chemical stability,

Table 5
Performance and structural properties of the TGM-127–1.4–1.2 thermoelectric module.

Parameter	Value	Unit
Width of the TEG module (W_{TEG})	40	mm
Length of TEG module (L_{TEG})	40	mm
Height of TEG module (h_{TEG})	3.5	mm
Thermocouple pairs (n)	127	–
Width of the thermocouple (W_{TC})	1.4	mm
Leg length (L)	1.2	mm
Seebeck coefficient	$3.24x10^{-4}$	V/K
Thermal resistance(R_t)	1.28	K/W
Outpower (P)	7.5	W

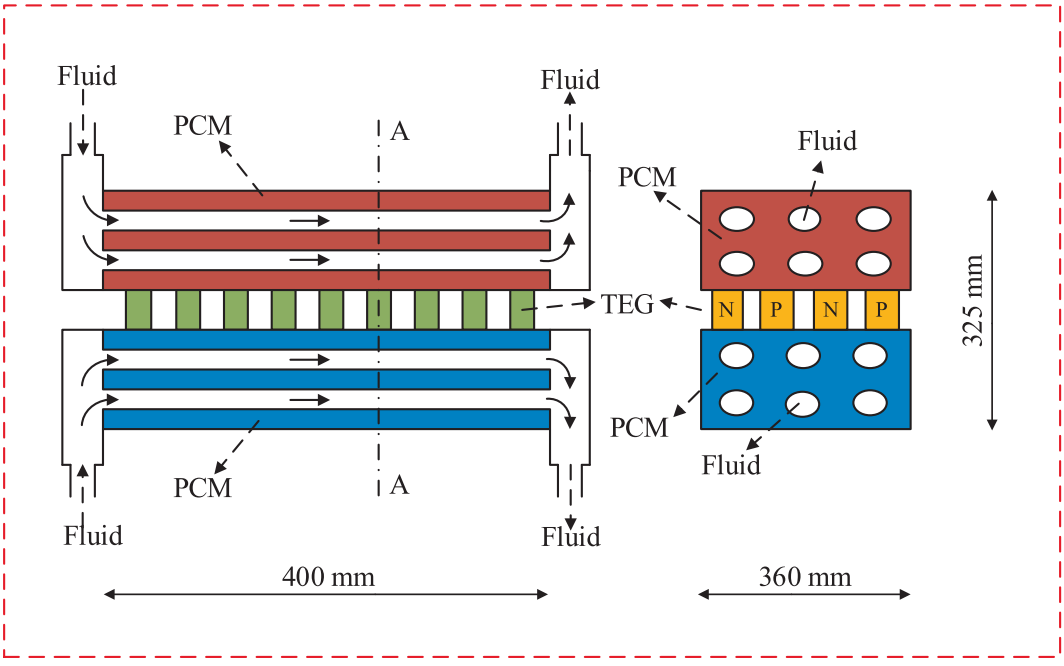

Fig. 7. Structure of PCM supported TEG unit.

Table 6
PCMs characteristic.

Characteristic	k (W/mK)	ρ_{liquid} (lt/m³)	ρ_{solid} (lt/m³)	β_{ex} (%)	$T_{melting}$ (°C)	C_p (kJ/kgK)	L_{LHC} (kJ/kg)
RT15	0.2	0.77	0.88	12.5	15	2	155
RT17	0.2	0.77	0.88	12.5	17	2	150
RT21	0.2	0.77	0.88	14	21	2	190
RT25	0.2	0.77	0.88	14	25	2	230
RT30	0.2	0.76	0.83	12.5	30	2	165
RT35	0.2	0.77	0.88	12	35	2	240
RT40	0.2	0.76	0.88	12.5	45	2	165
RT45	0.2	0.77	0.88	12	45	2	160
RT50	0.2	0.77	0.88	12.5	50	2	160
RT55	0.2	0.77	0.88	14	55	2	170
RT60	0.2	0.77	0.88	12	60	2	160

longevity, and easy availability. Furthermore, its high latent heat storage capacity in compact volumes is another important advantage that distinguishes paraffin wax [73]. The thermophysical properties of the PCMs used in the study is given in Table 6 [74].

In TEG analyses, the internal electrical resistance (R_{int}) arised depending on the thermal and electrical properties of the materials in the thermal module used [75,76].

$$R_{int} = \frac{\rho_p L_p}{A_p} + \frac{\rho_n L_n}{A_n} \tag{6}$$

where, A_p and A_n represent the cross-sectional areas of the p-type and n-type semiconductors, respectively, and ρp and ρn represent the electrical resistivity of the respective materials. L_p and L_n represent the lengths of the p-type and n-type thermoelectric elements, respectively. The thermal conductivity K_{TEG} (W/K) of the thermoelectric conductor pair is:

$$K_{TEG} = \frac{A_p k_p}{L_p} + \frac{A_n k_n}{L_n} \tag{7}$$

where, k_p and k_n represent the thermal conductivity coefficients of p-type and n-type thermoelectric materials, respectively [77]. At maximum power point condition, i.e. when the load resistance is equal to the internal resistance ($R_L = R_{int}$), the module current is given by [77]:

$$I = \frac{\alpha\,(T_{hot} - T_{cold})}{2R} \tag{8}$$

where, α is the Seebeck coefficient of the thermoelectric module *(V/K)*, T_{hot} and T_{cold}, with T_{hot} and T_{cold} indicating the temperatures at the hot and cold junctions, respectively. *(K)*, R_L is the external load resistance *(Ω)*. Based on the Seebeck effect, the electrical output of a thermoelectric generator is enhanced as the temperature gradient between the two sides increases. Output power is given [78]:

$$P = I^2 R = \alpha^2 (T_{hot} - T_{cold})^2 \frac{R_o}{(R_L + R)^2} \tag{9}$$

The maximum output power (P_{max}) of a TEG module is produced when the external load resistance is equal to its internal electrical resistance. P_{max} is given [79]:

$$P_{max} = I^2 R = \frac{\alpha^2 (T_{hot} - T_{cold})^2}{4R} \tag{10}$$

The heat flow at the hot junction was expressed by the following relation [80]:

$$\dot{Q}_{hot} = \left((\alpha T_{hot} I) - \left(\frac{1}{2} I^2 R \right) + K_{TEG}\,(T_{hot} - T_{cold}) \right) \tag{11}$$

The corresponding cold-side heat rate reads:

$$\dot{Q}_{cold} = \left((\alpha T_{cold} I) + \left(\frac{1}{2} I^2 R \right) + K_{TEG}\,(T_{hot} - T_{cold}) \right) \tag{12}$$

where, legs thermal conductance *(K_{TEG})*.Where, T_{hot} and T_{cold} represent the temperatures on the hot and cold surfaces of the TEG module, respectively. TEG efficiency is,

$$\eta = \frac{P_{Out}}{\dot{Q}_{hot}} \tag{13}$$

The number of TEG modules to be placed on the heat exchanger depending on the amount of waste heat ($\dot{Q}_{WH}$) is expressed as N_{TEG}.

$$N_{TEG} = \frac{\dot{Q}_{WH}}{\dot{Q}_{hot}\, n} \tag{14}$$

where, n represents the number of thermocouple pairs in each TEG module. After determining the total number of TEG modules, the heat exchanger sizing process was completed. At this stage, the horizontal and vertical placement of the TEG modules is optimally arranged. The amount of heat passing through a single tube within the heat exchanger is expressed as follows.

$$\dot{Q}_{pipe} = \underbrace{\frac{1}{\frac{1}{\frac{Nu_i k_i}{D}}\frac{A_o}{A_i} + \frac{A_i}{2\pi k_{pipe}} \ln\left(\frac{r_o}{d_i}\right) + \frac{A_o}{2\pi k_{fin}} \ln\left(\frac{d_o}{d_i}\right) + \frac{1}{\eta_k} \frac{1}{\frac{Nu_{PCM} k_{PCM}}{D}}}}_{U_{pipe}} A_{pipe} \left(T_{PCM-melt} - \left(\frac{T_{in} + T_{out}}{2} \right) \right) \tag{15}$$

where, k_{pipe} represents the heat transfer coefficient of the pipe material; k_i represents the heat transfer coefficient of the fluid passing through the pipe, and k_{PCM} represents the PCM heat transfer coefficient. d_i and d_o are the inner and outer radii of the pipe, respectively. Apipe represents the heat transfer surface area of the pipe. $T_{PCM\text{-}melt}$ is the melting temperature of the PCM; Nu_i is the Nusselt number of the fluid within the pipe; and Nu_{PCM} is the Nusselt number of the PCM [80]. The efficiency of the heat exchanger was taken as 0.98, taking into account the conduction losses [81]. A_{pipe} is given:

$$A_{pipe} = A_{bare} + \eta_f A_{fin} \tag{16}$$

$$A_{bare} = 2\pi r_1 L \tag{17}$$

$$A_{fin,single} = 2\pi r_2 t_f + \pi\left(r_2^2 - r_1^2\right) \tag{18}$$

where L is lelght of tube, A_{bare} is bare tube surface area, r_1 is the tube outer radius, t_f is fin thickness, and r_2 is fin outer radius. The overall heat transfer coefficient for a circular finned tube is given [82,83]:

$$\frac{1}{U_T} = \frac{1}{\eta_f h_o} + \frac{\delta_t}{k_t} + \frac{1}{h_i} \tag{19}$$

where h_o is the external convective heat transfer coefficient corresponding to the finned surface, h_i is internal coefficient for the tube side, δ_t indicates the tube wall thickness, k_t is tube material thermal conductivity, and η_f is fin efficiency. For circular fins, fin efficiency is given:

$$\eta_f = \frac{\tanh(mL_f)}{mL_f} \tag{20}$$

$$m = \sqrt{\frac{2h_i}{t_f k_{fin}}} \tag{21}$$

where L_f is fin lenght, k_{fin} is defined as the fin material's thermal conductivity. In the design and thermal analysis of both TEG-I and TEG-II systems, circular finned tubes are utilized as heat exchangers, where the outer surface of the tubes is surrounded by phase change material (PCM). Accordingly, U_{pipe} incorporates the convective heat transfer from the PCM side. In both systems, the external convective heat transfer

coefficient (h_o) is assumed to be the same, since PCM is used as the surrounding medium in both configurations.

$$h_o = \frac{Nu_{PCM} k_{PCM}}{D} \tag{22}$$

Nu_{PCM} is calculated based on natural convection, using the following correlation [84]:

$$Nu_{PCM} = \frac{0.35(GrPr)^{1/4}}{\left(1 - \left(\frac{0.143}{Pr}\right)^{9/16}\right)^{4/9}} \tag{23}$$

In the evaluation of the system for the TEG-I and TEG-II modules, the internal convective heat transfer coefficients vary as a result of variations in the working fluids used inside the tubes. In the TEG-I unit, and its internal convective heat transfer coefficient (hi) is calculated using empirical correlations for forced convection of gaseous flows. For the under laminar flow conditions, the Nusselt number is calculated using the empirical correlation given in [85]:

$$Nu_{fg} = 0.664\, Re^{1/2} Pr^{1/3} \tag{24}$$

where Re corresponds to the Reynolds number, while Pr corresponds to the Prandtl number.

$$Re = \frac{\dot{m} D}{A\,\mu} \tag{25}$$

$$Pr = \frac{C_p \mu}{k} \tag{26}$$

where D is tube diameter, $\dot{m}$ is mass flow rate, A is cross-sectional area of the tube and μ is dynamic viscosity.

$$Gr = \frac{g\beta(T_s - T_{ref})L^3}{\nu^2} \tag{27}$$

where, g Gravitational acceleration (m/s^2), β Volumetric thermal expansion coefficient ($1/K$), T_s Surface temperature (K), T_{ref} fluid temperature (K), L length (m), ν Kinematic viscosity (m^2/s).

In contrast, for the TEG-I unit, where liquid water circulates inside the tube to transfer heat to the PCM, the internal convective heat transfer coefficient is determined based on the thermal properties of water. Under laminar flow conditions, the Nusselt number for fully developed flow in a circular tube is taken as:

$$Nu = 3.66 \tag{28}$$

Nu number for turbulent flow:

$$Nu = \frac{f}{8}(Re - 1000)\frac{Pr}{1 + 12.7\sqrt{\frac{f}{8}}\left(Pr^{2/3} - 1\right)}(0.5 < Pr < 2000\, and\, 3000 < Re < 5 \times 10^6) \tag{29}$$

$$f = (0.79\ln(Re) - 1.64)^{-2} \tag{30}$$

In the TEG-II module, the hot surface is in contact with the dual-phase PCM3, while the cold surface is in contact with the air. In this region, heat transfer from PCM3 to the TEG is based on dual-phase convection behavior. Heat transfer on the other side of the TEG, surrounded by PCM4, was modeled using appropriate Nusselt number correlations [86].

$$Nu_{air} = 0,.023 Re^{0.8} Pr^{0.3} \tag{31}$$

Convection heat transfer due to air flow within a pipe was calculated using an empirical correlation based on the Nusselt number. The Nusselt number used in this context was related to the Nuair, Reynolds Re, and Prandtl Pr numbers. These numbers, commonly used for the turbulent regime, was determined by the following relations. Based on the relevant parameters, the air-side convection heat transfer coefficient h was calculated using the equation given below [87].

$$h = \frac{0.023.Re^{0.8}.Pr^{0.3}.k}{Dh} \tag{32}$$

In regions operating with dual-phase fluids (PCM2 and PCM3), classical single-phase Nusselt correlations was not used. Therefore, heat transfer in these regions varies depending on the fluid's vaporization quality and phase distribution, and is evaluated using the Chen correlation, widely used in the literature. This correlation allows the average heat transfer coefficient to be calculated by taking into account the heat transfer coefficients in the liquid and vapor phases and the fluid's dryness [88].

The convective heat transfer coefficient for the two-phase flow (h) is the sum of bubble boiling contribution (h_k) and forced convection contribution (h_z) [88]:

$$h = h_k + h_z \tag{33}$$

The Bubble Boiling Component (h_k) represents the enhanced heat transfer caused by vapor bubble formation at the heated surface:

$$h_k = 0,023\left(\frac{G.(1-x).D}{\mu_f}\right)^{0,8} Pr_f^{0,4}\frac{\lambda_f}{D}.F \tag{34}$$

where G is the mass flux (kg/m^{2}s), x is the vapor quality, D is the hydraulic diameter (m), μ_f, λ_f, and Pr_f are the dynamic viscosity, thermal conductivity, and Prandtl number of the liquid phase, respectively, F is the forced convection–boiling correction factor given by [88]:

$$\begin{aligned} F &= 1.0 && \frac{1}{X_{tt}} \le 0.1 \\ F &= 0.235\left(\frac{1}{X_{tt}} + 0,213\right)^{0,736} && \frac{1}{X_{tt}} > 0.1 \end{aligned} \tag{35}$$

where X_{tt} *is the* Martinelli parameter given by [88]:

$$X_{tt} = \left(\frac{1-x}{x}\right)^{0,9}\left(\frac{\rho_g}{\rho_f}\right)^{0,5}\left(\frac{\mu_f}{\mu_g}\right)^{0,1} \tag{36}$$

The Forced Convection Component (h_z) accounts for sensible heat transfer due to the motion of the fluid along the heated surface:

$$h_z = 0,00122\left(\frac{k_f^{0,79} C_{pf}^{0,45} \rho_f^{0,49}}{\sigma^{0,5}\mu_f^{0,29} h_{fg}^{0,24} \rho_g^{0,24}}\right)\Delta T_d^{0,24}\Delta P_d^{0,75} S \tag{37}$$

where ΔT_d is the temperature difference, ΔP_d is the pressure difference, k_f is thermal conductivity of the liquid phase. C_{pf} is specific heat of the liquid phase. μ_f *and* ρ_g are viscosity of the liquid and density of the vapor phases, respectively. σ is surface tension, and h_{fg} is the latent heat of vaporization. S is correction factor based on the Reynolds number (Re) [88]:

$$\begin{aligned} S &= \left(1 + 0,12Re^{1,14}\right)^{-1} && Re \le 32.5 \\ S &= \left(1 + 0,42Re^{0,78}\right)^{-1} && 32.5 < Re < 70 \\ S &= 0.1 && Re \ge 70 \end{aligned} \tag{38}$$

with

$$Re = F^{1,25}\left(\frac{G.(1-x).D_h}{\mu_f}\right) \tag{39}$$

The energy balance used in PCM melting analysis consists of the effective heat flux entering the control volume $\dot{Q}_{in}$, the heat flux transferred to the $\dot{Q}_{TEG}$, and the external losses $\dot{Q}_{loss}$; the relevant expressions was given below [80].

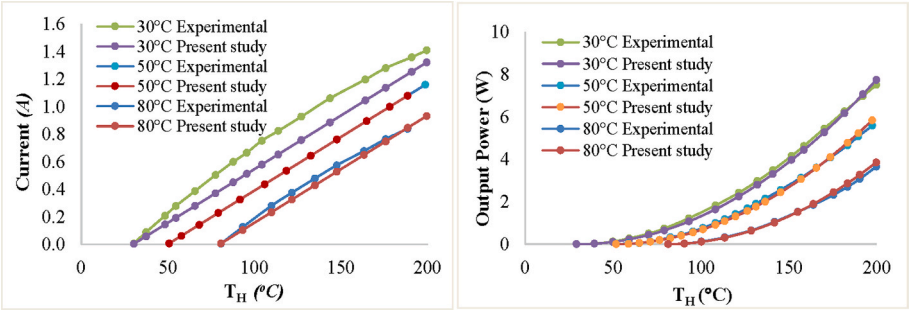

Fig. 8. Comparative analysis of current and power outputs of TEG under different cold surface temperatures, depending on the hot surface temperature.

Table 7
Evaluation of error statistics between TEG's performance curves and simulation results.

	Output power (W)				Current (A)		
T_C (°C)	R^2	MAPE (%)	RMSE (%)	R^2	MAPE (%)	RMSE (%)
30	0.99	7.58	14.82	0.98	20.16	13.34
50	0.99	6.39	10.35	0.99	15.12	9.19
80	0.99	4.96	10.06	0.99	7.29	3.32

$$\dot{Q}_{in} = n_{HX}\, U_{pipe} A_{pipe}\left(T_{PCM-melt} - \left(\frac{T_{in}+T_{out}}{2}\right)\right) \quad (40)$$

$\dot{Q}_{in}$ is the heat flux entering the control volume, U_{pipe} is the effective total heat transfer coefficient between the pipe and PCM, A_{pipe} is the effective heat transfer area of the pipe outer surface, and n_{HX} is the heat exchanger efficiency.

By conservation of energy for the PCM:

$$\dot{Q}_{in} = \dot{Q}_{TEG} + \dot{Q}_{loss} \quad (41)$$

$\dot{Q}_{TEG}$ is the heat flux (W) transferred to the TEG, $\dot{Q}_{loss}$ is the heat loss from the enclosure to the outside environment (W). The amount of energy that PCM can store during the melting process is;

$$Q_{PCM} = m_{PCM} Le \quad (42)$$

where, m_{PCM} is defined as the PCM mass (kg), Le is the latent heat of the PCM (kJ/kg). In this design, Because the PCM operates in a closed volume, losses were not taken into account. [89].

4. Modeling of compressor

The required power of the compressor is given by [90]:

$$\dot{W}_c = \dot{m} c_p \frac{T_i}{\eta_c}\left[\left(\frac{P_0}{P_i}\right)^{\frac{k-1}{k}} - 1\right] \quad (43)$$

where C_p signifies the specific heat (kJ/kgK), η_c represents the compressor efficiency (80 % [90]), and k designates the isentropic exponent.

5. Model validation

The system was designed to simultaneously provide heating and cooling functions, in addition to electricity generation. The thermoelectric generator module included in the design was compared with manufacturer data from the Kryotherm TGM-127–1.4–1.2 catalog [72], and this validation process is given in Fig. 8. The error statistics for the simulation results using the thermoelectric module's performance curves is given in Table 7.

The validation criteria in Table 7 are consistent with validation thresholds commonly used in the literature, supporting the validity of the model. The range of R^2 is 0.98–0.99 for power and current indicates very high fit; MAPE is 4.96–7.58 % for power and 7.29–15.12 % for current under most conditions. Generally, <10 % is considered high accuracy, and 10–20 % is considered acceptable. The RMSE range of 3.32–14.82 % indicates that the model's calculations for the TEG system was validated in accordance with the reference experimental study. In another validation process, if the heat exchangers used in the system used different fluids, the validation process was performed separately for three different fluids, the water side, the dual-phase fluid side, and the air side. The results obtained for each operating condition was compared with studies in the literature. As part of this validation, comparisons were made with three separate articles, specifically for the R134a side, the water side, and the air side. During the validation process, the working conditions in References were adapted to this study. The results is given in Table 8.

According to Table 8, The heat exchanger sizing parameters for R134a, water, and air are in close agreement with the literature. Reynolds numbers of 2.6–5.6 %, in-tube heat transfer coefficients (h), and overall heat transfer coefficients (U) mostly match within 2.5–6.2 % of the sample. Nusselt number (Nu) values similarly deviate between 2.7–5.3 %, and the 11.1 % difference in velocity is attributable to possible geometry/boundary condition and system design changes. This comparison supports the reliability of the correlation and sizing method used in the system for all R134a-side, water-side, and air-side fluid conditions.

6. Energy and exergy analysis.

The performance of the waste heat recovery system integrated with

Table 8
Comparison of heat exchanger design parameters for R134a, water and air fluids with reference studies in the literature.

		R134a			Water			Air		
		Present study	Ref. [91]	Dif. (%)	Present study	Ref. [92]	Dif. (%)	Present study	Ref. [93]	Dif. (%)
Number of tubes	Nt	46	48	4.16	51	49	3.91	47	44	6.38
Fluid velocity in tube	Vt	0.983	0.916	7.83	0.024	0.027	11.1	2.48	2.5	0.67
Reynold number	Re	3823	3927	2.62	8241	7999	2.93	1429.9	1509.20	5.58
Heat transfer coefficient	h	6723.13	7020	4.23	1969.08	1898.64	2.66	162.807	158.47	2.74
Overall heat transfer coefficient	U	2759	2587	6.20	1111.63	1084.61	2.51	85.9	89.82	4.56
Nusselt Number	Nu	–	–	–	66.54	70.05	5.27	66.77	65	2.73

Table 9
Energy and exergy balances of the HPAC system.

Components	Energy balance	Exergy balance
Evap	$\dot{Q}_{Ev} = \left(\dot{m}_6 h_6 - \dot{m}_5 h_5\right) - (\dot{m}_4 h_4 - \dot{m}_1 h_1) + \dot{W}_{TEG1}$	$\dot{E}x_{d,Evap} = \dot{m}_6\psi_6 - \dot{m}_5\psi_5 + \dot{m}_4\psi_4 - \dot{m}_1\psi_1 - \left(1 - \frac{T_0}{T_1}\right)\dot{Q}_{Ev}$
Comp	$\dot{W}_{Comp} = \dot{m}_2 h_2 - \dot{m}_1 h_1$	$\dot{E}x_{d,Comp} = \dot{m}_2\psi_2 - \dot{m}_1\psi_1 \pm \dot{m}_{11}\psi_{11} + \left(1 - \frac{T_0}{T_2}\right)\dot{Q}_{Comp}$
Cond	$\dot{Q}_{con} = (\dot{m}_2 h_2 - \dot{m}_3 h_3) - (\dot{m}_9 h_9 - \dot{m}_{10} h_{10}) + \dot{W}_{TEG2}$	$\dot{E}x_{d,Con} = \dot{m}_2\psi_2 - \dot{m}_3\psi_3 + \dot{m}_9\psi_9 - \dot{m}_{10}\psi_{10} + \left(1 - \frac{T_0}{T_3}\right)\dot{Q}_{Con}$
ExV	$\dot{m}_5 h_5 = \dot{m}_6 h_6$	$\dot{E}x_{d,Exv} = \dot{m}_3\psi_3 - \dot{m}_4\psi_4$
Pump	$\dot{W}_{pump} = (\dot{m}_5 h_5 - \dot{m}_6 h_6)$	$\dot{W}_{pump} = (\dot{m}_5\psi_5 - \dot{m}_6\psi_6)$
Fan	$\dot{W}_{fan}$	$\dot{E}_{x,fan}$
TEG1	$\dot{W}_{TEG1} = \left(\dot{m}_6 h_6 - \dot{m}_5 h_5\right) - \dot{Q}_{PCM1} - \dot{Q}_{PCM2} - (\dot{m}_4 h_4 - \dot{m}_1 h_1)\dot{Q}_{PCM1} = 0.98\left(\dot{m}_6 h_6 - \dot{m}_5 h_5\right)\dot{Q}_{PCM2} = 0.98(\dot{m}_4 h_4 - \dot{m}_1 h_1)$	$\dot{W}_{TEG1} = (\dot{m}_6\psi_6 - \dot{m}_5\psi_5) - (\dot{m}_4\psi_4 - \dot{m}_1\psi_1) - \left(1 - \frac{T_0}{T_{PCM1}}\right)\dot{Q}_{PCM1} - \left(1 - \frac{T_0}{T_{PCM2}}\right)\dot{Q}_{PCM2}$
TEG2	$\dot{W}_{TEG2} = \left(\dot{m}_2 h_2 - \dot{m}_3 h_3\right) - \dot{Q}_{PCM3} - \dot{Q}_{PCM4} - (\dot{m}_9 h_9 - \dot{m}_{10} h_{10})\dot{Q}_{PCM3} = 0.98\left(\dot{m}_2 h_2 - \dot{m}_3 h_3\right)\dot{Q}_{PCM4} = 0.98(\dot{m}_9 h_9 - \dot{m}_{10} h_{10})$	$\dot{W}_{TEG2} = (\dot{m}_2\psi_2 - \dot{m}_3\psi_3) - (\dot{m}_9\psi_9 - \dot{m}_{10}\psi_{10}) - \left(1 - \frac{T_0}{T_{PCM3}}\right)\dot{Q}_{PCM3} - \left(1 - \frac{T_0}{T_{PCM4}}\right)\dot{Q}_{PCM4}$

TEG and PCM for vehicle heating and cooling was also be examined from a thermodynamic perspective. In this context, the system's energy efficiency and potential for conversion to work was evaluated in detail through energy and exergy analyses.

Expressions regarding mass conservation, energy conservation and exergy balances is given as follows:

$$\Sigma\dot{m}_i - \Sigma\dot{m}_o = 0 \tag{44}$$

$$\dot{Q} - \dot{W} + \Sigma\left(\dot{m}_i\dot{h}_i\right) - \Sigma\left(\dot{m}_o\dot{h}_o\right) = 0 \tag{45}$$

$$\left(1 - \frac{T_o}{T}\right)\dot{Q} - \dot{W} - \Sigma\left(\dot{m}_i\psi_i\right) - \Sigma\left(\dot{m}_o\psi_o\right) - \dot{E}x_d = 0 \tag{46}$$

where, the Q term represents heat transfer, the $\dot{W}$ term represents work transfer, and the ṁ represents the mass flow rate. The subscripts i and o represent the inlet and outlet conditions, respectively. The exergy of the flow is defined as:

$$\psi = (h - h_0) - T_0(s - s_0) \tag{47}$$

The symbols h and s represent the specific enthalpy and specific entropy at a specific thermodynamic state, respectively. The subscript "o" indicates the environmental reference state, defined at −40 °C and 1 atm (101.325 kPa) pressure. The energy and exergy balance equations used in the designed system is given in Table 9, respectively.

Energy and Exergy efficiencies of cooling, heating and the overall system:

$$COP_H = \frac{\dot{Q}_{con}}{\dot{W}_{pump} + \dot{W}_{Comp} - (\dot{W}_{TEG1} + \dot{W}_{TEG2})} \tag{48}$$

$$COP_C = \frac{\dot{Q}_{ev}}{\dot{W}_{fan} + \dot{W}_{Comp} - \dot{W}_{TEG2}} \tag{49}$$

$$\varepsilon_H = 1 - \frac{\dot{E}x_{d,Con} + \dot{W}_{TEG2}}{\left(\dot{m}_2\psi_2 + \dot{m}_9\psi_9\right)} \tag{50}$$

$$\varepsilon_C = 1 - \frac{\dot{E}x_{d,Ev} + \dot{W}_{TEG2)}}{(\dot{m}_2\psi_2 + \dot{m}_9\psi_9)} \tag{51}$$

$$\varepsilon_{overall,H} = 1 - \frac{(\dot{m}_3\psi_3 + \dot{m}_{10}\psi_{10})}{(\dot{m}_2\psi_2 + \dot{m}_9\psi_9 + \dot{W}_{Comp} - \left(\dot{W}_{TEG1} + \dot{W}_{TEG2}\right) + \dot{W}_{Pump}} \tag{52}$$

7. Auxiliary systems

One of the factors affecting the total energy requirement in the system is the power consumption of auxiliary equipment. In this context, the pump power for circulation in the battery cooling circuit and the fan power for air circulation was calculated. The power of both equipment was calculated using the general equation below, taking into account the pressure difference applied to the fluid and the volumetric flow rate.

$$\dot{Q} = \dot{m}.c_p.\Delta T \tag{53}$$

where $\dot{Q}$ is the waste heat energy, $\dot{m}$ is the mass flow rate, ΔT is the temperature difference

$$\dot{V} = \frac{\dot{m}}{\rho} \tag{54}$$

where, $\dot{V}$ represents the volumetric flow rate and ρ represents the fluid density. The pump power and fan power required for the system are given as follows.

$$W_{p,f} = \frac{\Delta P.\dot{V}}{\eta} \tag{55}$$

In this equation, ΔP represents the pressure difference (Pa), V represents the volumetric flow rate (m^3/s), and η represents the mechanical efficiency of the equipment. Pump power was calculated separately for liquid fluids and fan power for gaseous fluids such as air, and their effects on system energy consumption were evaluated. For the pump, ΔP = 250.000 Pa, efficiency η = 0.70, and for the fan, ΔP = 125 Pa, efficiency η = 0.55 [94–96].

8. Economic analysis

The NPV method was used to analyze the economic performance of a new HPAC system over its entire lifespan, as NPV calculates the time value of economic performance [97,98]. In this context, the HPAC was assumed to have an average operating time of 2 h per day during a 150-day heating season. While the average lifespan of common systems is 20 years, it was assumed to be 8 years based on the manufacturer's warranty period for the batteries. The NPV of a system is given as follows [99,100]:

$$\mathrm{NPV} = + \sum_{t=0}^{n} \frac{B_t}{(1+r)^t} - C_0 \tag{56}$$

where I_o represents the initial investment cost, n denotes the

Table 10
Component costs.

Component	Cost function	References
Condenser (€/m^2)	$297A$	[103]
Evaporator (€/m^2)	$190 + 310A$	[104]
Heat Exchanger (€/m^2)	$297A$	[103]
ExV	$C_{exv} = 114.\dot{m}$	[105]
Compressor ($/m^2)	$\frac{71,1.\dot{m}}{0,91-\eta_{comp}}\left(\frac{P_o}{P_i}\right)ln\left(\frac{P_o}{P_i}\right)$	[106]
Paraffin Wax (€/kg)	8.95	[107]
TEG (€)	21.89	[108]
Pump ($/m^2)	$1026\left(\frac{\dot{W}_p}{300}\right)^{0.25}$	[109]
Fann ($/m^2)	$1026\left(\frac{\dot{W}_f}{300}\right)^{0.25}$	[109]
Operation and maintenance costs	1.5 % of the installation cost	[110]
Discount rate (%)	$r = 6$ %	[111]
Depreciation period, n (year)	8	–
*1€=1,09$ **1TL = 0.054$		

depreciation period, B_t signifies the cash flow in year t, and r denotes the discount rate. Since there is no gaining from the system, the B_t is determined based on the electricity saving in comparison to the conventional system:

$$B_t = C_E - C_{mr} \quad (57)$$

where C_e indicates the cost of electricity savings, and C_{mr} indicates maintenance and repair costs. Since the maintenance and repair cost is equal for the new concept (NC) and conventional system (CS), the B_t can be rewritten as:

$$B_t = C_e \quad (58)$$

The total electricity saving cost for 300 working hours per year is given by:

$$C_e = \dot{W}_e c_e 300 \quad (59)$$

where ce is the unit electricity price, and We is the saved electricity in a year. Since the evaporator itself is a Li-Ion battery, the initial investment cost for HPAC includes the cost of the compressor (C_{Comp}), condenser (C_{Cond}), fann (C_{Fann}), Pupm (C_{pump}), PCM (C_{PCM}), TEG (C_{TEG}) and expansion valve (C_{Exv}). The total investment costs of the new HPAC and conventional system (CS) are then given as [101,102]:

$$C_{NC} = C_{Ev} + C_{Cond} + C_{Comp} + C_{pump} + C_{fann} + C_{Exv} + C_{PCM} + C_{TEG1,} + C_{TEG,2} \quad (60)$$

$$C_{CS} = C_{Ev} + C_{Cond} + C_{Comp} + C_{pump} + + C_{fann} + C_{Exv} \quad (61)$$

$$C_{NC} = C_{CS} + C_{PCM} + C_{TEG1,} + C_{TEG,2} \quad (62)$$

$$C_{EG} = C_{TEG1} + C_{TEG2} \quad (63)$$

The initial investment cost of the system is determined by subtracting the salvage cost (C_{SC}, assumed as 10 % of the total investment) from the total investment cost. So, the initial investment cost is given by:

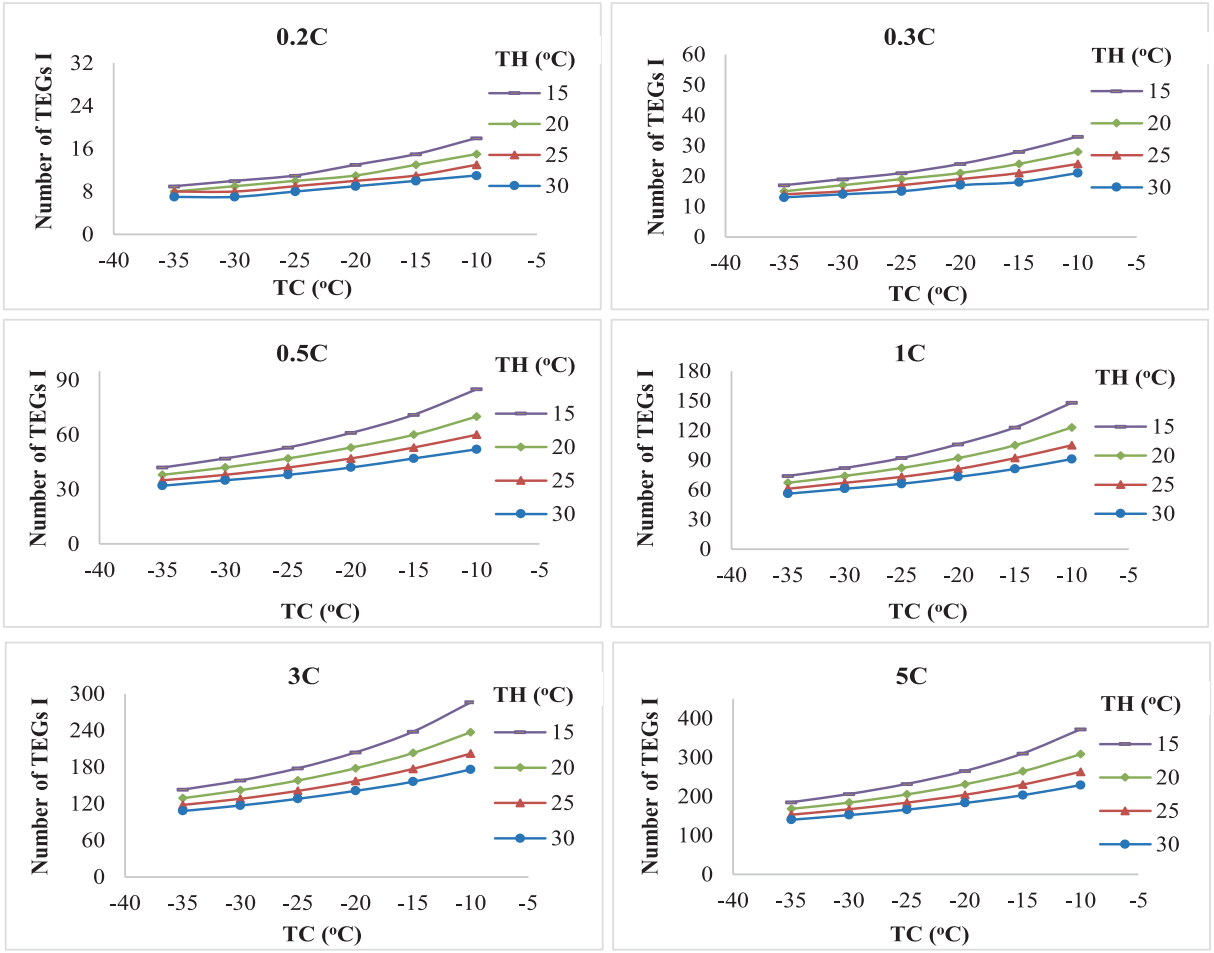

Fig. 9. Number of TEG I modules required at different C rates depending on PCM temperature.

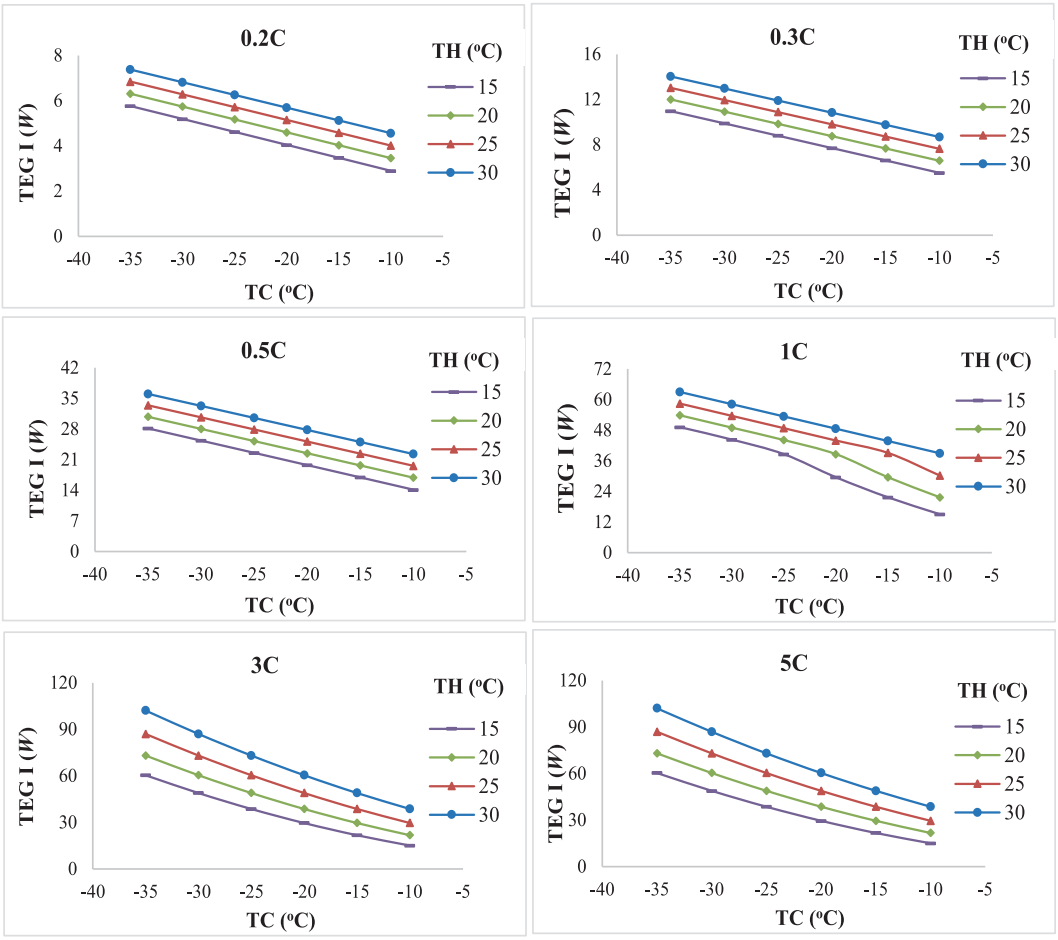

Fig. 10. Change of TEG-I output power depending on PCM temperature difference at different C-rates.

$$C_{O,NC} = C_{NC} - C_{CS,NC} \tag{64}$$

$$C_{O,CS} = C_{CS} - C_{CS,CS} \tag{65}$$

As the NPV analysis is based on the comparative savings with the conventional system, the initial investment is rewritten as:

$$C_o = C_{o,NC} - C_{o,CS} \tag{66}$$

The NPV analysis was structured to reflect the component and operational differences between the two systems. The NC structure includes a TEG and PCM for power generation, while the CS does not; therefore, the initial investment cost difference stems from the TEG and PCM in the NC. Furthermore, due to differences in design parameters, the compressor powers are not equal in the two systems. In the NC, the electricity generated from the TEGs reduces energy costs and improves cash flow. Therefore, the NPV was determined by considering the differences in compressor power and the electricity generated from the TEG together. The equations used to calculate the cost of the designed heating system is given in Table 10.

The payback period indicates how long it takes for an investment to cover its initial cost through cumulative cash flows in present value. In this study, DPB is calculated using the same discount rate r used in the NPV section and the initial cost C_0.

$$B_t^{(d)} = \frac{B_t}{(1+r)^t} \tag{67}$$

B_t is net cash flow in t year, r is discount rate, t is year index, B_t^d The present value (discounted value) of Bt.

$$S_t = \sum_{i=1}^{t} B_i^{(d)} \tag{68}$$

S_t is the sum of the present values of all net cash flows occurring up to the end of year t (cumulative discounted total), Bi, net cash flow in year i.

9. Result and discussion

To determine the required number of TEG modules based on the available waste heat, the output power that could be generated from this heat was calculated. The calculations was based on the technical data of the Kryotherm TGM-127–1.4–1.2 module. The number of TEG modules required to generate electrical energy from the recovered waste heat was then calculated. The change in the number of TEG modules required to convert waste heat into electrical energy as a function of PCM temperatures under different operating conditions is given in Fig. 9.

According to Fig. 9, The graph shows the change in the number of TEG-I modules required to achieve the desired electrical power at different battery discharge rates (0.2C–5C) and various temperature differences. At 0.2C, the minimum number of modules is 7 at TH = 30 °C and TC = −35 °C, while the maximum is 18 at TH = 5°C and TC = 0°C. At 0.3C, these values range from 13 to 33, at 0.5C 32–85, at 1C 56–148, at 3C 108–286, and at 5C 140–372, respectively. As seen in all graphs, as the temperature difference decreases (i.e., as the TH-TC difference decreases), the power produced by each TEG decreases due to the decrease in Seebeck voltage. Therefore, more modules are required to achieve the same total power. Furthermore, as the C ratio increases, the amount of waste heat generated from the battery increases, thus increasing the

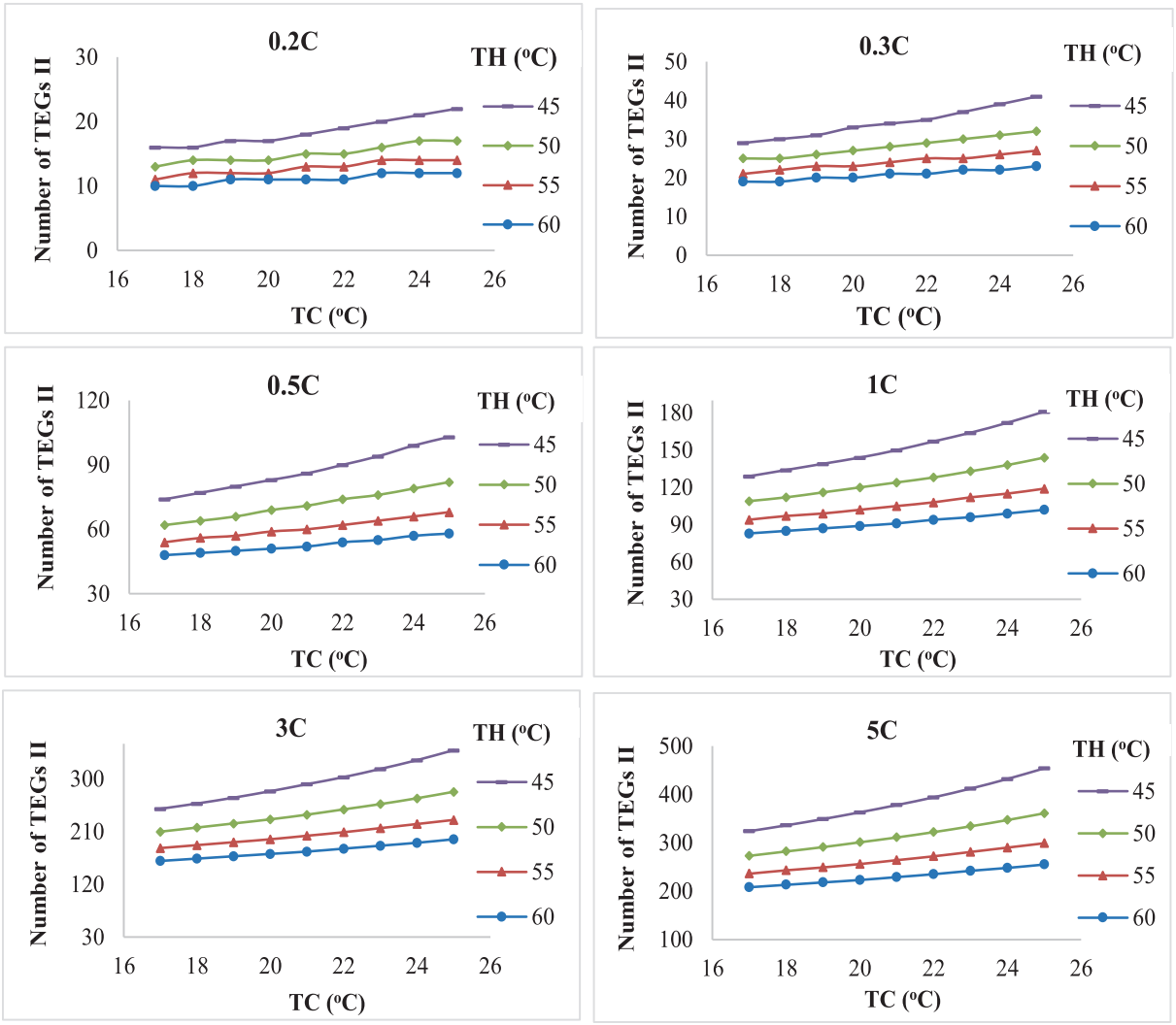

Fig. 11. Change in the number of modules required for the TEG-II unit at different C-rate values.

system's power demand. Consequently, the number of TEG modules required at each temperature level also increases. This demonstrates that not only the temperature difference but also the battery load profile is a critical determinant of system sizing. The change in TEG output power under different PCM temperatures and operating conditions is given in Fig. 10.

According to Fig. 10, the output power of TEG-I varies with the temperature difference of the PCM as the battery operates at different C-rates. At all discharge rates, the output power increases linearly as the temperature difference increases (as TH decreases while TC remains constant). At a 0.2C-rate, the output power was approximately 2.6 W at a $\Delta T = 15$ °C difference, reaching 8.2 W at a $\Delta T = 65$ °C difference. Similarly, at a 0.3C rate, the output power ranged from 4.1 W to 15.5 W, and at a 0.5C-rate, it ranged from 7.2 W to 40.5 W. At these low C-rates, because the thermal energy obtained from the battery is limited and all 90 TEG modules can be installed in the system, the output power directly represents the actual operating values. At a 1C-rate, calculations were made within some temperature ranges without exceeding the 90 TEG limit in the system. However, due to the excess heat energy generated at high temperature differences, the output power was adjusted accordingly. The same applies to the 3C and 5C rates. Because the thermal energy generated from the battery at these rates is quite high, the number of TEGs exceeds 90 in all parameters. All calculated output powers was limited to a maximum of 90 TEG modules. Therefore, the maximum output power achieved at 1C, 3C, and 5C rates is limited to approximately 102 W for all three. As the discharge rate increases, the amount of waste heat released from the battery increases, resulting in a higher heat energy transfer to the TEG, and the output power increases significantly. Similarly, as the temperature difference increases, the temperature gradient across the TEG increases, and electricity generation becomes more efficient due to the Seebeck effect. The change in the number of TEG II modules required to convert waste heat into electrical energy at different operating conditions and PCM temperatures is given in Fig. 11.

According to Fig. 11, The figure was showed the total number of TEG II modules required in the system, based on the electrical power the TEG II unit can generate under different battery C ratios and PCM temperature differences. In each graph, the hot surface temperature (TH) of the TEG was evaluated between 35 °C and 60 °C, and the cold surface temperature (TC) was evaluated between 17 °C and 26 °C. In these analyses, as the electrical power generated by the TEG II is reduced, the number of modules required to meet a given waste heat level increases. In particular, when the temperature difference (TH-TC) decreases, the number of TEGs required increases rapidly because the power generated by a single TEG decreases. At discharge rates as low as 0.2C, the TEG II's demand remained at its lowest. While approximately 10 TEG modules were sufficient at TH = 60 °C and TC = 17 °C, this number increased to 22 at low temperature differentials such as TH = 35 °C and TC = 26 °C. On the other hand, at high C values such as 5C, the amount of waste heat generated in the system increased, requiring significantly more TEG

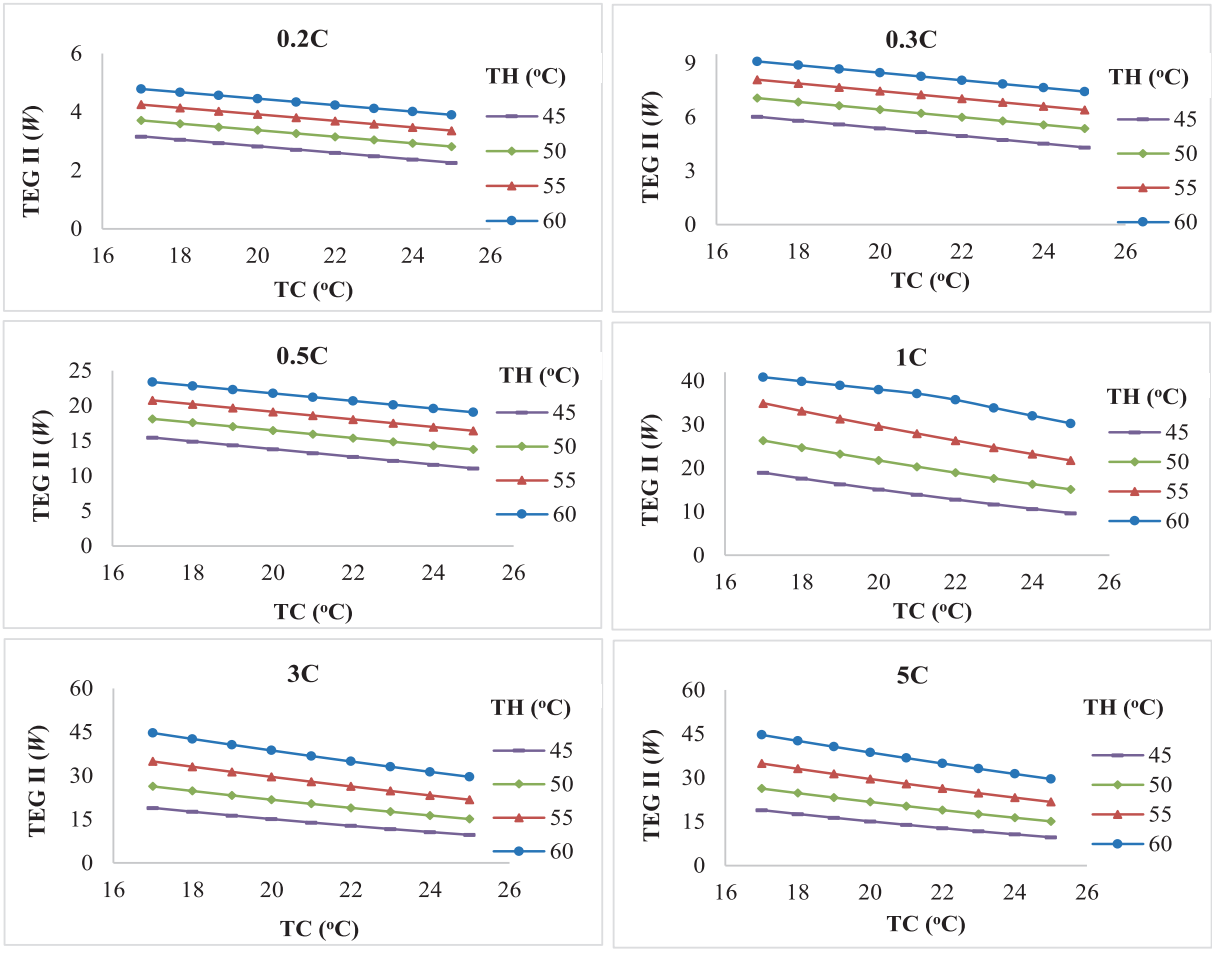

Fig. 12. Change of TEG-II output power depending on PCM temperature difference at different C-rates.

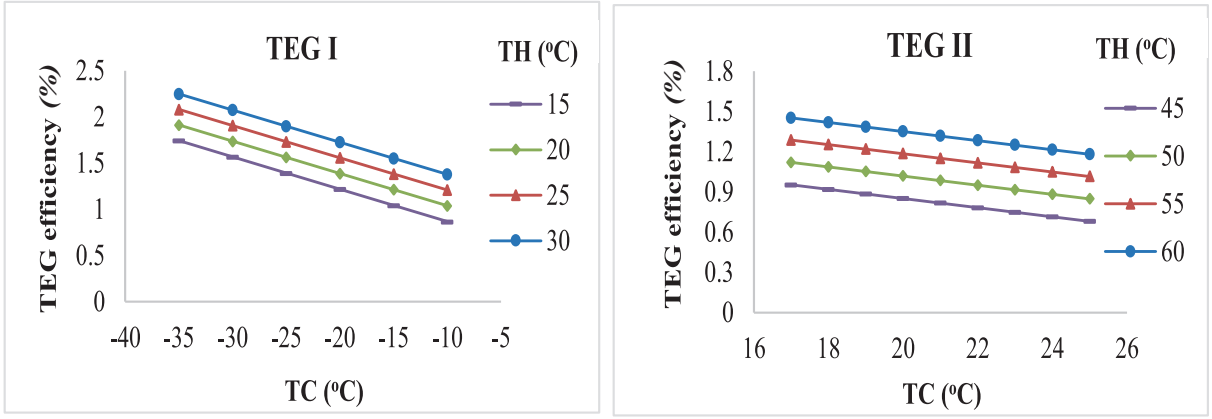

Fig. 13. Thermoelectric efficiency variation for TEG I and TEG II systems at different PCM temperatures.

modules even at similar temperature differentials. In this case, at TH = 35 °C and TC = 26 °C, the number of TEG modules required for operation in the system reached approximately 450. As observed in all graphs, the number of TEG modules increases with increasing TC while the TH temperature remains constant. The change in TEG II output power under different PCM temperatures and operating conditions is given in Fig. 12.

According to Fig. 12, it is showed the change in the electricity production of the TEG II using waste heat generated from the battery system under different C-rate and PCM temperatures. In all graphs, the hot-side temperature (TH) of the TEG varies between 35 °C and 60 °C, and the cold-side temperature (TC) varies between 17–26 °C. Under these conditions, an increase in TEG output power is observed as the temperature difference increases, while a decrease in output is observed as the cold-side temperature increases. At the 0.2C-rate, the electrical power generated is at its lowest, with a maximum output of approximately 4.6 W (TH = 35 °C, TC = 17 °C). At 1C, 3C, and 5C-rates, the increased battery waste heat potential allows for greater thermal load transfer to the TEG II. However, a design limitation of a maximum of 90 TEG modules is imposed based on the heat exchanger sizing parameters.

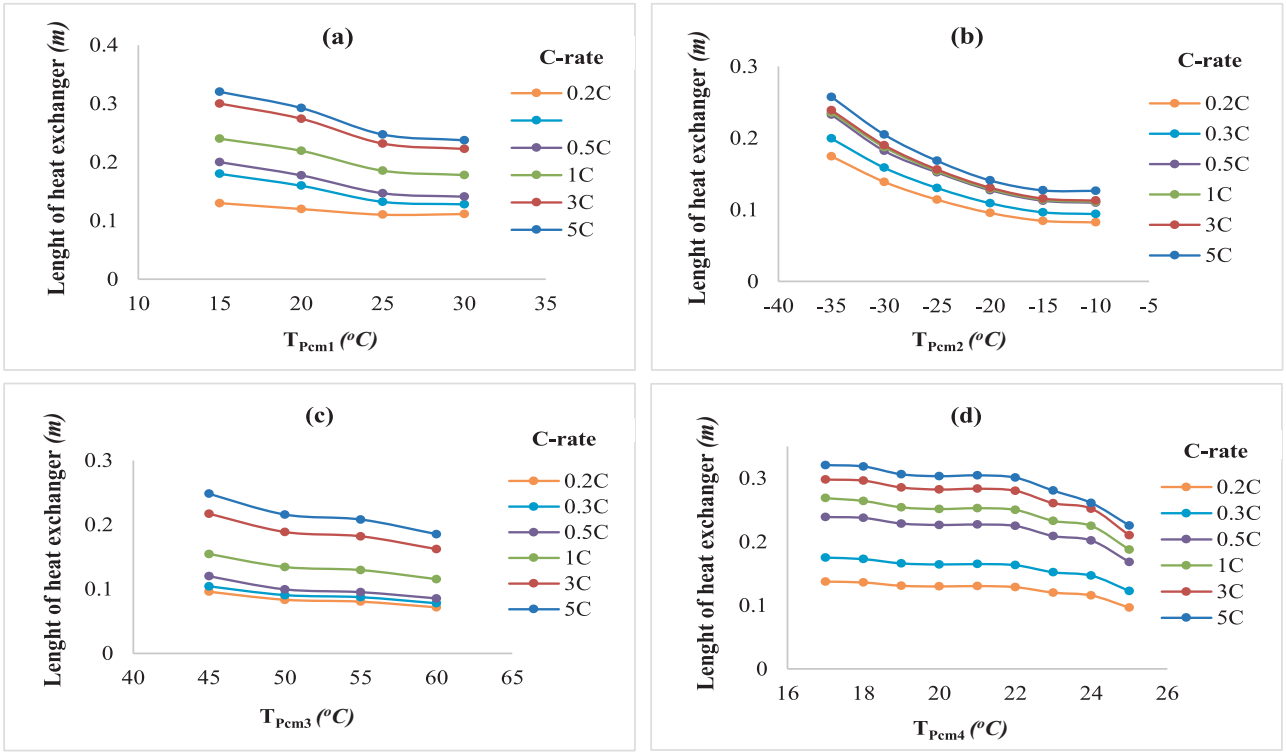

Fig. 14. Changes in heat exchanger length depending on temperature change in different PCM materials.

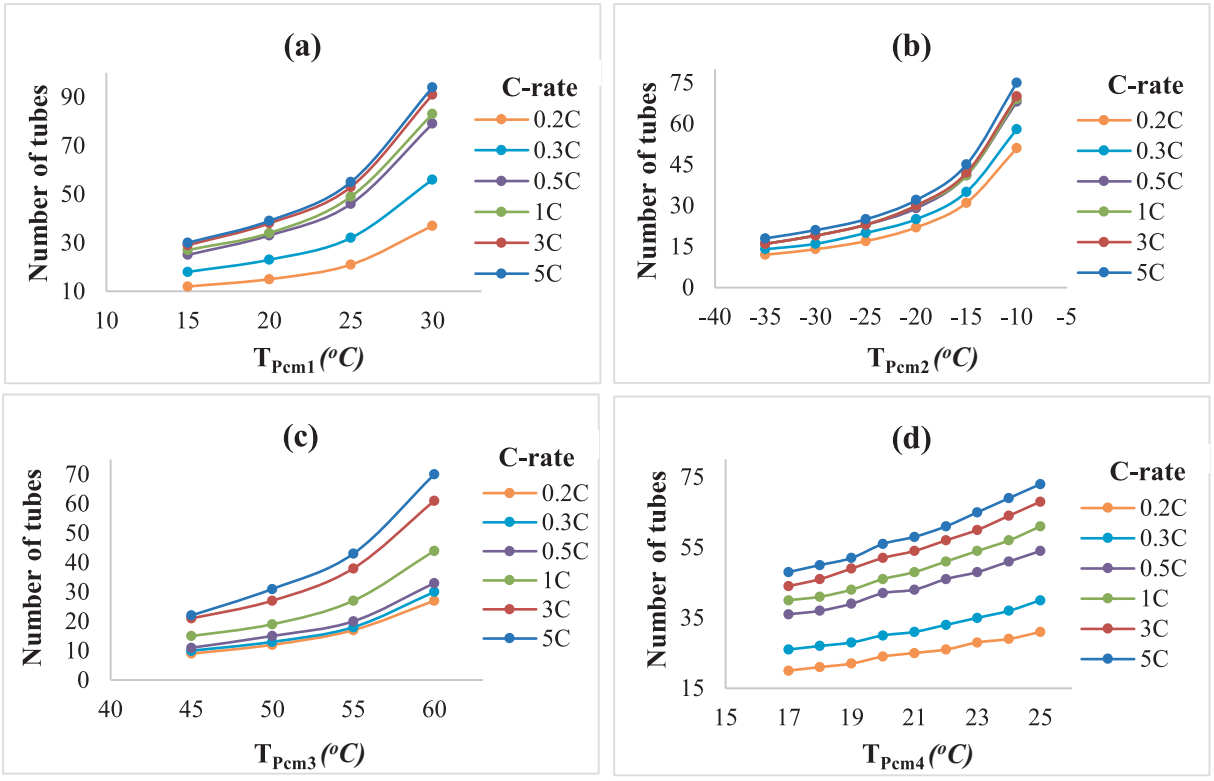

Fig. 15. Change in the total number of pipes required in the heat exchanger depending on the PCM temperature, according to the use of PCM1 (a), PCM2 (b), PCM3 (c) and PCM4 (d), according to the amount of waste heat obtained at different C-rates.

Therefore, while the 90 module limit was exceeded only in some sub-scenarios at 1C, this limit was exceeded at all PCM temperatures at 3C and 5C-rates, and the calculations were limited to 90 TEG modules. Accordingly, the maximum TEG output power was limited to 44.671 W at 3C and 5C-rates. In particular, the TEG II unit, operating at TH = 60 °C, produced the highest power values at all C rates. Consequently,

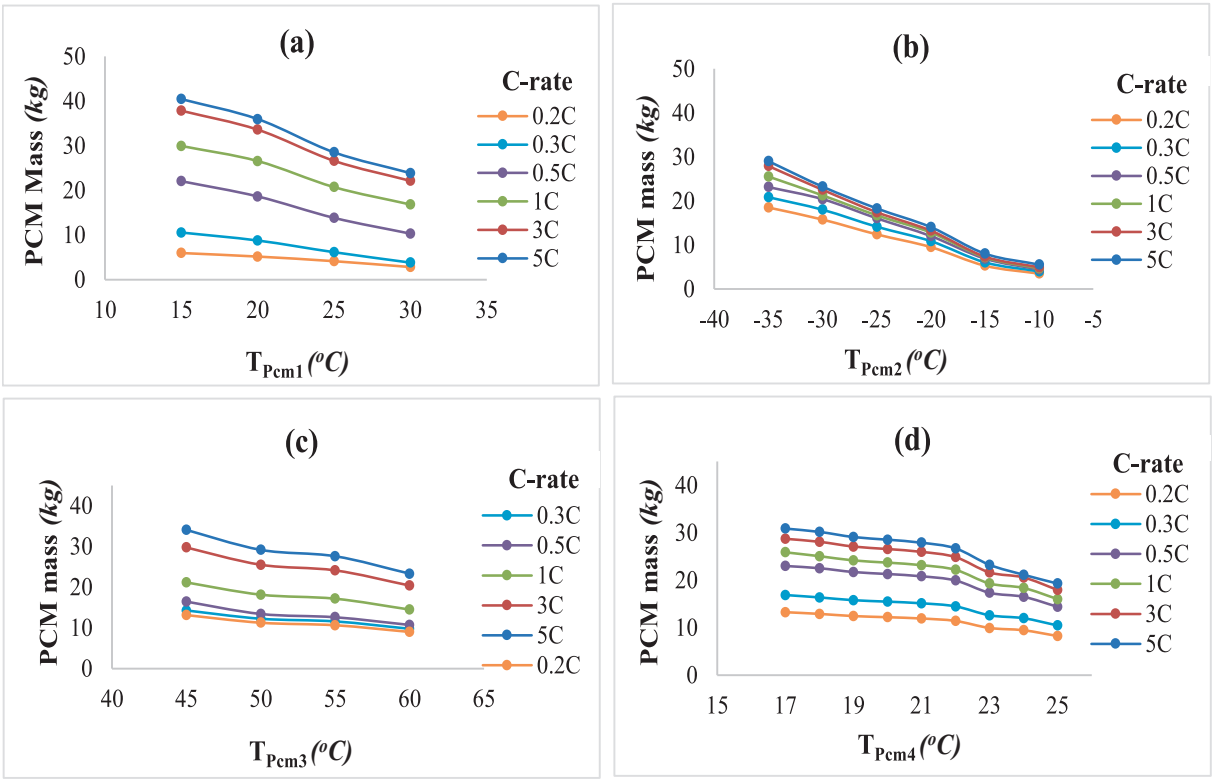

Fig. 16. Change of required PCM mass depending on different C ratios and PCM temperatures.

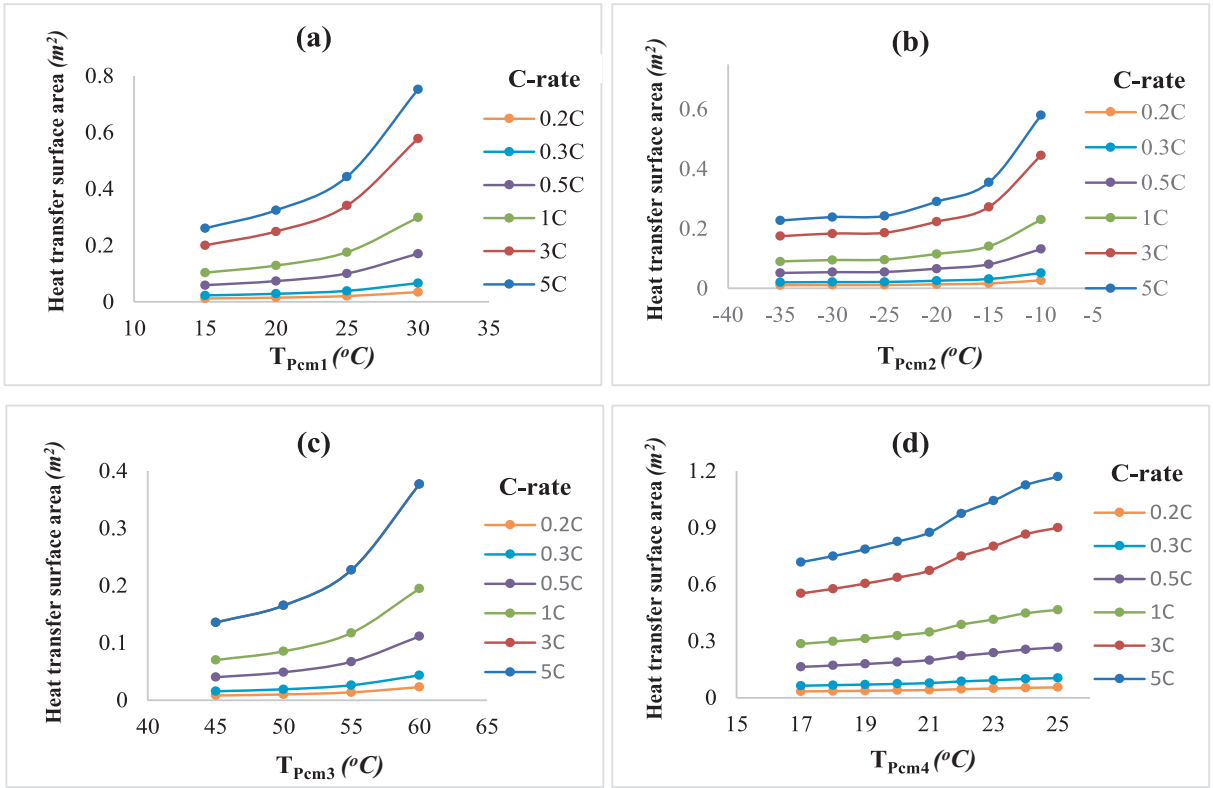

Fig. 17. Changes in heat transfer surface area depending on PCM temperature at different C-rates.

the TEG II's electricity production was determined not only by the magnitude of the temperature difference, but also by the amount of waste heat transferred from the battery system and the maximum number of TEG modules allowed in the heat exchanger design. TEG efficiencies is given in Fig. 13.

According to Fig. 12, The efficiency achieved based on the

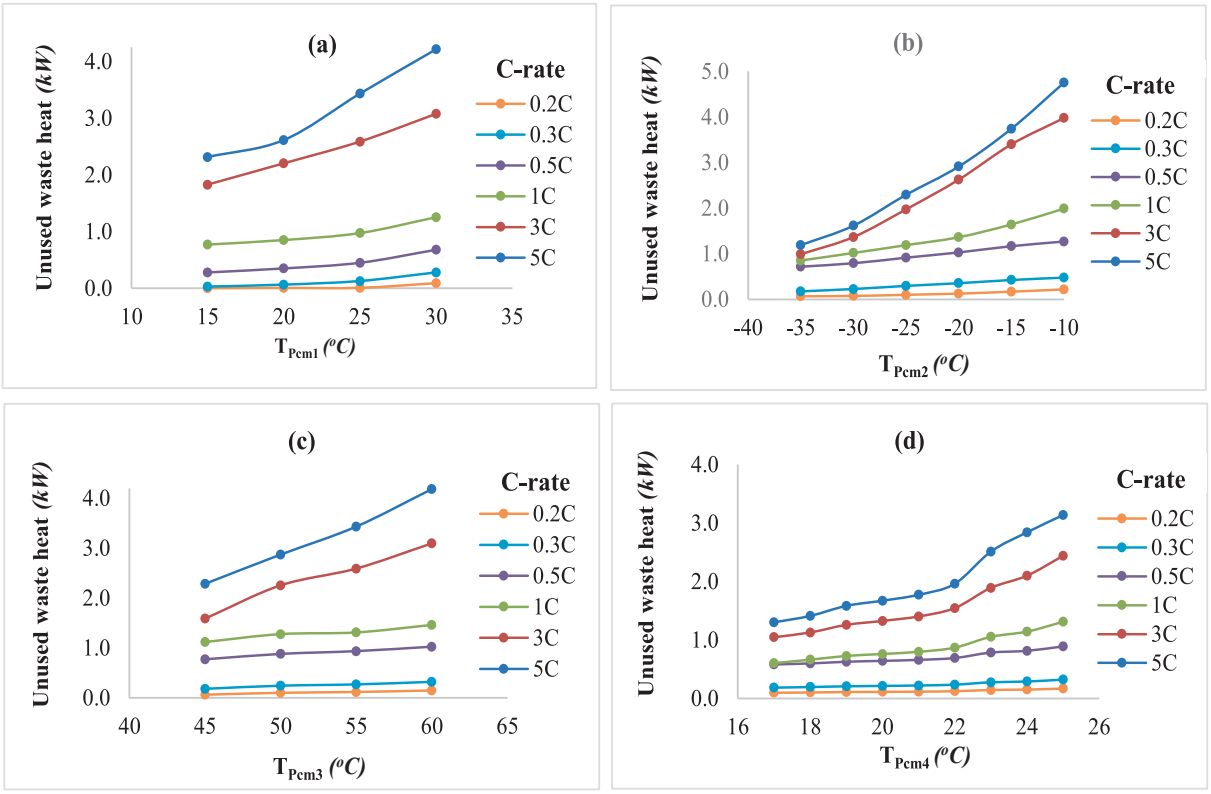

Fig. 18. Unused waste heat values depending on PCM temperature.

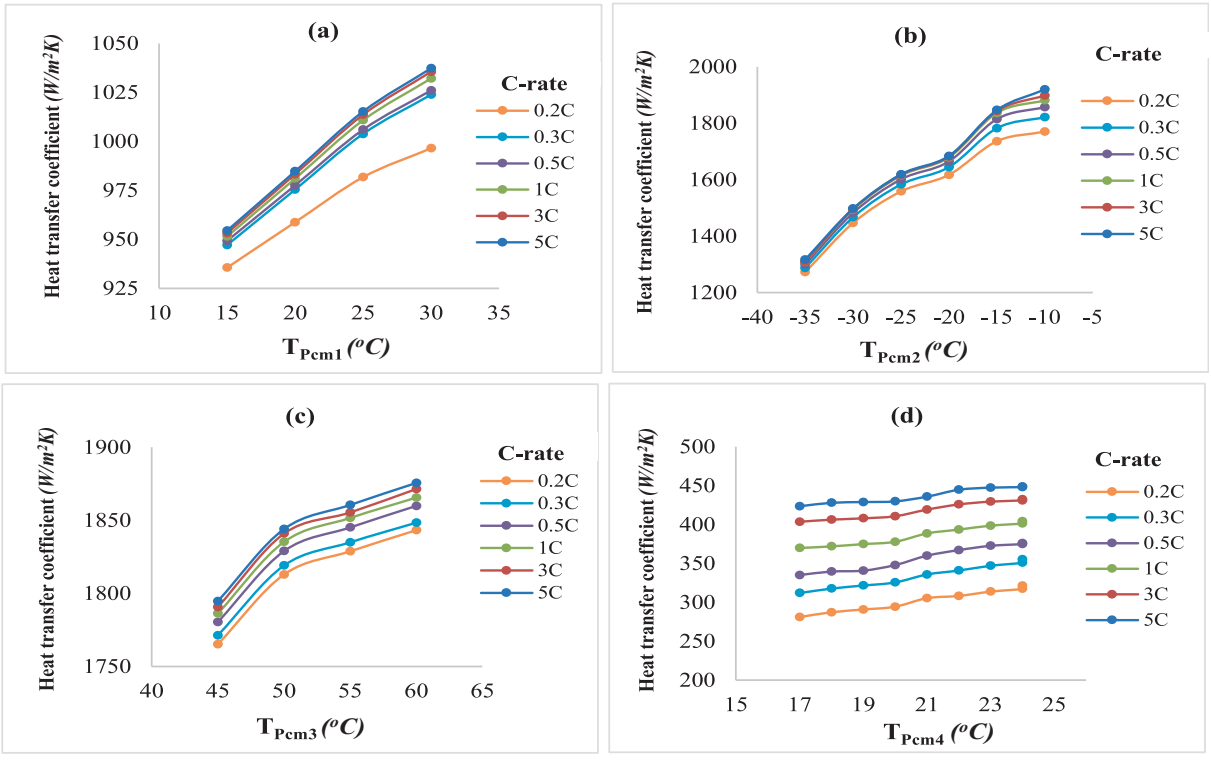

Fig. 19. Changes in heat transfer coefficient depending on PCM temperature.

temperature difference for the TEG I and TEG II systems is given. In both cases, the Kryotherm TGM-127–1.4–1.2 model was used as the TEG module. The hot surface temperature (TH) was held constant, while the cold surface temperature (TC) was varied at regular intervals. For the TEG I unit, maximum efficiency of approximately 2.3 % was achieved at TH = 30 °C and TC = −40 °C. At the reduced temperature difference

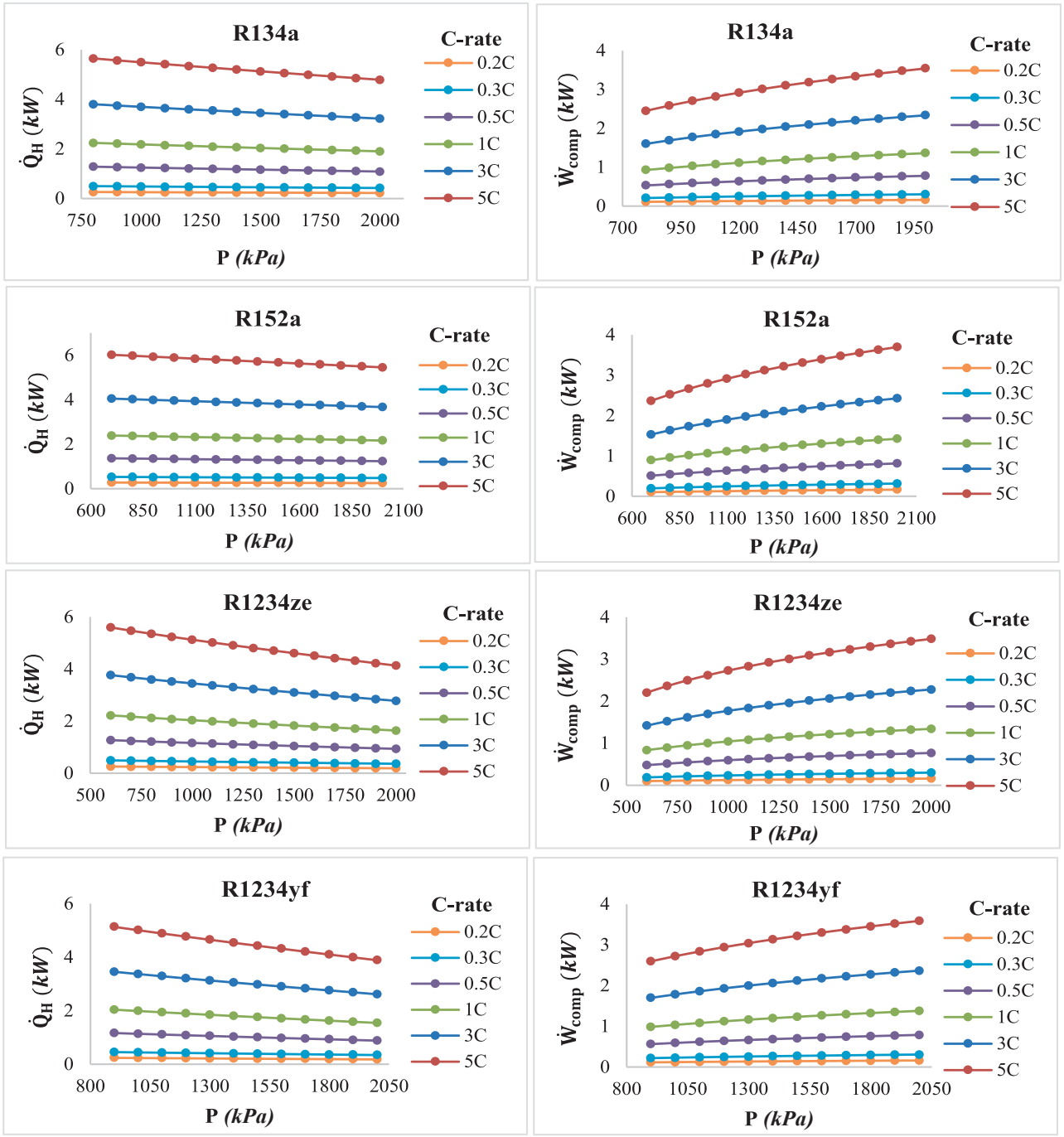

Fig. 20. Heating capacity and compressor power changes for different refrigerants.

conditions of TH = 15 °C and TC = −10 °C, efficiency was 1.2 %. For the TEG II unit, operation was carried out within a narrower temperature range (TH = 45–60 °C, TC = 17–25 °C). In this unit, the highest efficiency was calculated to be approximately 1.5 % at TH = 60 °C and TC = 17 °C, while it dropped to 0.8 % at TH = 45 °C and TC = 25 °C. In both systems, efficiency increases in direct proportion to the temperature difference. However, in the TEG II, efficiency is more limited due to the lower temperature difference values.

The heat exchanger sizing was based on the physical dimensions of the TEG modules. However, the high number of TEGs results in a larger footprint. The heat exchanger dimensions were adjusted to a maximum of 400 mm * 360 mm * 325 mm, taking into account realistic vehicle conditions. The width of the heat exchanger was kept constant at 400 mm throughout the design process, and the length and height varied for each design parameter. Based on this configuration and the total number of TEG modules required, the required length of the heat exchanger was calculated, and 90 TEGs were installed at the maximum exchanger dimensions. The surface arrangement was created accordingly. The fluids providing heat transfer to the PCMs within the heat exchanger vary depending on the operating region. PCM1 is heated by water circulating in the battery cooling circuit. In PCM2 and PCM3, heat transfer is achieved through the dual-phase refrigerant used in the vehicle heating and cooling systems. In PCM4, heat transfer is achieved through ambient air. The change in heat exchanger length depending on PCM operating temperatures at different discharge rates is given in Fig. 14.

According to Fig. 14, The changes in heat exchanger length are

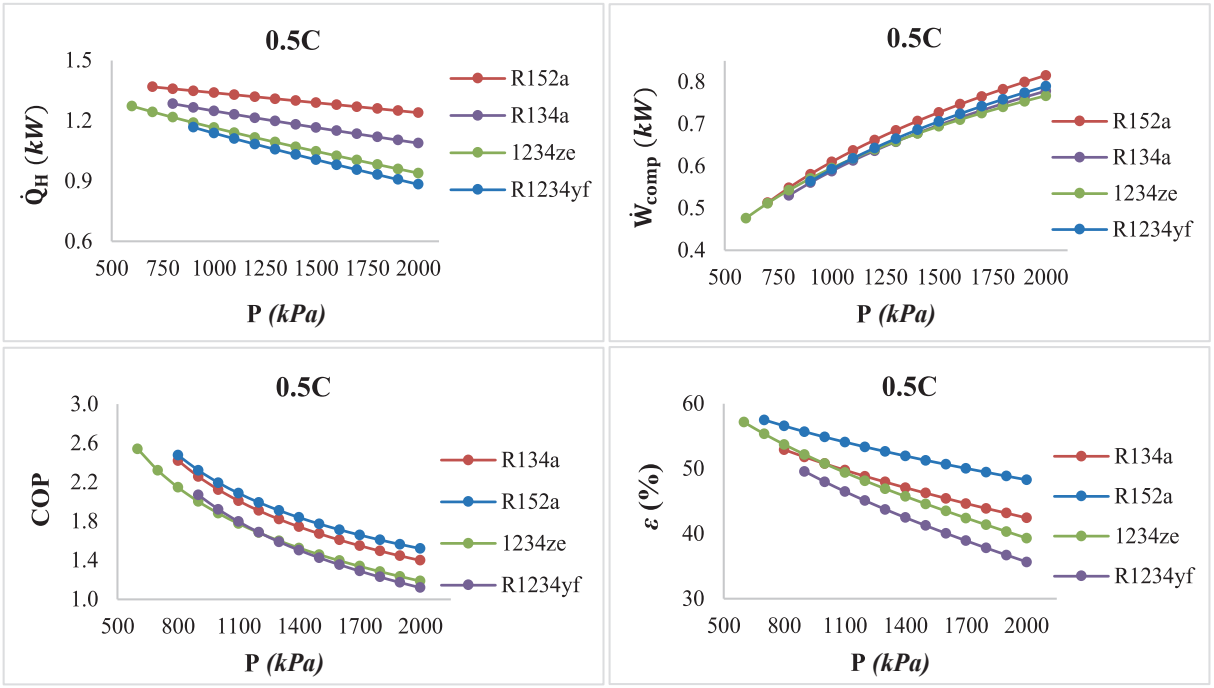

Fig. 21. Heating capacity and compressor power variation for different fluids at 0.5C-rates.

shown in different temperature ranges obtained using PCM1, PCM2, PCM3, and PCM4. All four PCMs undergo phase transition, and the system's thermal response is shaped not only by the temperature difference but also by the physical properties of the PCM, which vary with temperature. In Fig. 4a, because the phase transition characteristics of PCM1 occur within a stable range, the changes in volume and mass progress more regularly, and the exchanger length exhibits a symmetrical and continuous increase with temperature. Heights of 0.11 m to 0.32 m were obtained in Fig. 4a, and heights of 0.08 to 0.248 m were obtained in Fig. 4b. Heights of 0.09 m to 0.024 m were obtained in Fig. 4c. Heights of 0.094 to 0.324 m were obtained in Fig. 4d.

To determine the total volume of the heat exchanger, the total number of tubes corresponding to each design condition was calculated. In this context, the amount of heat that could be transferred from each tube was first calculated separately, based on the thermophysical properties of the relevant PCM and the determined temperature differences. The total amount of waste heat generated by operating the battery at different discharge rates was then taken into account, and the required number of tubes for the entire system was determined to be sufficient to accommodate this heat. In the four separate heat exchanger designs using PCM1, PCM2, PCM3, and PCM4, the energy that could be transferred per tube varied depending on the temperature conditions and heat transfer characteristics of each PCM. Therefore, the total number of tubes corresponding to the same amount of waste heat varied depending on the type of PCM used and the operating temperature. The change in the total number of tubes required in the heat exchanger based on the waste heat generated at different discharge rates and PCM temperatures is given in Fig. 15.

According to Fig. 15, The changes in the total number of tubes required for new heat exchanger designs at different PCM temperatures and battery discharge rates is given. In these analyses, the amount of waste heat obtained from the battery varies for each C ratio, with the highest waste heat occurring at a 5C-rate and the lowest at a 0.2C-rate. In Fig. 13a, due to the high heat transfer capacity of the water fluid, a limited number of tubes was sufficient at low C ratios. At 15 °C PCM temperature and a 0.2C rate, a minimum of 12 tubes were required, and at temperatures below 30 °C and 5 °C, a maximum of 94 tubes were required. In Fig. 13b, the number of tubes required ranges from 12 to 74. In Fig. 13c, the minimum number of tubes was achieved in the dual-phase fluid system, thanks to the high heat transfer capacity provided by condensation and evaporation. At 45 °C PCM temperature and 0.2C-rate, 9 pipes were required, while at 60 °C and 5 °C, 70 pipes were required. In Fig. 13d, the system required more pipes due to the low specific heat of the air fluid. The number of pipes varies between 20 and 73. As a result, the total number of pipes in the system varied depending on both the PCM temperature and the C-rate, with different fluid types meeting this requirement at different rates. The highest pipe requirement occurred in the air system, while the lowest occurred in the dual-phase fluid system. The PCM mass required in the heat exchanger design was calculated by considering the total amount of waste heat generated in the system. The effect of PCM temperature on the required PCM mass is given in Fig. 16.

According to Fig. 16,The changes in PCM mass required for the four different PCM blocks used in the heat exchanger system, depending on the C-rate and PCM temperature, is shown. In the analysis, each C-rate corresponds to a different amount of waste heat generated from the battery, and the PCM mass required to fully store this heat by the PCM was calculated. As seen in Fig. 14a, as the PCM1 temperature increases, the required PCM mass decreases at all C-rates. This trend can be explained by the need for less energy storage at higher PCM temperatures. At 5C-rate, approximately 40.44 kg of PCM is sufficient at 15 °C, and at 0.2C, approximately 2.82 kg of PCM is sufficient at 30 °C. Fig. 14b shows the maximum PCM2 requirement at 5C, 29.03 kg at 15 °C, and the minimum requirement at 0.2C, approximately 3.50 kg at 60 °C. In Fig. 14c, as the PCM3 temperature increases, the PCM mass required in the system decreases significantly. At 45 °C, approximately 23.31 kg of PCM is required at 5 °C, while at 60 °C, this value decreases to 9 kg. In Fig. 14d, at 17 °C, approximately 30.88 kg of PCM is required at 5 °C, while at 25 °C, this value decreases to 8.25 kg. This demonstrates that a larger PCM volume is required at lower temperature differences. Consequently, as the battery discharge rate increases, the waste heat entering the system also increases, directly increasing the required PCM mass. The phase change material (PCM) mass required for the heat exchanger design was calculated based on the total amount of waste heat generated in the system. Similarly, the required heat transfer surface area was determined by considering the amount of waste heat and

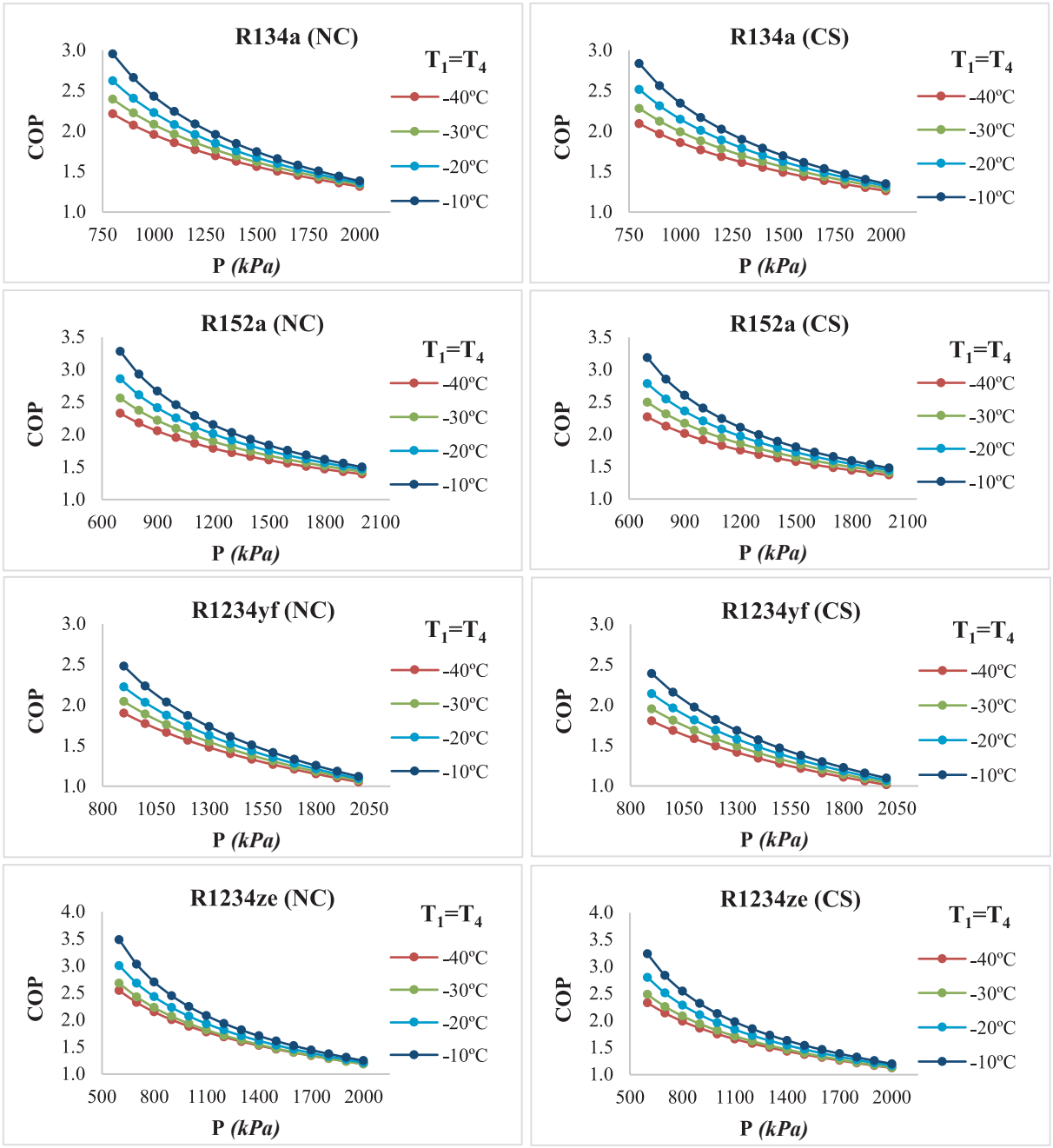

Fig. 22. COP changes of refrigerants depending on the increase in evaporator temperature.

the logarithmic mean temperature difference. Changes in heat transfer surface area is given in Fig. 17.

According to Fig. 17, The figure shows the change in the required heat transfer surface area depending on the PCM temperature for three different fluids with constant inlet temperatures. In a system operating with a fluid with a high heat transfer capacity, the temperature difference decreases as the PCM temperature increases. Consequently, the surface area required to transfer the same amount of heat tends to increase regularly and linearly. In general, heat transfer efficiency decreases as the temperature difference decreases, requiring systems with a larger surface area. The extent of these trends varies depending on the thermophysical properties of the fluids and the PCM. The amounts of unused heat are given in Fig. 18.

According to Fig. 18, the amounts of unused waste heat generated based on C ratios and PCM temperatures were evaluated in two separate exchanger systems using different fluid types (water, R134a, and air). Exchanger dimensions in all systems were limited to 0.40 m × 0.32 m × 0.25 m. The number of tubes, exchanger height, and the corresponding PCM mass allowed to be placed varied in each system. In this context, the amount of PCM that could be completely melted in each system was determined. Only the energy required to melt this mass was evaluated by the system. The total waste heat arriving at the exchanger, and any excess energy, was dissipated unused outside the system. In two different heat exchanger systems using water, R134a, and air, the evaluation was conducted with a minimum temperature difference of 5 °C for all systems. In the water system, the highest PCM mass was melted, resulting in 4.21 kW of unused waste heat. In the second system using R134a, the PCM temperature was set at −10 °C, and approximately 4.75 kW of waste heat was removed from the system. In the third system, R134a was used again, but this time, the fluid inlet temperature

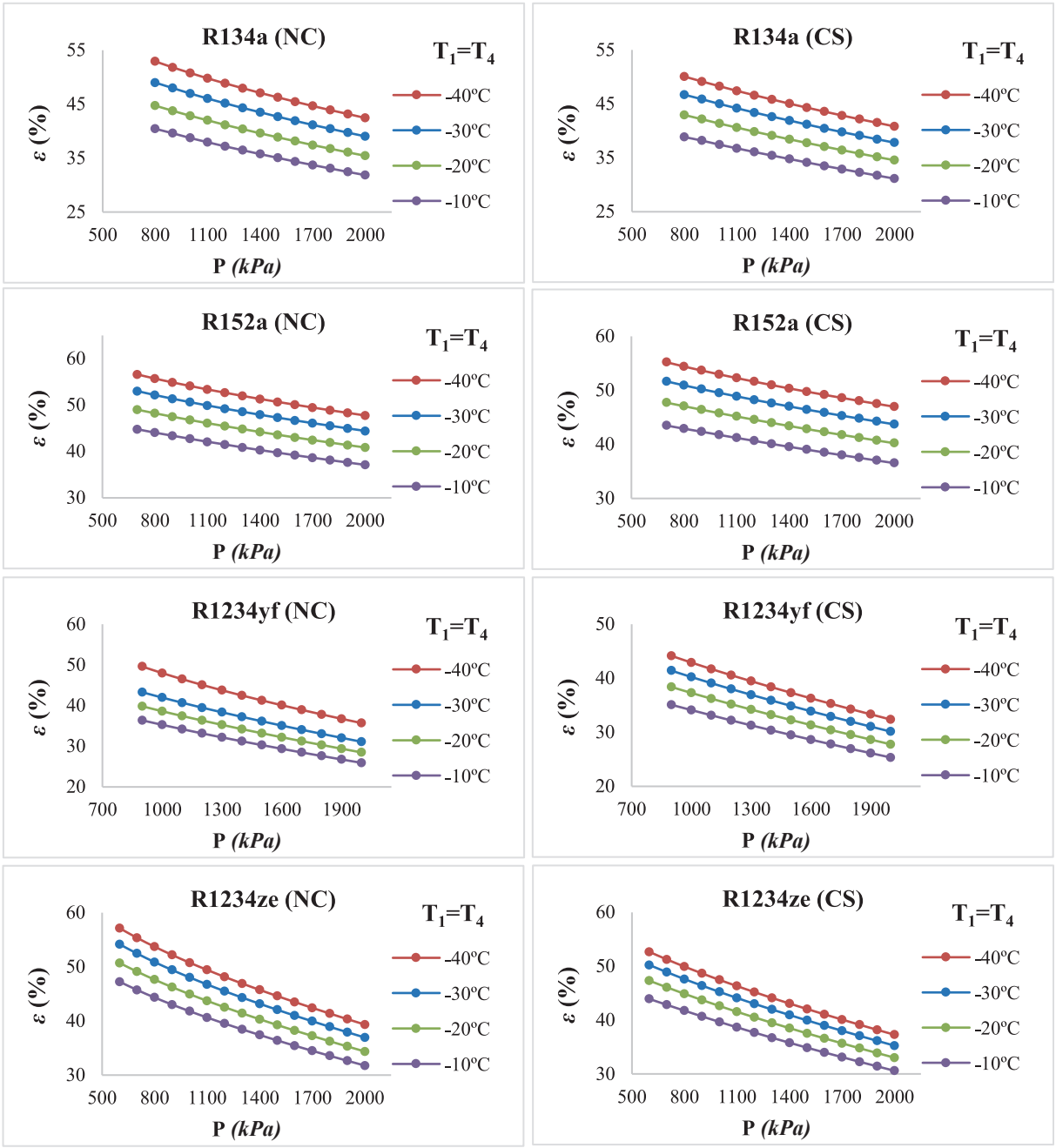

Fig. 23. Changes in second law efficiencies for R134a, R152a, R1234yf and R1234ze fluids at different evaporation temperatures.

was set at 65 °C, and 4.18 kW of unused heat was detected under a similar ΔT condition. In the final system using air, this amount was limited to 3.14 kW. These findings demonstrate that not only the fluid properties but also the temperature difference, PCM volume, and exchanger design play a decisive role in system performance. In this regards, as the temperature difference increases, the amount of waste heat that can be utilized by the system increases. Thus, the amount of heat released unused decreases. The heat transfer coefficient changes corresponding to different C-rates in four different regions, depending on the change in PCM temperature, is given in Fig. 19.

According to Fig. 19, Heat transfer coefficient values obtained at different C-rates, depending on the change in PCM temperature, are presented in four different heat exchanger zones (a-d). Each zone is classified by fluid type and represents the heat transfer surfaces in fluids operating with (a) water, (b) R134a evaporation zone, (c) R134a condensation zone, and (d) air. Since the heat load carried in the system was kept constant for a given C-rate in all zones, an increase in PCM temperature resulted in a decrease in the temperature difference between the fluid and the PCM. This required an increase in the h coefficient to maintain constant heat flux. (a), the h value was recorded as a minimum of 935 W/m^2•K (PCM1 = 15 °C, 0.2C) and a maximum of 1040 W/m^2•K (PCM1 = 30 °C, 5C). The maximum value was reached due to the increasing C ratio and decreasing temperature differences. (b), the h value varied between a minimum of 1230 W/m^2•K (PCM2 = -35 °C, 0.2C) and a maximum of 1919 W/m^2•K (PCM2 = -10 °C, 5C). (c), the maximum h value was 1875.59 W/m^2•K (PCM3 = 50 °C, 5C), and the minimum was 1765.12 W/m^2•K (PCM3 = 45 °C, 0.2C). (d), the lowest h value was determined as 281.13 W/m^2•K (PCM4 = 25 °C, 0.2C), and the highest h value was determined as 449.06 W/m^2•K (PCM4 = 17 °C, 5C). The results reveal that each region exhibits

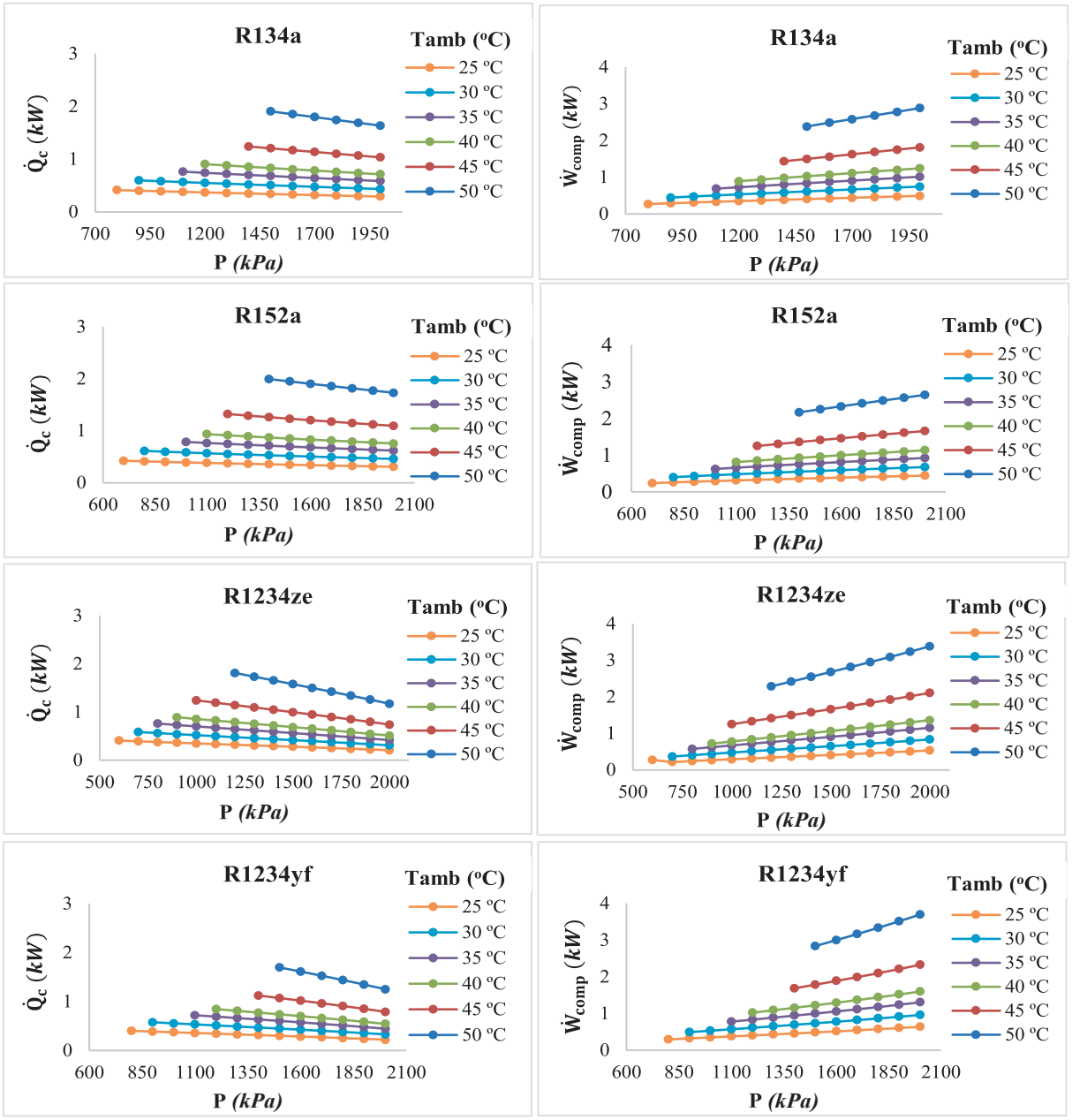

Fig. 24. Cooling capacity and compressor power changes for four different refrigerants at 0.5C discharge rate.

different heat transfer performances depending on the fluid properties, thermal load, and temperature difference.

Analyses performed for vehicle interior heating were designed to evaluate the thermodynamic effects of the refrigerants R134a, R152a, R1234yf, and R1234ze on the system. In this analysis, the evaporator temperature was maintained at −40 °C. Accordingly, the outlet pressure for each refrigerant was varied between 200 kPa and 2000 kPa. Cycle conditions were determined according to the physical properties of each refrigerant. As a result of the calculations, the resulting heating capacity, compressor power consumption, and the thermodynamic performance of each refrigerant on the cycle were analyzed in detail. The results is given in Fig. 20.

According to Fig. 20, the thermodynamic performances of the refrigerants R134a, R152a, R1234yf, and R1234ze was evaluated in different outlet pressure ranges under in-vehicle heating mode conditions with an evaporator temperature of −40 °C. In this context, the condenser pressures were determined as 750–2000 kPa for R134a, 600–2100 kPa for R152a, 800–2050 kPa for R1234yf, and 500–2000 kPa for R1234ze. As a result of the analyses, the highest heating capacity value of 6.02 kW was obtained for R152a, followed by 5.65 kW for R134a, 5.13 kW for R1234yf, and 5.00 kW for R1234ze. In terms of compressor power consumption, the lowest value was observed for R1234ze at 3.484 kW, while the highest value was observed for R152a at 3.70 kW. Heating capacity, compressor power, COP, and second-law efficiency for four different fluids at different C ratios at a 0.5C-rate and −40 °C evaporator temperature is given in Fig. 21.

According to Fig. 21, the thermodynamic performances of the refrigerants R134a, R152a, R1234yf, and R1234ze were examined in relation to outlet pressure within the scope of the analysis conducted at 0.5C-rate. According to the evaluations, the heating capacity of all −refrigerants tends to decrease with increasing outlet pressure. R152a achieved the highest heating capacity value of 1.48 kW. The maximum heating capacities for the other refrigerants were 1.32 kW for R134a, 1.26 kW for R1234ze, and 1.17 kW for R1234yf, respectively. As outlet

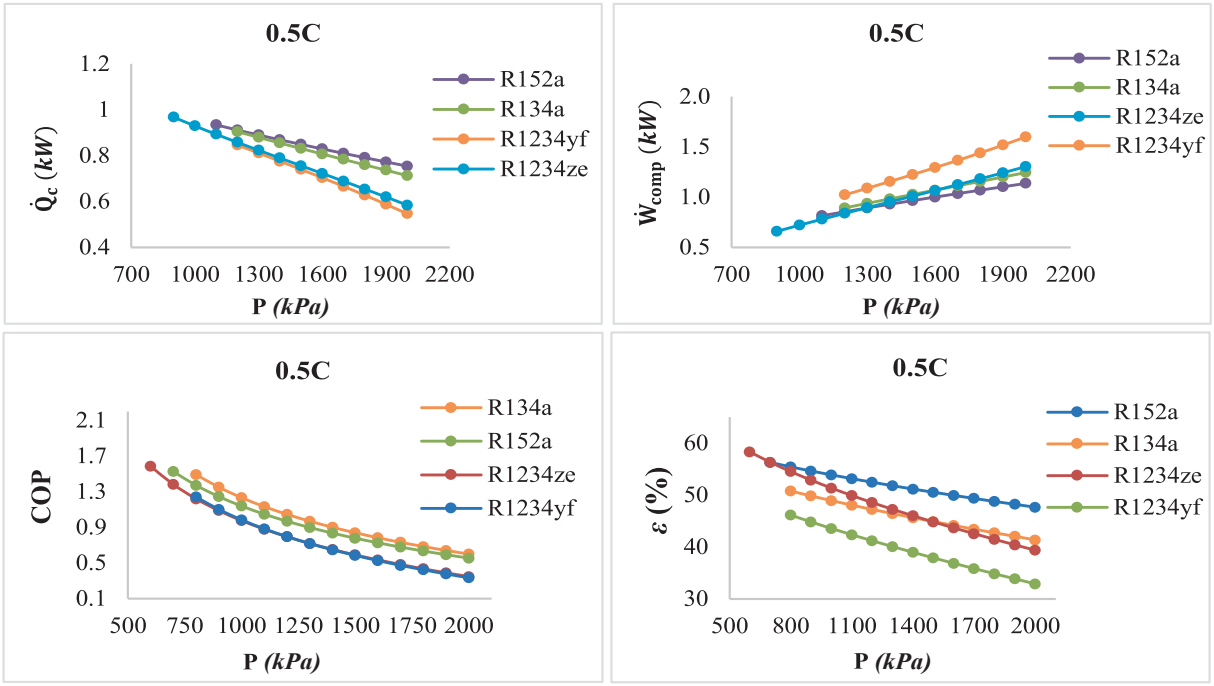

Fig. 25. Variation of cooling load, compressor power, COP and exergy efficiency.

pressure increased, compressor power increased for all refrigerants. Maximum compressor power was achieved with R152a at 0.816 kW, while maximum compressor pressures for the other refrigerants were 0.792 kW for R1234yf, 0.778 kW for R134a, and 0.767 kW for R1234ze, respectively. This indicates that R152a requires more mechanical work to achieve its high heating capacity. R1234ze, on the other hand, offers a lower-power cycle with limited energy consumption despite lower heating output. Therefore, while R152a stands out with its high heating capacity, R1234ze is considered a viable option, offering advantages in terms of energy efficiency thanks to its lower compressor power.

COP values tended to decrease with increasing condenser pressure for all refrigerants; this was due to the increased irreversibilities due to the narrowing of the temperature difference between the cycle and the ambient. Changes in COP and second-law efficiency depending on condenser pressure for four different refrigerants at a 0.5C discharge rate are given. The highest COP value of 2.549 was obtained for R1234ze at 600 kPa. The highest COP values for the other refrigerants were 2.471 for R152a, 2.421 for R134a, and 2.069 for R1234yf. In terms of second-law efficiency, the highest value of 57.14 % was obtained for R1234ze at 600 kPa. The maximum efficiencies for the other refrigerants were 56.57 % for R152a, 52.91 % for R134a and 50.59 % for R1234yf respectively. These results demonstrate that R1234ze stands out in terms of energy efficiency, providing the highest COP, while also achieving the highest second-law efficiency, making it the most advantageous refrigerant in terms of exergetic performance. Therefore, R1234ze is the most efficient refrigerant in both performance criteria. Depending on the change in evaporation temperature, the COP values obtained for four different refrigerants were evaluated comparatively with the new system (NC) and the conventional system (CS). The change in COP values is given in Fig. 22.

In analyses conducted to evaluate the effects of evaporator temperature on system performance, the COP values of four different refrigerants were examined for both NC and CS structures, with evaporator temperatures fixed at −40 °C, −30 °C, −20 °C, and −10 °C. In the NC system, the highest COP value of 3.472 was obtained with R1234ze, followed by R152a (3.276), R134a (2.953), and R1234yf (2.498). In the CS system, the highest COP values were recorded as 3.233, 3.178, 2.834, and 2.391, in the same order. Accordingly, the COP increase provided by the NC system compared to the CS system was calculated as 7.39 % for R1234ze, 3.93 % for R152a, 4.20 % for R134a, and 4.47 % for R1234yf. These results indicate that COP values increase in all systems as evaporator temperature increases, and that the NC system offers a significant improvement in energy efficiency by providing higher performance for all refrigerants. The changes in second-law efficiency with evaporator temperature for four different refrigerants in the CS and NC systems is given in Fig. 23.

According to Fig. 23, the evaporation temperatures were evaluated as −40 °C, −30 °C, −20 °C, and −10 °C. The second-law efficiencies of the refrigerants R134a, R152a, R1234yf, and R1234ze was comparatively evaluated for both NC and CS structures under different output pressures. In the NC system, a significant increase in second-law efficiency was observed with increasing evaporation temperature for all refrigerants; this is explained by the decrease in thermodynamic irreversibilities that occur with the decreasing temperature difference in the cycle. The highest second-law efficiency of 57.14 % was obtained for R1234ze, followed by R152a (56.57 %), R134a (52.91 %), and R1234yf (49.59 %). Under the same conditions, the maximum second-law efficiencies obtained in the CS system are 45.13 % for R1234yf, 55.18 % for R152a, 52.64 % for R1234ze, and 50.04 % for R134a. The efficiency increase provided by the NC system compared to the CS system is calculated as 5.73 % for R134a, 2.59 % for R152a, 9.80 % for R1234yf, and 8.54 % for R1234ze. These data bring up that the R1234ze fluid achieves the highest exergy efficiency by minimizing irreversibilities that occur during the cycle in both systems. It also demonstrates that the NC system significantly improves thermodynamic performance by providing higher second-law efficiencies than the CS system for all fluids.

For the in vehicle cooling system, the refrigeration cycle for four different refrigerants was examined at a constant evaporator inlet and outlet temperature of −40 °C, and outlet pressures were selected between 200 kPa and 2000 kPa for each, taking into account thermodynamic equilibrium conditions. Considering the physical properties of the fluids, the cycles were designed according to the second law of thermodynamics, with respect to the direction of energy flow. The resulting cooling heat loads and compressor powers was calculated accordingly. The cooling capacities, energy consumption, and performance changes

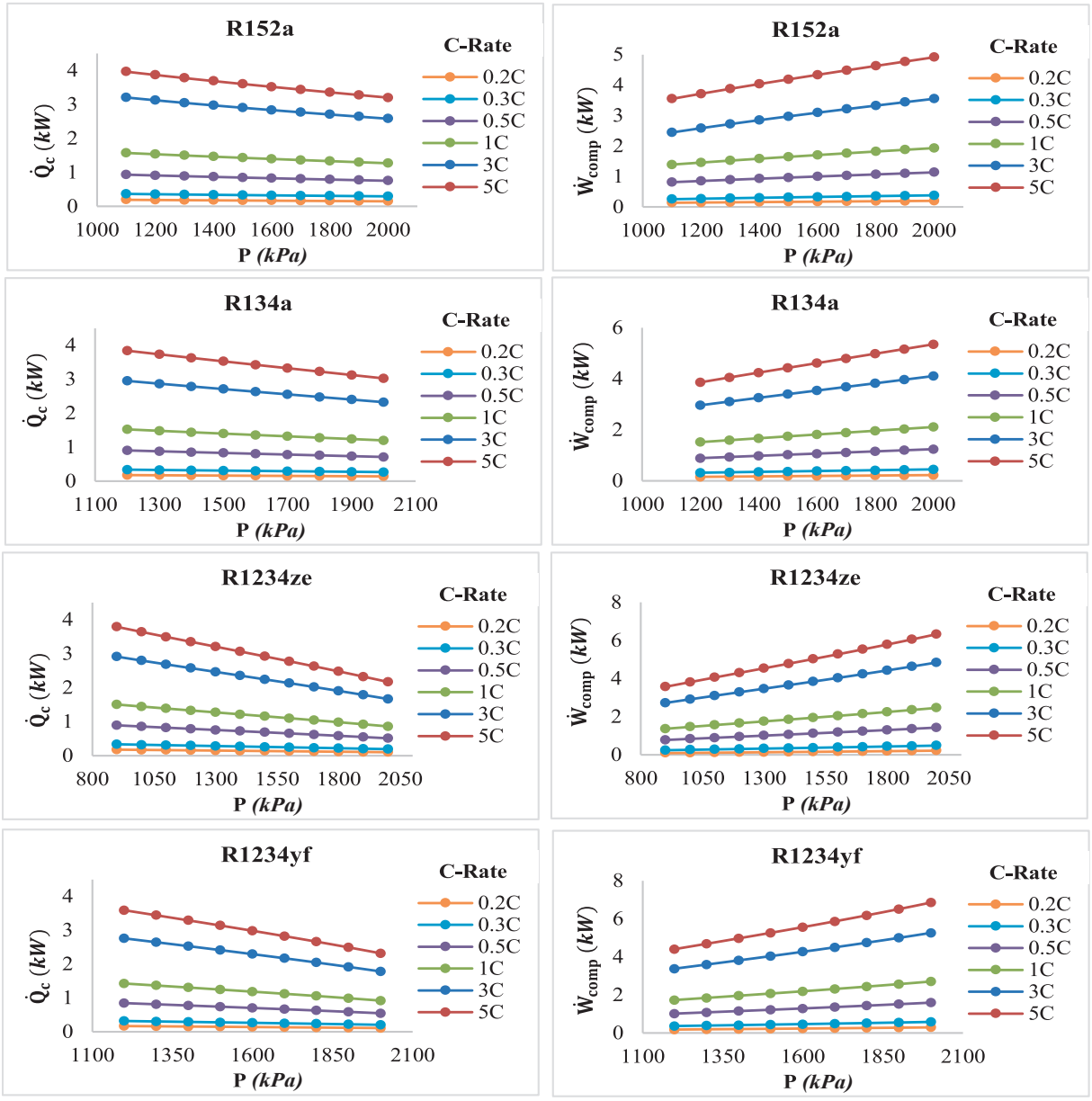

Fig. 26. Changes in cooling capacity and compressor power for four fluids.

of each refrigerant in the cycle based on these parameters is given in Fig. 24.

According to Fig. 24, The thermodynamic performance values of four different refrigerants, R134a, R152a, R1234ze, and R1234yf, are given at an evaporator temperature of −40 °C and various ambient temperatures. R152a reaches its maximum cooling capacity of 1.99 kW at 1100 kPa and 50 °C ambient temperature, while R134a reaches 1.90 kW at 1200 kPa, R1234ze reaches 1.81 kW at 1300 kPa, and R1234yf reaches 1.69 kW at 1350 kPa under the same conditions. When compressor power values are examined, at 50 °C ambient temperature, R134a reached 2,783 kW, R152a 2,643 kW, R1234ze 3,384 kW, and R1234yf 3,691 kW. At 50 °C, R152a had the highest cooling capacity and the lowest compressor power requirements. Providing more cooling with less energy compared to other fluids, R152a demonstrates its more efficient operation under these conditions. In cooling mode, the thermodynamic performance parameters of four different refrigerants were analyzed under conditions where the battery temperature was held constant at 40 °C. In this context, changes in cooling capacity, compressor power consumption, COP, and overall efficiencies depending on outlet pressure is given Fig. 25.

According to Fig. 25, the performances of four different refrigerants, R134a, R152a, R1234yf, and R1234ze were examined in the cooling mode, where the battery temperature was held constant at 40 °C. In terms of cooling capacity, a significant decrease was observed for all refrigerants with an increase in outlet pressure. This is due to the decrease in the temperature difference in the cycle due to the increase in condenser condensation temperature, thus reducing heat transfer potential. The highest cooling capacity was provided by R152a and R134a, with approximately 1.00 kW, followed by R1234ze with 0.92 kW and R1234yf with around 0.60 kW. In terms of compressor power, R1234yf reached the highest value at 1.621 kW. R1234ze 1.32 kW, R152a and R134a 1.30–1.35 kW, respectively. These results show that R1234ze has the advantage of low energy consumption, while R152a and R134a stand out with their higher cooling capacity.

COP values tend to decrease for all fluids depending on outlet pressure. The highest COP values was calculated as 1.68 for R1234ze at 600 kPa; 1.62 for R152a at 700 kPa; 1.59 for R134a at 800 kPa; and 1.39 for R1234yf at 800 kPa. In terms of exergy efficiency, R1234ze reached

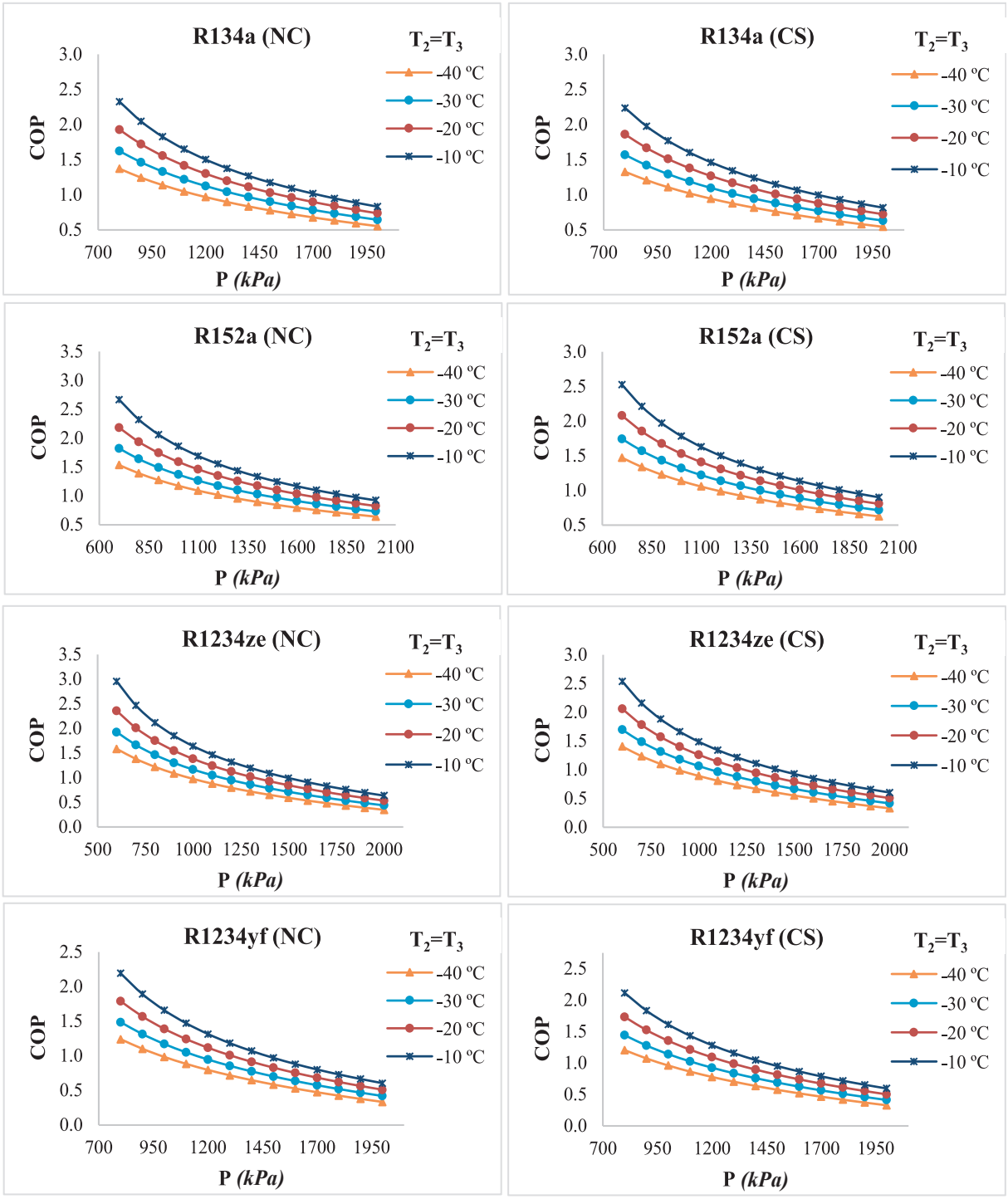

Fig. 27. Changes in COP values at different evaporator temperatures.

58.30 % at 600 kPa, R152a at 700 kPa 56.28 %, R1234yf at 800 kPa 46.12 %, and R134a at 800 kPa 51.76 %. These results clearly demonstrate the performance differences resulting from the thermophysical properties of different refrigerants used under the same cycle conditions. The thermodynamic performances of four different refrigerants operating at different C ratios in a refrigeration cycle under ambient temperature conditions of 40 °C were investigated. For each refrigerant, cooling capacity, compressor power, and energy efficiency parameters were evaluated. The results are presented in Fig. 26.

According to Fig. 26, the refrigeration cycle performances of four different refrigerants: R134a, R152a, R1234ze, and R1234yf, was evaluated at different C-rates and outlet pressures. According to the analysis results, while the cooling capacity for all refrigerants tends to decrease with increasing outlet pressure, the compressor power increases significantly. The maximum cooling capacities were 3.96 kW for R152a, 3.83 kW for R134a, 3.78 kW for R1234ze, and 3.59 kW for R1234yf. The highest values in terms of compressor power was observed for R1234yf: 6.88 kW, R1234ze: 6.33 kW, R134a: 5.31 kW, and R152a: 4.91 kW, respectively. The effect of evaporator temperatures on system performance was investigated. In this context, COP values in NC and CS systems for four different refrigerants were evaluated at different evaporation temperatures and pressure levels. Performance changes

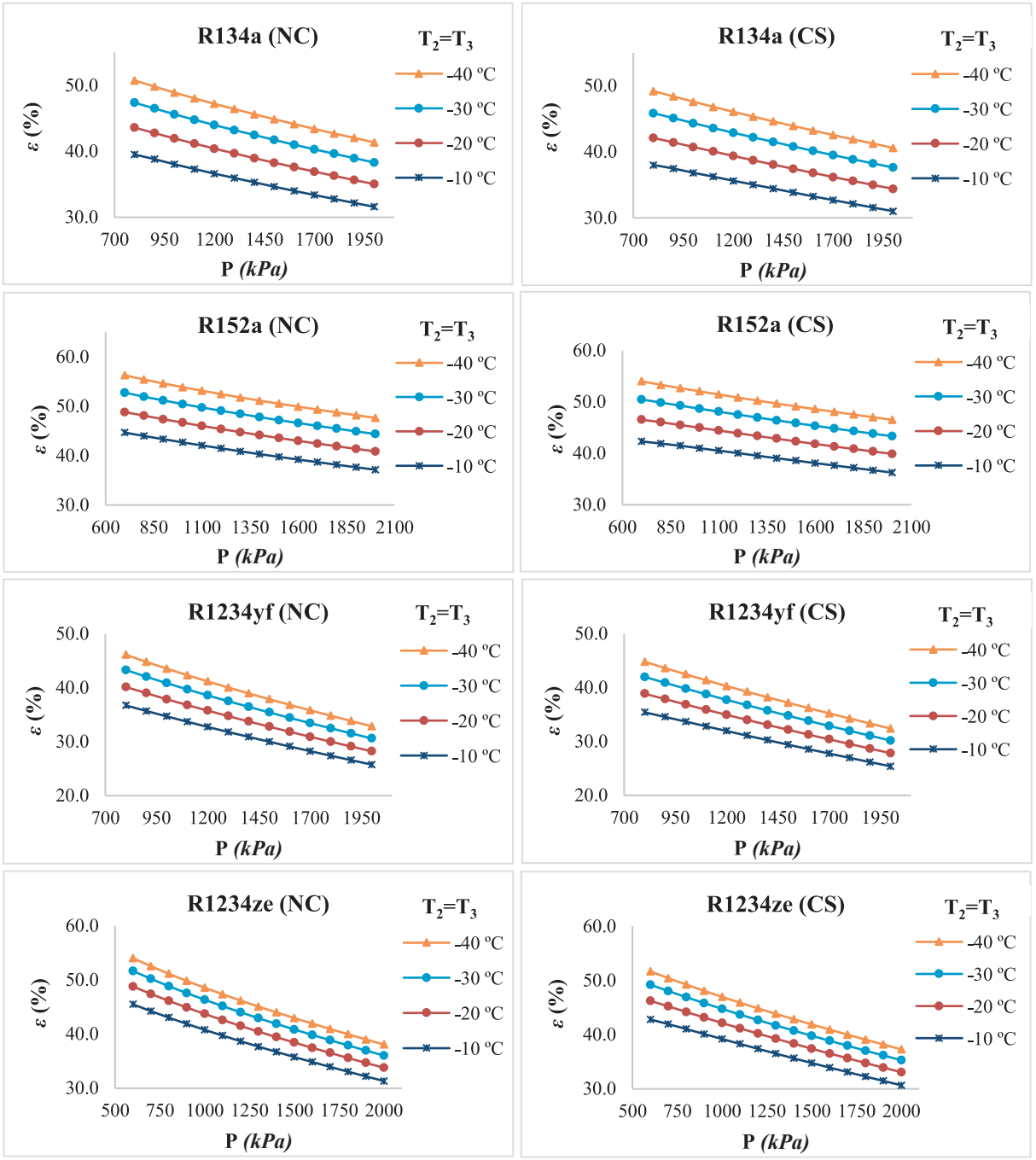

Fig. 28. Exergy efficiencies at different evaporator temperatures.

with evaporator temperature is given in Fig. 27.

According to Fig. 27, the data presented in the figure shows that, when the evaporator temperature is −10 °C, the highest COP value in the NC system is 2.69 for R1234ze. This value is followed by 2.66 for R152a, 2.44 for R134a, and 2.19 for R1234yf. In the conventional CS system, the maximum COP values for the same refrigerants are 2.54, 2.52, 2.23, and 2.11, respectively. In this context, the NC system, compared to the CS system, provides a 6.32 % increase in COP values for R1234ze, 5.57 % for R152a, 4.03 % for R134a, and 3.79 % for R1234yf. These increases demonstrate that the new concept has positive effects on thermodynamic performance and provides more efficient operation in the refrigeration cycle. As evaporator temperature increases, COP values increase in both NC and CS systems; however, this increase is greater in the NC system. This result demonstrates that the NC system operates thermodynamically more favorably, particularly at higher evaporator temperatures, and increases energy efficiency. The effect of changing evaporation temperatures on exergy efficiency is given in Fig. 28.

According to Fig. 28, the highest value in terms of second-law efficiency in the NC system was obtained as 54.03 % for R1234ze. For other fluids, this value was 56.28 % for R152a, 50.76 % for R134a, and 46.12 % for R1234yf. Under the same conditions, the maximum efficiencies of the CS system were calculated as 51.63 % for R1234ze, 54.44 % for R152a, 49.21 % for R134a, and 44.70 % for R1234yf. Accordingly, the advantage of the NC system compared to the CS system in second-law efficiency was determined as %4.64 for R1234ze, 4.22 % for R152a, 3.15 % for R134a, and 3,16 % for R1234yf. These differences show that the NC system provides a significant advantage in terms of exergy, especially when used with high potential fluids such as R1234ze. The

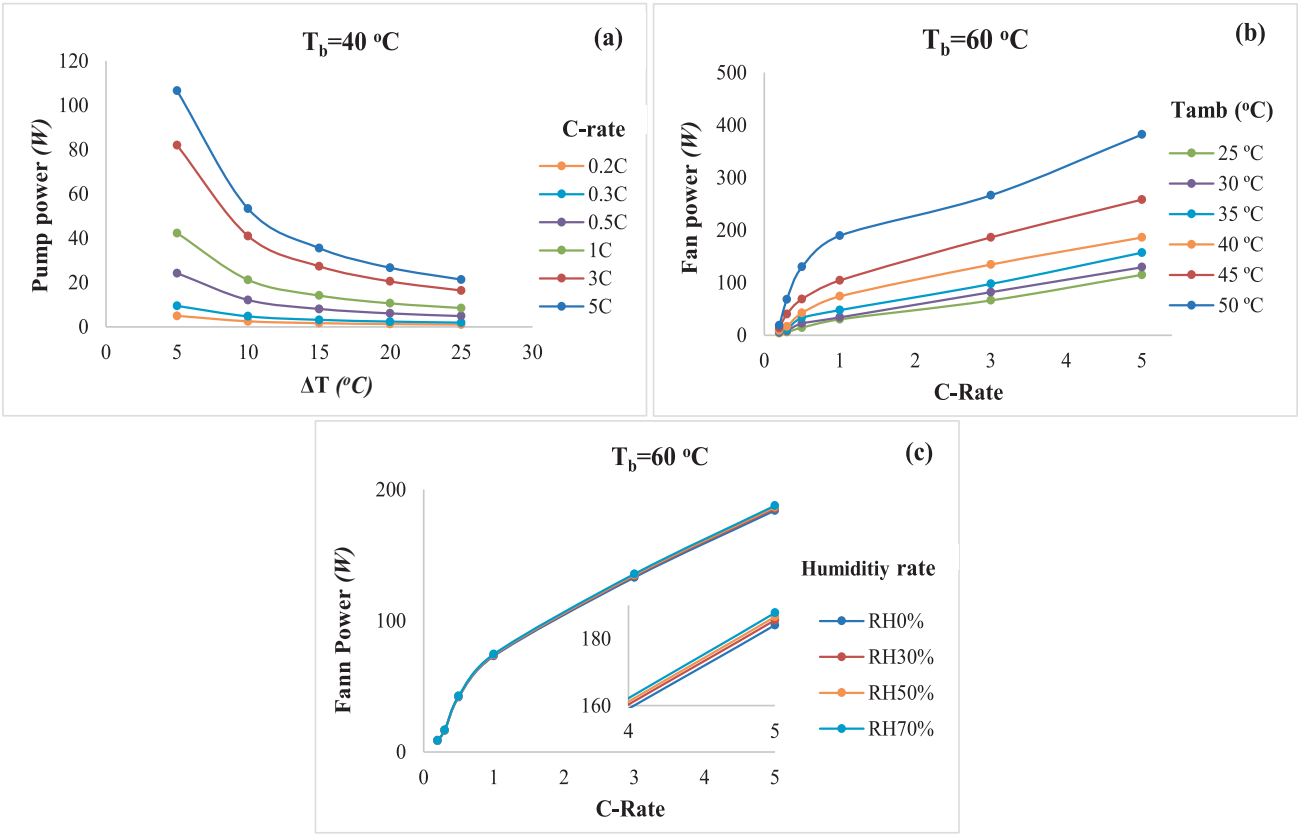

Fig. 29. (a) Pump power; (b) Fan power (dry air); (c) Fan power (according to different humidity levels).

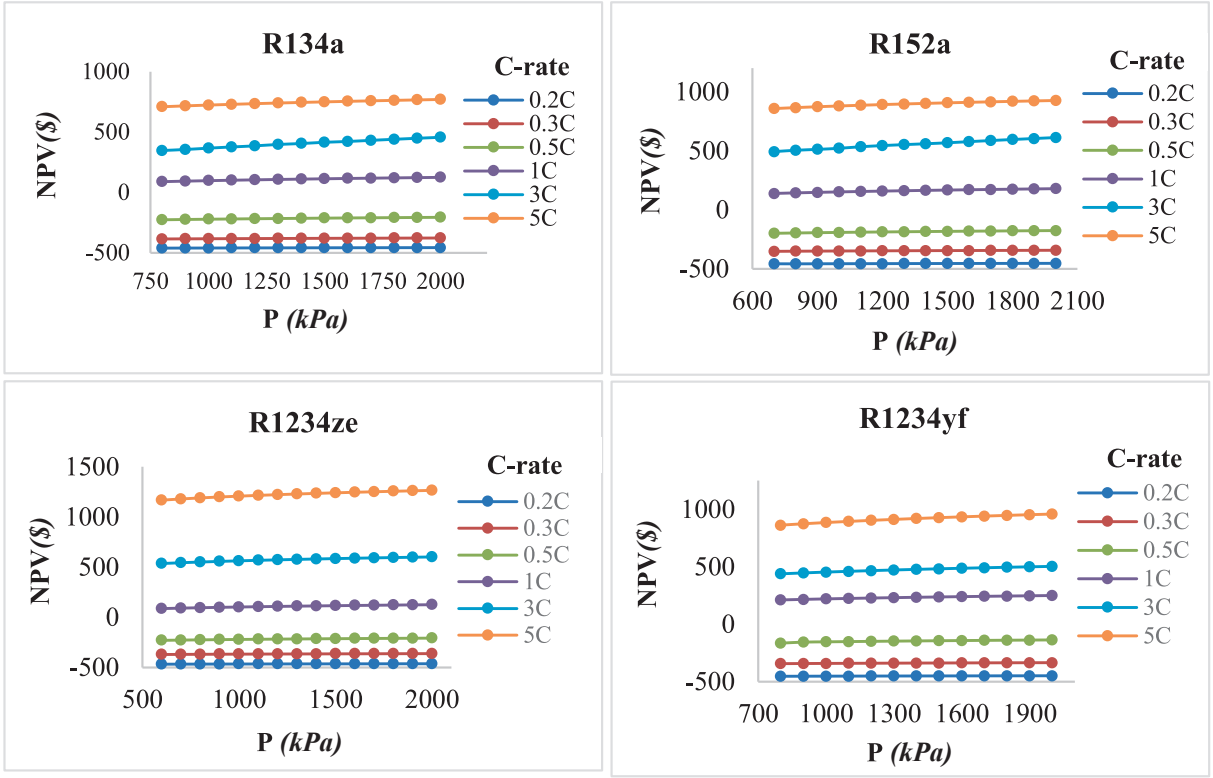

Fig. 30. NPV variations for four refrigerants at different C-rates.

Table 11
Discounted payback (DPB) periods according to different C-rates.

	DPB					
Refrigerants	0.2C	0.3C	0.5C	1C	3C	5C
R134a	8 ≤	8 ≤	8 ≤	5.64	4.63	4.02
R152a	8 ≤	8 ≤	8 ≤	5.18	4.39	3.87
R1234yf	8 ≤	8 ≤	8 ≤	5.61	4.27	3.26
R1234ze	8 ≤	8 ≤	8 ≤	5.08	4.50	3.69

Table 12
Payback benchmarks for TEG-based EV systems.

References	System	Economic assumptions	Payback	Description
[48]	Automotive TEG(Different structures)	−/Positive NPV	≈ 2–3	Structural designs shorten payback period.
[49]	EV TMS + WHR (vs. PTC)	€162-€249/ year	4.57–6.77	Annual operating savings compared to PTC heaters.
[50]	Heat pipe ATEG	613.2 kWh/ year, $85.8 /year	2.86	Advanced ATEG architecture.
[50]	Conventional ATEG	423.4 kWh/ year	1.83	Conventional structure for comparison purposes.
Present Study	EV-PCM-TEG (NC), 1C–5C	94.5–209.8 kWh/year $56.46-$1 /year	3.26–5.64	Seasonal stability with PCM, No intermediate exchanger losses, Modular TEG layout: adapt to vehicle dimensions
Present Study	EV-PCM-TEG (NC), 0.2C-0.5C	−/Yearly net gain is low	≥ 8	At lower C-rates, the payback period is longer.

Table 13
Thermodynamic properties of optimal design for R1234ze.

Point	$\dot{m}$(kg/s)	T (°C)	P (kPa)	$\dot{E}$(kW)	$\dot{E}x$(kW)
1	0.0071	−40	62.37	1.291	0.3529
2	0.0071	57.70	800	1.748	0.7420
3	0.0071	41.58	800	0.4759	0.4419
4	0.0071	−40	62.37	0.4759	0.3529
5	0.074	35	351.325	0.8468	0.0732
6	0.074	15	101.325	1.9738	0.1799
7	0.0088	47.40	800	2.1597	0.9466
8	0.0134	31.26	800	0.5878	0.5458
9	0.0355	−40	101.325	1.4285	0.2968
10	0.0355	30	101.325	1.0703	0.0474

system design includes a pump and a fan as auxiliary components. The pump directs battery cooling fluid to PCM1, while the fan cools the battery directly with air. The power consumption of these components is given in Fig. 29.

Under vehicle interior heating conditions, the pump power requirement generated during battery liquid cooling was directly related to the temperature difference between the battery and the coolant and the C-rate. Analyses conducted under constant battery temperature (Tb = 40 °C) showed that pump power decreases for all C-rates as the temperature difference increases. While pump power is approximately 110 W at a 5C discharge rate and ΔT = 5°C, it drops to 22 W when ΔT = 25 °C is reached. Similarly, pump power varies between 70–18 W at 3C and 35–9 W at 1C. It fluctuates between 20–5 W at 0.5C, 10–3 W at 0.3C, and approximately 6–2 W at 0.2C. These results indicate that operating with a low temperature difference significantly increases pump power under high current draw conditions, while the system can operate with lower energy consumption at lower C-rates. According to Fig. 28b, Fan power values calculated for different ambient temperatures (Tamb = 25–50 °C) and C ratios are given under a constant battery temperature (Tb = 60 °C). As ambient temperature increases, the air inlet temperature increases, resulting in a decrease in the temperature difference required to transport the heat load by air. Transporting the same heat load with a lower ΔT leads to an increase in mass flow rate, resulting in a significant increase in fan power. Fan power increases as both the C ratio and ambient temperature increase, reaching fan power exceeding 300 W at high ambient temperatures and high C ratios. These results demonstrate that the thermal performance of air cooling is highly dependent on ambient conditions and significantly increases system energy requirements, particularly under high-temperature conditions. According to Fig. 29 c, At 40 °C and 1 atm, under the same hydraulic/flow conditions, fan power increases only slightly with increasing relative humidity: maximum power is recorded as 184.07 W, 185.55 W, 186.55 W, and 187.74 W for RH0%, RH30%, RH50%, and RH70%, respectively; minimum power is 8.56 W, 8.63 W, 8.68 W, and 8.73 W. Based on RH0%, percentage increases in fan power are 0.81 % for RH30, 1.35 % for RH50, and approximately 2 % for RH70. Studies in the literature indicate that, under the assumption of constant heat output (CH), the COP increase with increasing relative humidity is approximately 2.4 % compared to a dry coil at 7 °C [112]. The NPV obtained depending on the operating pressure at various C-rate levels for four different refrigerants such as R134a, R152a, R1234ze and R1234yf are given in Fig. 30.

According to Fig. 30, when the minimum and maximum NPV ($) values obtained for four refrigerants at different C-rate levels are examined, it is seen that at the 0.2C-rate the lowest NPV is −$468.24 with R1234ze and the highest value is −$453.07 with R152a. At 0.3C, the NPV values vary between −$351.40 and −$342.40 for R152a, −$384.12 and −$376.19 for R134a, −$371.47 and −$362.84 for R1234ze, and −$343.53 and −$330.99 for R1234yf. At 0.5C, the minimum and maximum values for R134a are −$225.29 and −$204.94, for R152a −$198.58 to −$175.50, for R1234ze −$230.45 to −$208.29, and for R1234yf −$136.75 to −$165. At 1C, the economic performance of the system improves significantly. The values range from $90.23 to $125.48 for R134a, $139.08 to $179.44 for R152a, $86.23 to $124.97 for R1234ze, and $211.66 to $260.00 for R1234yf. At 3C, the NPV ranges from $347.98 to $457.50 for R134a, $493.51 to $642.12 for R152a, $535.69 to $601.32 for R1234ze, and $662.75 to $727.69 for R1234yf. At the highest discharge rate of 5C, the maximum NPVs were $926.42 for R152a in the pressure range of 2000 kPa. These values were $770.54 for R134a and $959.77 for R1234yf. The economic return for R1234ze fluid was calculated as $1265.25. These results show that NPV increases significantly as the C-rate increases for all fluids. This clearly demonstrates that low C-rates result in negative economic returns, while high C-rates result in positive economic returns. In this analysis, the initial investment cost was calculated as 1525.71 USD more than CS. The discounted payback periods (DPP) calculated in this study is given in Table 11.

According to Table 11, the discounted payback periods for 1C, 3C, and 5C range from 3.26 to 5.64 years. The payback periods for 0.2C, 0.3C and 0.5C are greater than 8 years (≥8). This finding is consistent with the 8-year NPV evaluation period: NPV ≥ 0 for configurations with a DPB < 8, and NPV < 0 for those with a DPB ≥ 8. As the C-rate increases, recoverable electricity production and annual net revenue increase, while the DPB decreases accordingly. At low C-rates (0.2C-0.5C), the net revenue is insufficient, resulting in negative NPV and DPB values of ≥ 8 years. These trends are regular and consistent across the pressure range and for all fluids. A comparison table is provided in Table 12.

Our evaluation framework is based on LCC/NPV and is consistent with reference studies. In [48], ATEG designs focusing on electricity production alone report positive NPV and ≈2–3 year payback. Similarly,

Table 14
Energy and Exergy analysis results for R1234ze.

Component	$\dot{Q}$(kW)	$\dot{W}$(kW)	$\dot{E}x_Q$(kW)	$\dot{E}x_W$(kW)	$\dot{E}x_d$(kW)	η (%)	ε (%)	COP
Evaporator	0.8156	–	0.2448	–	0.2448	–	59.44	
Compressor	–	0.477	0.348	0.477	0.260	89.26	42.61	
Condenser	1.272	–	–	–	0.6234	–	69.06	
Pump	0.0012	0.00484	0.00317	0.00484	0.00007	70	77.07	
Fann	0.0014	0.0422	0.0002	0.0422	0.041	55	10.99	
Overall system							57.14	2.42

while the TEG solutions in [49] and [50] focus mainly on electricity generation, our NC design provides thermal benefits + electrical gains by integrating a PCM-assisted heat pump with a TEG and eliminates intermediate heat exchanger losses. Our tabular results show that NPV $\geq$ 0 and DPB of 3.26–5.64 years are achieved in the 1C–5C scenarios. This demonstrates that we offer a competitive (in some cases shorter) payback compared to the 4.57–6.77 years reported for EV-TMS + WHR in [49]. In another study, the payback period for heat pipe ATEG was 2.86 years and for conventional ATEG it was 1.83 years. The modular TEG layout provides adaptability and scalability to vehicle sizes, while the PCM increases seasonal stability. As the C-rate increases, the recoverable electricity production and annual net cash flow increase. As a result, the discounted payback period shortens (at lower C-rates, the payback is longer because the net gain is limited). This is primarily due to the increased waste heat generated from the battery as the C-rate increases, resulting in the PCM-TEG system operating with more recoverable energy. Considering maximum COP, exergy efficiency, and NPV values, the optimum design point was obtained at a compressor outlet pressure of 600 kPa. In this study, the optimal system parameters for R1234ZE refrigerant were determined under these conditions. The thermodynamic properties of the optimum system is given in Table 13, and the energy and exergy analysis results are presented in Table 14.

According to the energy and exergy analysis of the R1234ZE refrigerant, the highest exergy destruction in the system occurred in the compressor with 0.260 kW, and this component achieved the highest efficiency of 89.26 %. The evaporator determined the heat removal capacity of the system with 0.8156 kW of heat transfer and 0.2448 kW of exergy destruction, while the condenser generated 0.6234 kW of exergy destruction for 1.272 kW of heat. The pump and fan, among the auxiliary elements, operated with 70 % and 55 % exergy efficiency, respectively, and the fan's exergy destruction was calculated as 0.041 kW. The overall system COP was 2.42, and the exergy efficiency was 57.14 %.

10. Conclusion

In this study, two different systems integrating PCM and TEG technologies were designed to recover battery-generated waste heat in electric vehicles. Their energy, exergy, and economic performances under seasonal conditions were investigated in detail. In the winter, waste heat generated through a water-based thermal management system, in which the battery was kept at a constant temperature of 40 °C, was transferred to TEG1. Condenser waste heat from the cooling cycle was also utilized through TEG2. In this context, at 5C-rate'de, TEG1 produced 102 W with R134a, 97.2 W with R152a, 100.5 W with R1234yf, and 98.1 W with R1234ze. Under the same conditions, TEG2 produced 47.2 W, 45.3 W, 46.1 W, and 45.8 W, respectively. Thus, in winter mode, total TEG production reached 149.2 W for R134a, 142.5 W for R152a, 146.6 W for R1234yf, and 143.9 W for R1234ze.

In summer conditions, the battery was cooled by ambient air, its temperature rose to 60 °C, and the waste heat from this high temperature was utilized solely through TEG2. In this case, TEG2 generated 38.9 W of electricity with R134a, 36.5 W with R152a, 37.6 W with R1234yf, and 36.9 W with R1234ze. When the system performance was examined, in the heating system, under conditions of evaporator temperature being −10 °C, the highest COP value was 3.472 with R1234ze. On the other hand, for 5C-rate,the highest compressor power consumption was 3.718 kW with R152a, and the lowest compressor power was 2.205 kW with R1234ze. In the heating system, the highest 57.14 % exergy efficiency was obtained with R1234ze, and the lowest 31.84 % with R134a. In the cooling system, for the 5C-rate, the highest COP value was 2.95 with R1234ze, and the lowest COP value was 0.89 with R1234yf. The highest exergy efficiency was obtained with R1234ze, with 58.30 %, and the lowest exergy efficiency was obtained with R1234yf, with 25.76 %. The highest compressor power values were observed for R1234yf, 6.88 kW, and the lowest for R152a, 4.91 kW. NPV analyses similarly revealed positive economic results for all refrigerants at high C ratios. At 5C, the maximum NPV reached $959.77 for R1234yf, with values of $770.51 for R134a, $962.42 for R152a, and $1265.25 for R1234ze. The findings demonstrate that such integrated recovery systems are feasible for electric vehicles in terms of both energy efficiency and economic sustainability. The discounted payback periods calculated in this study are 3.26–5.64 year.

CRediT authorship contribution statement

Ahmet Mavi: Conceptualization, Writing – review & editing, Investigation, Methodoloy. **Oguz Arslan:** Writing – review & editing, Supervision, Investigation, Methodoloy, Conceptualization.

Declaration of competing interest

The authors declare that they have no known competing financial interests or personal relationships that could have appeared to influence the work reported in this paper.

Data availability

No data was used for the research described in the article.

References

[1] Y. Zhu, E.F. Choma, K. Wang, H. Wang, Electric vehicle adoption delivers public health and environmental benefits, Eco-Environ. Health 2 (4) (2023) 193–194.
[2] M. Ehsani, Y. Gao, S.E. Gay, A. Emad, Modern electric, hybrid electric and fuel cell vehicles, 3rd ed., CRC Press, Taylor & Francis Group, Boca Raton, FL, USA, 2018.
[3] X. Zeng, M. Li, D. Abd El-Hady, W. Alshitari, A.S. Al-Bogami, J. Lu, K. Amine, Commercialization of lithium battery technologies for electric vehicles, Adv. Energy Mater. 9 (27) (2019) 1900161.
[4] Y. Chen, et al., A review of lithium-ion battery safety concerns: the issues, strategies, and testing standards, J. Energy Chem. 59 (2021) 83–99.
[5] M. Li, J. Lu, Z. Chen, K. Amine, 30 Years of lithium-ion batteries, Adv. Mater. 30 (33) (2018) 1800561.
[6] A.A. Pesaran, Battery thermal models for hybrid vehicle simulations, J. Power Sources 110 (2) (2002) 377–382.
[7] K.S. Garud, L.D. Tai, S.-G. Hwang, N.-H. Nguyen, M.-Y. Lee, A review of advanced cooling strategies for battery thermal management systems in electric vehicles, Symmetry 15 (7) (2023) 1322.
[8] M. Bandhauer, S. Garimella, T.F. Fuller, A critical review of thermal issues in lithium-ion batteries, J. Electrochem. Soc. 158 (3) (2011) R1–R25.
[9] J. Bao, Y. Mao, Y. Zhang, et al., Critical review of temperature prediction for lithium-ion batteries in electric vehicles, Batteries 10 (12) (2024) 421.
[10] S. Yang, et al., A review of lithium-ion battery thermal management system strategies and the evaluate criteria, Int. J. Electrochem. Sci. 14 (2019) 6077–6107.

[11] H. Togun, et al., A comprehensive review of battery thermal management systems for electric vehicles: enhancing performance, sustainability, and future trends, Int. J. Hydrogen Energy 97 (Jan. 2025) 1077–1107.
[12] M.A. Hannan, M.S. Hossain Lipu, A. Hussain, A. Mohamed, A review of lithium-ion battery state of charge estimation and management system in electric vehicle applications: challenges and recommendations, Renew. Sustain. Energy Rev. 78 (2017) 834–854.
[13] A.J. Piggott, J.S. Allen, A.A. Pesaran, High-heat transfer lithium-ion batteries: a new era in battery thermal management, Appl. Therm. Eng. 272 (2025) 126347.
[14] I. Park, C. Kim, H. Lee, C.-L. Myung, K. Min, Comprehensive analysis of battery thermal management and energy consumption in an electric vehicle: impact of driving modes and ambient temperatures, Int. J. Automot. Technol. 26 (2025) 621–636.
[15] N. Napa, M.K. Agrawal, B. Tamma, Development of electro-thermal model for prismatic lithium-ion cell subjected to electric vehicle drive cycle using converging fluid channel, Int. J. Therm. Sci. 199 (2024) 108936.
[16] A. Wang, J. Zhou, Q. Li, F. Jia, D. Hu, X. Yin, F. Cao, Performance evaluation of steady-state and dynamic response for innovative configurations of EV cabin and battery coupled thermal management based on transcritical CO2 cycle, Energy (2025) 137984.
[17] M. Kılıç, M.Ö. Korukçu, The effect of energy management in heating-cooling systems of electric vehicles on charging and range, Appl. Sci. 14 (15) (2024) 6406.
[18] A. Nandy, Y. Houl, W. Zhao, N.A. D'Souza, Thermal heat transfer and energy modeling through incorporation of phase change materials (PCMs) into polyurethane foam, Renew. Sustain. Energy Rev. 182 (2023) 113410.
[19] L. He, H. Jing, Y. Zhang, P. Li, Z. Gu, et al., Performance research of integrated thermal management system for battery electric vehicles with motor waste heat recovery, J. Energy Storage 84 (2024) 110893.
[20] L. He, B. Tong, L. Wu, Y. Zhang, Y. Feng, L. Tan, Performance investigation of integrated thermal management system for electric vehicle with waste heat recovery of electric drive system, J. Storage Mater. 102 (2024) 114075.
[21] D.A. Dolla, M.G. Fetene, Investigations of phase change materials in battery thermal management systems for electric vehicles: a review, Mater. Res. Express 11 (1) (2024) 012002.
[22] F.S. Hwang, T. Confrey, C. Reidy, D. Picovici, D. Callaghan, D. Culliton, C. Nolan, Review of battery thermal management systems in electric vehicles, Renew. Sustain. Energy Rev. 192 (2024) 114171.
[23] K. Song, A.N.M. Tanvir, M.O. Bappy, Y. Zhang, New directions for thermoelectrics: a roadmap from high-throughput materials discovery to advanced device manufacturing, Small Sci. 4 (2024) 2300359.
[24] P. Chelladorai, P. Atekov, N.K. Balakrishnan, A. Kashyap, P. Chakravarty, G. Naresh, Computational and experimental evaluation of thermoelectric generator for waste heat recovery in internal combustion engine applications, SAE Tech. Paper no (2024) 2024–01-5076.
[25] X. Zhou, A.M. Abed, R. Chaturvedi, B.S. Abdullaeva, A. Shawabkeh, Y. Fouad, F. Riaz, A novel thermal management system for a cylindrical battery based on tubular thermoelectric generator, Case Stud. Therm. Eng. 59 (2024) 104585.
[26] Z. Shi, G. Wang, C. Liu, Q. Lv, B. Gong, Y. Zhang, Y. Yan, Optimizing the transient performance of thermoelectric generator with PCM by Taguchi method, Energies 16 (2) (2023) 805.
[27] A. Wazeer, A. Das, C. Abeykoon, A. Sinha, A. Karmakar, Phase change materials for battery thermal management of electric and hybrid vehicles: a review, Renew. Sustain. Energy Rev. 104 (2022) 100131.
[28] M.K. Kisomi, Thermal management of lithium-ion batteries: a comparative study of phase change materials and air-cooling systems equipped with fins, arXiv, preprint arXiv:2503.10244, 2025.
[29] S. Bhakta, B. Kundu, A review of thermoelectric generators in automobile waste heat recovery systems for improving energy utilization, Energies 17 (5) (2024) 1016.
[30] P. Saini, J.D. Osorio, Review on phase change materials and thermoelectric generators for ocean thermal gradient applications, Renew. Sustain. Energy Rev. 219 (2025) 115851.
[31] A. Liu, H. Xie, Z. Wu Ve, Y. Wang, Advances and outlook of TE-PCM system: a review, Carbon Neutrality 1 (1) (2022) 1–19.
[32] U. Akram, Z. Tang, Thermo-magnetic convection of MHD Casson fluid in a wavy triangular porous cavity with an embedded cold inverted triangle obstacle, Numer. Heat Transf., Part A: Appl. (2024) 1–13.
[33] U. Akram, Z. Tang, Cold obstacle influence on nanofluid convection in porous cavity, Phys. Fluids 36 (6) (2024) 062011.
[34] M.S. Imran, H.J. Kurji, J.A. Mahdive, R.A. Abdulsahib, Exhaust waste energy harvesting by using a thermoelectric generator with a water heat exchanger, J. Eng. Sci. Technol. 18 (4) (2023) 2020–2034.
[35] Z. Shi, G. Wang, C. Liu, Q. Lv, B. Gong, Y. Zhang, Y. Yan, Optimizing the transient performance of thermoelectric generator with PCM by parametric evaluation, Energies 16 (2) (2023) 1–18.
[36] Z. Shi, J. Wang, C. Jin, L. Chen, Improving transient performance of thermoelectric generator by integrating phase change material, Energ. Conver. Manage. 221 (2020) 113161.
[37] J. Mao, A. Liu, Y. Wang, Y. Li, H. Xie, Z. Wu, Enhancement of power generation of thermoelectric generator using phase change material, IOP Conf. Ser.: Mater. Sci. Eng. 892 (2020) 012055.
[38] A. Al-Janabi, O. Alsalmi, E. Alsubhi, Thermoelectric generators as a heat recovery system for exhaust gases of vehicles driving at low speeds, Eng. Technol. J. 41 (1) (2023) 185–195.
[39] S. Zhang, K. Zhang, L. Li, H. Ge, Z. Zhang, Review on thermal management systems using phase change materials and heat pipes for electric vehicles, Energ. Conver. Manage. 220 (2020) 113036.
[40] K. Li, L. Shi, Y. Zhang, Y. Yao, H. Tian, G. Shu, Global selection appraisal study for heat pump system of electric vehicle based on energetic, economic, and environmental analysis, Carbon Neutrality 3 (1) (2024) 16.
[41] B. Yu, J. Long, Y. Zhang, H. Ouyang, D. Wang, J. Shi, J. Chen, Life cycle climate performance evaluation (LCCP) of electric vehicle heat pumps using low-GWP refrigerants towards China's carbon neutrality, Appl. Energy 353 (2024) 122061.
[42] X. Tang, Q. Guo, M. Li, M. Jiang, Heating performance characteristics of an electric vehicle heat pump air conditioning system based on exergy analysis, Energies 13 (11) (2020) 2868.
[43] N. Javani, I. Dincer, G.F. Naterer, B.S. Yilbas, Exergy analysis and optimization of a thermal management system with phase change material for hybrid electric vehicles, Appl. Therm. Eng. 64 (1–2) (2014) 471–482.
[44] H. Rezaei, M.J. Ghomsheh, F. Kowsary, P. Ahmadi, Performance assessment of a range-extended electric vehicle under real driving conditions using novel PCM-based HVAC system, Sustain. Energy Technol. Assess. 47 (2021) 101527.
[45] L. Lander, A. Hales, E. Kallitsis, J.S. Edge, G.J. Offer, Cost and carbon footprint reduction of electric vehicle lithium-ion batteries through efficient thermal management, Appl. Energy 289 (2021) 116737.
[46] A. Asef, I. Chitsaz, N. Madani, Modeling and total cost optimization of battery thermal management system in a hybrid electric vehicle, J. Energy Storage 52 (2022) 104844.
[47] S. Dincer, M.A. Rosen, Exergy: Energy, Environment and Sustainable Development, 2nd ed., Elsevier, 2013.
[48] D. Luo, S. Yang, Z. Li, J. Cao, H. Chen, Transient energy, exergy, and economic analysis of an automotive thermoelectric generator with different structures, Appl. Energy 377 (2025) 1–12.
[49] Z. Tian, W. Gan, X. Zhang, L. Gu, Performance evaluation of an electric vehicle thermal management system with waste heat recovery: energy, exergo-economic and payback period analysis, Appl. Therm. Eng. 136 (2018) 16–27.
[50] D. Ji, S. Yang, Z. Li, J. Cao, H. Chen, Transient energy, exergy, and economic analysis of an automotive thermoelectric generator with different structures, Appl. Energy 355 (2024) 121999.
[51] A. Mavi, O. Arslan, Numerical investigation on the thermal management of Li-ion batteries for electric vehicles considering the cooling media with phase change for the auxiliary use, J. Energy Storage 77 (2024) 109964.
[52] I. Chriaa, M. Karkri, A. Trigui, I. Jedidi, M. Abdelmouleh, C. Boudaya, The performances of expanded graphite on the phase change materials composites for thermal energy storage, Polymer 212 (2021) 123128.
[53] Y. Jia, Y. Jiang, Y. Pan, X. Zou, Q. Zhang, X. Gao, J. Zhang, K. Yu, Y. Yang, Y. Liu, Recent advances in energy storage and applications of form-stable phase change materials with recyclable skeleton, Carbon Neutralization 3 (2024) 313–343.
[54] S. Liu, T. Zhang, C. Zhang, L. Yuan, Z. Xu, L. Jin, Non-uniform heat generation model of pouch lithium-ion battery based on regional heat generation rate, J. Energy Storage 63 (February) (2023) 107074.
[55] Q. Wang, Q. Sun, P. Ping, X. Zhao, J. Sun, Z. Lin, Heat transfer in the dynamic cycling of lithium - titanate batteries, Int. J. Heat Mass Transf. 93 (2016) 896–905.
[56] Q. Huang, M. Yan, Z. Jiang, Thermal study on single electrodes in lithium-ion battery, J. Power Sources 156 (2) (2006) 541–546.
[57] K. Onda, T. Ohshima, M. Nakayama, K. Fukuda, T. Araki, Thermal behavior of small lithium-ion battery during rapid charge and discharge cycles, J. Power Sources 158 (2006) 535–542.
[58] D. Bernardi, E. Pawlikowski, J. Newman, A general energy balance for battery systems, J. Electrochem. Soc. 132 (1985) 5–12.
[59] L. Chen, Y. Zhang, S. Patel, Performance of high capacity Li-ion pouch cells over wide range of operating conditions, Electrochim. Acta 391 (2021) 138951.
[60] S. Arora, A. Kapoor, Experimental study of heat generation rate during discharge of $LiFePO_4$ pouch cells of different nominal capacities and thickness, Batteries 5 (4) (Nov. 2019) 70.
[61] W. Shen, N. Wang, J. Zhang, F. Wang, G. Zhang, Heat generation and degradation mechanism of lithium-ion batteries during high-temperature aging, ACS Omega 7 (49) (2022) 44733–44742.
[62] E. Peled, S. Menkin, SEI: past, present and future, J. Electrochem. Soc. 164 (7) (2017) A1703–A1719.
[63] P. Gasper, K. Gering, E. Dufek, K. Smith, Challenging practices of algebraic battery life models through statistical validation and model identification via machine-learning, J. Electrochem. Soc. 168 (2) (2021).
[64] Y.J. Lee, H.Y. Choi, C.W. Ha, J.H. Yu, M.J. Hwang, C.H. Doh, J.H. Choi, Cycle life modeling and the capacity fading mechanisms in a graphite/LiNi0.6Co0.2Mn0.2O2 cell, J. Appl. Electrochem. 45 (5) (2015) 419–426.
[65] I. Baghdadi, O. Briat, J.-Y. Delétage, P. Gyan, J.-M. Vinassa, Lithium battery aging model based on Dakin's degradation approach, J. Power Sources 325 (2016) 273–285.
[66] S. Zhang, D. Guan, Z. Xue, C. Shen, Y. Shen, G. Hu, Y. Cao, Z. Peng, W. Wang, Y. Ren, Enhanced elevated-temperature performance of $LiMcik_2O_4$ cathodes in lithium-ion batteries via a multifunctional electrolyte additive, Chem. Eng. J. 503 (2025) 158219.
[67] B. Roy, U. Pal, D. Simondson, C. Nguyen, B. Kerr, R. Hocking, D. Al-Masri, P. Howlett, M. Forsyth, M. Kar, D. MacFarlane, Extreme fast charging and stable cycling of $LiMn_2O_4$ – Li_4Ti5O_{12} lithium batteries by suppression of cathode phase changes, (2023).
[68] R.S. Basu, D.P. Wilson, Thermophysical properties of 1, 1, 1, 2-tetrafluoroethane (R-134a), Int. J. Thermophys. 10 (1989) 591–603.

[69] J. Roy, H. Mahmud, M. Assadi, N. Iman, H. Nikpey, Moving beyond gas: can bangladesh leapfrog and make the energy transition just by exploring the role of geothermal energy and gas infrastructure? Int. Energy J. 20 (3A) (2020).
[70] R.J. Bellair, L. Hood, Comprehensive evaluation of the flammability and ignitability of HFO-1234ze, Process Saf. Environ. Prot. 132 (2019) 273–284.
[71] M. Pierantozzi, S. Tomassetti, G. Di Nicola, Climate change and refrigerants: thermodynamic properties of low-GWP fluids for domestic applications and binary systems for low-temperature options, Appl. Sci. 10 (6) (2020) 2014.
[72] Kryotherm, "TGM-127-1.4-1.2 (datasheet)," [Online]. Available: http://kryothermtec.com/assets/dir2attz/ru/TGM-127-1.4-1.2.pdf.
[73] A. Wadee, P. Walker, N. McCullen, V. Ferrandiz-Mas, The effect of thermal cycling on the thermal and chemical stability of paraffin phase change materials (PCMs) composites, Mater. Struct. 58 (1) (2025).
[74] Rubitherm, "Organic PCM (RT series)," [Online]. Available: https://www.rubitherm.eu/en/productcategory/organische-pcm-rt.
[75] H. Sahli, B. Tashtoush, E. Nahdi, Analysis of a hybrid solar absorption cooling system with thermoelectric generator, Therm. Sci. Eng. Prog. 35 (2022) 101474.
[76] D. Champier, J.-P. Bédécarrats, T. Kousksou, M. Rivaletto, F. Strub, P. Pignolet, Study of a TE (thermoelectric) generator incorporated in a multifunction wood stove, Energy 36 (3) (2011) 1518–1526.
[77] M. Ilbas, S. Akyildiz, S. Karyeyen, A. Aktas, Conventional and distributed combustion regime on a model thermoelectric generator (TEG) performance using a swirl burner/furnace, Fuel 347 (2023) 128487.
[78] H. Ali, Z. Wang, W.K. Alani, J. Zheng, M.A. Fayad, A novel experimental design for free energy from the heat-gaining panel using multi-thermoelectric generators (TEGs) panel, Case Stud. Therm. Eng. 50 (August) (2023) 103431.
[79] X. Cui, Y. Wu, X. Chen, Thermoelectric generation: principles, applications, and prospects, Renew. Sustain. Energy Rev. 224 (2025) 116081.
[80] J. Wiley, Heat Sinks, Thermoelectrics, Heat Pipes, Compact Heat Exchangers, and Solar Cells, (2011).
[81] O. Arslan, A.E. Arslan, I. Kurtbas, Exergoeconomic and exergoenvironmental based multi-criteria optimization of a new geothermal district heating system integrated with thermal energy storage driven heat pump, J. Build. Eng. 73 (2023) 106733.
[82] V.K. Yadav, J. Sarkar, P. Ghosh, Thermodynamic , economic and environmental assessments of a novel solar-driven combined cooling and power syste, J. Clean. Prod. 402 (January) (2023) 136791, https://doi.org/10.1016/j.jclepro.2023.136791.
[83] P.A. Banu, B. Dhanapal, T.M. Pillai, B. Chellappa, R. Sathyamurthy, Thermodynamic and hydraulic design characteristics of the fin tube heat exchanger, Mater. Today Proc. 62 (2022) 2380–2387.
[84] O. Arslan, A.E. Arslan, T.E. Boukelia, Modelling and optimization of domestic thermal energy storage based heat pump system for geothermal district heating, Energy Build. 282 (2023) 112792.
[85] A. Shaito, H. El, J. Faraj, M. Mortazavi, T. Lemenand, ScienceDirect thermal modeling and parametric study of TEG power generation from the exhaust gas of boilers and cold oil tank, Energy Rep. 9 (February) (2023) 51–58, https://doi.org/10.1016/j.egyr.2023.05.248.
[86] H. Zhao, X. Li, Y. Wu, X. Wu, Friction factor and Nusselt number correlations for forced convection in helical tubes, Int. J. Heat Mass Transf. 155 (2020) 119759.
[87] F.P. Incropera, D.P. DeWitt, T.L. Bergman, A.S. Lavine, Fundamentals of Heat and Mass Transfer, 6th ed., John Wiley & Sons, Hoboken, NJ, USA, 2007.
[88] H. Yuncu, S. Kakac, Basic Heat Transfer, Bilim Publishing, Ankara, 1999 in Turkish.
[89] Y. Zhang, S. Zhuang, Q. Wang, J. He, Experimental research on the thermal performance of composite PCM hollow block walls and validation of phase transition heat transfer models, Adv. Mater. Sci. Eng. 2016 (2016) 6359414.
[90] O. Arslan, E. Acikkalp, G. Genc, A multi-generation system for hydrogen production through the high-temperature solid oxide electrolyzer integrated to a 150 MW coal-fired steam boiler, Fuel 315 (2022) 123201.
[91] M. Ghadiri, C.K. Bach, C.R. Bradshaw, Effects of Splitter Placement on Fin-Tube Heat Exchanger Evaporator Performance, in Proc. Int. Refrigeration and Air Conditioning Conf., West Lafayette, IN, USA, (2024).
[92] M. Marcinkowski, D. Taler, J. Sacharczuk, K. Węglarz, J. Taler, Innovative analysis of local and average air-side heat transfer coefficients in fin-and-tube heat exchangers using CFD and experimental method, Energy 297 (2024).
[93] D.S. Wijayanto, M.B.T. Soenarto, W. Prasetyo, I. Widiastuti, Analysis of longitudinal finned pipes in cross-flow heat exchanger, J. Homepage 39 (6) (2021) 1909–1916.
[94] Y.A. Çengel, M.A. Boles, Thermodynamics: An Engineering Approach, 8th ed., McGraw-Hill, New York, NY, USA, 2015, pp. 237–240.
[95] Y.A. Çengel, J.M. Cimbala, Fluid Mechanics: Fundamentals and Applications, 4th ed., McGraw-Hill Education, New York, NY, USA, 2018, pp. 703–707.
[96] M.J. Moran, H.N. Shapiro, Fundamentals of Engineering Thermodynamics, 8th ed., Wiley, Hoboken, NJ, USA, 2014, pp. 648–652.
[97] A.B.G. Altiokka, O. Arslan, Design and optimization of absorption cooling system operating under low solar radiation for residential use, J. Build. Eng. 73 (2023) 106697.
[98] D.K. Erikgenoğlu, O. Arslan, A.E. Arslan, Multi-criteria decision-making optimization of a two-staged solar power plant for low radiation zone through the social decision units, Energ. Conver. Manage. 323 (2025) 119263.
[99] A.B.G. Altiokka, O. Arslan, Performance analysis of residential hybrid cooling and heating system operating under low solar radiation, Process Saf. Environ. Prot. 189 (2024) 246–266.
[100] C. Zhao, J. Huang, D. Xie, Y. Qiao, M. Xu, Thermodynamic and techno-economic analysis of hydrogen production from food waste by torrefaction integrated with steam gasification, Energy Convers. Manag. 299 (2024) 117826.
[101] J. Xia, J. Wang, J. Lou, J. Hu, S. Yao, Thermodynamic, economic, environmental analysis and multi-objective optimization of a novel combined cooling and power system for cascade utilization of engine waste heat, Energy 277 (2023) 127623.
[102] H. Ma, et al., Operating performance and economic analysis of solar single/double-effect compound absorption refrigeration system, Sol. Energy 247 (2022) 73–85.
[103] M. Taheripour, M. Kahani, M.H. Ahmadi, A hybrid poly-generation system for power and hydrogen production by thermal recovery from waste streams in a steel plant: techno-economic analysis, Energy Rep. 11 (2024) 2921–2934.
[104] R. Mastrullo, A.W. Mauro, G. Napoli, L. Viscito, Thermo-economic optimization and environmental analysis of a waste heat driven multi-ejector chiller for maritime applications, Case Stu Therm. Eng. 54 (January) (2024) 104081.
[105] T. Hai, et al., Thermal energy recovery from a Brayton cycle nuclear power plant for efficiency improvement via compressor inlet cooling: thermoeconomic optimization, Case Stud. Therm. Eng. 52 (2023) 103734.
[106] C. Yue, F. You, Y. Huang, Thermal and economic analysis of an energy system of an ORC coupled with vehicle air conditioning, Int. J. Refrig 64 (2016) 152–167.
[107] PCM prices, [Online]. Available from: https://dwoil.de/en/home/#contact (accessed July 2025).
[108] TEG prices, [Online]. Available from: https://es.aliexpress.com/item/32762807511.html?gatewayAdapt=glo2esp4itemAdapt (accessed July 2025).
[109] T. Hai, et al., Developing and optimizing a new cogeneration cycle to produce hydrogen from seawater, Process Saf. Environ. Prot. 184 (2024) 1525–1539.
[110] S. Lecompte, H. Huisseune, M. van den Broek, S. De Schampheleire, M. De Paepe, Part load based thermo-economic optimization of the Organic Rankine Cycle (ORC) applied to a combined heat and power (CHP) system, Appl. Energy 111 (2013) 871–881.
[111] N. Goetzel, M. Hasanuzzaman, An empirical analysis of electric vehicle cost trends: a case study in Germany, Res. Transp. Bus. Manag. 43 (2022) 100825.
[112] T. Koopman, T. Zhu, W. Rohlfs, Performance evaluation of air-source heat pump based on a pressure drop embedded model, Heliyon 10 (4) (2024).